The Role of Hydrodynamic Interactions in the Dynamics and Viscoelasticity of Actin Networks

by

Reza Karimi

Master of Science in Mechanical Engineering
Sharif University of Technology, 2004

Submitted to the Department of Mechanical Engineering in Partial Fulfillment of the Requirements for the Degree of
Doctor of Philosophy in Mechanical Engineering
at the
Massachusetts Institute of Technology
February 2012

© 2012 Reza Karimi. All rights reserved.

Signature of Author ……………………………………………..…………………………………….…
Department of Mechanical Engineering
January 20, 2012

Certified by ……………………………………………………………..………………………..............
Dr. Roger D. Kamm, Professor
Department of Mechanical Engineering and Biological Engineering Division
Chair, Thesis Committee

Certified by ……………………………………..……………………………………………………...
Dr. Mohammad R. K. Mofrad, Associate Professor
Department of Bioengineering, University of California Berkeley
Thesis Supervisor

Accepted by ………………………………………………………………..……………………..................
Dr. David E. Hardt, Professor
Department of Mechanical Engineering
Chair, Department Committee on Graduate Student

The Role of Hydrodynamic Interactions in the Dynamics and Viscoelasticity of Actin Networks

by

Reza Karimi

Submitted to the Department of Mechanical Engineering
on January 20, 2012 in partial fulfillment of the Requirements for the
Degree of Doctor of Philosophy in Mechanical Engineering

Abstract

Actin, the primary component of the cytoskeleton, is the most studied semiflexible filament, yet its dynamics remains elusive. We show that hydrodynamic interactions (HIs) significantly alter the time scale of actin deformation by 2-20 fold at different levels of network structure. For a single fiber, HIs between the mesh-sized segments can change the net force by up to 7 fold. Relaxation times are underestimated, if HIs are ignored, but mode shapes are not affected. HIs can explain deviation of the relaxation times from standard worm like chain models, speculated to be due to internal viscosity of the filament. HIs affect filament alignment, a necessary step for bundle formation. Ignoring HIs can result in up to 20-fold overestimation of shear loss modulus in the 2 μm range investigated. Even for a 1 mg/ml F-actin (0.1% volume fraction), HIs cannot be neglected whether the network is discretized into beads or rods. A shear loss modulus, slightly dependent on system-size, can be defined consistent with (intrinsic) viscoelasticity. However, axial loss modulus follows a quadratic system-size dependency consistent with poroelasticity. Our results suggest that including HIs is critical for consistency in theoretical models or analyzing experimental observation in cytoskeleton mechanics and dynamics. We also propose a new rod method to incorporate the HIs accurately and effectively. This method includes HIs in the larger systems, the same way as typical bead models, but it can decrease the computational cost by up to 100,000 fold.

The primary part of this thesis deals with the viscous properties of the cytoskeletal actin networks investigated via theoretical bottom-up approaches in the nm to μm ranges. However, initially we focus on elastic properties of arterial tissue in the μm to mm ranges via an experimental top-down approach. We develop a combined robust registration and inverse elasticity method to investigate the mechanical properties of arterial tissue. We quantify the accuracy of this method with simulated problems and *in vitro* gels. This method can identify lipid pools via OCT (optical coherence tomography) and assess plaque rupture risk for cardiovascular diagnosis. The method can also be used as a model-based registration technique.

Key words: Actin, Hydrodynamic Interactions, Relaxation Time, Cytoskeleton, Rod Model, Brownian Dynamics, Viscoelasticity, Poroelasticity, Length-Scale Dependent, Inverse Elasticity Problem, Registration, Optical Coherence Tomography (OCT), Atherosclerotic Plaque, Cardiovascular Mechanics

Thesis Supervisor: Dr. Mohammad R. K. Mofrad
Title: Associate Professor of Bioengineering

Acknowledgements

I would like to thank my thesis advisors and my collaborators. This work could not have been accomplished without their help, inspiration and continued support. Dr. Mohammad Reza Kaazempur Mofrad, Dr. Roger D. Kamm and Dr. Brett E. Bouma have all helped me. I am in debt to them for sharing their knowledge with me, encouraging me and allowing me to utilize their lab facilities. Additionally, I am also grateful to Dr. Alan J. Grodzinsky and Dr. Matthew J. Lang for participating in my Ph.D. committee and providing me with great feedback.

I am also grateful to Dr., MD, Elaine Tseng and Dr., MD, Mark Ratcliffe from whom I have learnt much during my internship in University of California, San Francisco. Furthermore, I would like to thank Dr. Daewon Moon from the Korean Research Institute of Science and Standards (KRISS) for providing financial support, sharing his data and collaborating on the elastography part of my thesis. I am also grateful to Dr. Kurt Thorn from the Nikon Imaging Center in University of California, San Francisco for training and support in optical imaging. I would also like to thank Terry Johnson at University of California, Berkeley for sharing his knowledge about cell culture.

Also I would like to thank Dr. Raymond C. Chan. He has always helped me to with my experiments at Wellman Center for Photomedicine and in addition he has spent considerable time assisting me with programming and code implementations. Additionally, I would like to thank another post-doctoral researcher, Dr. Namrata Gunidah, who helped me with my experiments in University of California, San Francisco. Special thanks also goes to Dr. Mohammad-Reza Alam from MIT, a dear friend who has always helped me and has been also my research collaborator in the hydrodynamic interaction part of my thesis.

Thanks to my friends Ruhollah, Alyx, Mo, Yousef, Mehrdad, Ting, Amir, Mohammad A., Brian, Caroline, Jason, Helene, Steve, Sophia, Alex J., Javad, Hengameh, Daniel, Yannis, and also to the greater communities of Mofrad's Lab, Kamm's Lab, and Wellman Center for Photomedicine. My work at MIT and Berkeley could not have been such a pleasure without the company of my dear friends Ali P., Saeed, Abolhassan, Davoud, Salman, Eaman, Vahhab, Mohammad-Taghi, Reza S., Mohammad-Sadegh, Majid, Meysam, Reza G., Hadi, Hamid, Rouzbeh, Farshad, Alireza, Asnavi, Dora, Karan, George, Rahul, Alex A. and Brett.

My research was partially funded by the National Institutes of Health (NIH grant 5-R01-HL70039). Furthermore, during my education at MIT I was fortunate to be the teaching assistant for several faculty members who provided funding for my study and a great

learning experience. I am thankful to Dr. David M. Parks, Dr. Rohit Karnik, Dr. Henrik Schmidt, and Dr. Heidi Nepf from Civil & Enviromental Engineering in MIT. I am especially grateful to Dr. Derek Rowel, who has been my role model in teaching with an endless devotion to his students.

I am infinitely in debt to my advisor, Dr. Mofrad. Not only has Mohammad been my advisor, but he has also been my dearest friend. He has been a constant source of encouragement and an academic role model for me. His support exceeds his role as an advisor and continues in every aspect of my work, career, and life. He had confidence on me, when everyone else doubted and I am forever thankful to him.

Finally, I would like to say that I can never thank my parents enough for their sustained devotion to educate me. I am honored to dedicate this work to them and to my beloved fiancée, Nazanin. In the past few years, Nazanin has provided me with a pure love and patience without which I could not have finished my work.

Table of Contents

Abstract 3

Acknowledgements 5

Table of Contents 7

List of Figures 9

List of Tables 15

Chapter 1: Introduction to Cardiovascular Mechanobiology 17

1.1 Cardiovascular Disease and Atherosclerosis 17
1.2 Pathogenesis of Atherosclerosis 19
1.2.1 Plaque Formation *19*
1.2.2 Life-Threatening Plaque *22*
1.3 Biomechanics of Atherosclerosis 23
1.3.1 Biomechanics in evolution of plaque *24*
1.3.2 Biomechanics in plaque fissure *25*
1.4 Elastography and Elastic Modulus Estimation 27
1.5 Thesis Plan 29
1.5.1 Part I-Elastic Moduli Estimation with Image Registration and Inverse Elasticity *29*
1.5.2 Part II-Viscoelasticity of Actin Networks, Dependence on Hydrodynamic Interactions *30*

Chapter 2: Mathematics of Elastography 33

2.1 Introduction 33
2.2 Direct Elasticity Problem 33
2.2.1 Stress-Strain Constitutive Relations for Vascular Tissues *34*
2.2.2 Custom-Built Finite Element Software and its Verification *38*
2.3 Registration Elasticity Problem 43
2.3.1 Formulation *48*
2.3.2 Numerical Implementation *52*

Chapter 3: Elastography and Registration Results 55

3.1 Inverse Elasticity Problem 55

3.1.1 FEM model: mesh size and constitutive relation ... 56
3.1.2 Shape Complexity and Contrast Recovery Ratio ... 60
3.2 Registration Elasticity Problem ... 63
3.2.1 Registration Problem followed by Inverse Elasticity Problem for an Elastic Band ... 64
3.2.2 Noise Reduction and Strain Limits based on Phantom Gels ... 66
3.2.3 In Vitro Feasibility of IREP ... 69
Chapter 4: Modeling of Hydrodynamic Interactions ... 71
4.1 Introduction ... 71
4.2 Bead Model for Hydrodynamic Interactions ... 73
4.3 Rod Model for Hydrodynamic Interactions ... 74
4.3.1 Simplified Rod Model for Hydrodynamic Interactions ... 74
4.3.2 Rod Drag Coefficients based on Swanson-Batchelor ... 76
4.3.3 Volume Correction and Discretization ... 78
4.3.4 Rod Model: All components together ... 81
Chapter 5: Role of Hydrodynamic Interactions in F-actin Mechanics ... 89
5.1 Introduction ... 89
5.2 Hydrodynamic Interactions in Single Filament ... 92
5.2.1 Rigid Body Movement and Diffusion ... 93
5.2.2 Lateral Fluctuations ... 94
5.3 Hydrodynamic Interactions in Bundle Formation ... 100
5.3.1 Geometry and Assumptions ... 100
5.3.2 Sliding of Antiparallel Filaments ... 103
5.3.3 Zipper Action of Crossed Filaments ... 104
5.3.4 Verification of Simplified Rod Model ... 106
5.4 Hydrodynamic Interaction in Actin Networks ... 109
5.4.1 Idealized Regular 1D Network ... 109
5.4.2 3D Network ... 110
5.4.3 3D-Cross Model to Approximate Hydrodynamic Interactions Strength in a Network ... 114
5.4.4 Hydrodynamic Interactions and System-Size Dependent Viscoelastic Shear Loss Moduli ... 116
Chapter 6: Summary and Conclusions ... 123
6.1 Registration and Inverse Elasticity for Cardiovascular Diagnosis ... 123
6.2 Hydrodynamic Interactions in Cytoskeletal Mechanics and a New Rod Method ... 125
Appendix ... 131
Bibliography ... 131

List of Figures

Figure 1-1: Development of atherosclerosis and stenosis leading to acute myocardial infarction (AMI), taken from[5] 18

Figure 1-2: Primary leukocytes active in the atherosclerosis plaque and their individual transformations: A) monocyte, B)T-lymphocite, and C)mast cell; taken from[5]. 21

Figure 1-3: Primary mechanisms in plaque rupture and thrombosis formation, taken from[19]. 22

Figure 1-4: Schematic depicting conventional procedure to solve the inverse elasticity problem following registration problem. In this thesis, we present a new method to directly relate elastic properties to the image frames (IREP: Inverse Elasticity and Registration Problem). 28

Figure 2-1: Simple depiction showing relation between force/displacement with stress/strain. A: Area, L: Length. 33

Figure 2-2: Patch test for the Quad_8 element in the plane stress and shear mode. (a): Normalized shear stress, (b): element and node indices as well as boundary conditions (red: node index, black: element index, f: force boundary condition, u: displacement boundary condition). Solution corresponds to $\nu = 0.3$ and applied stress of $\tau/\mu = 0.01$ (τ: shear stress). The deformations are scaled by 10 times. 40

Figure 2-3: Stress concentration in a circular hole in plane strain. (a): Energy norm of error versus number of elements follows a quadratic form for Tri_6 element type, (b): Normalized σxx corresponding to the 4th data point in curve (a). Solution corresponds to $\nu = 0.3$ and $\sigma_{\infty}/\mu = 0.01$ 42

Figure 2-4: Stress pattern near a crack. (a): Energy norm of error versus number of elements shows a slow convergence for our Quad_9 element type, (b): Geometry and loading depiction, (c) Normalized σyy corresponding to the 4th data point in curve (a) plotted in the deformed configuration (10 times actual deformation). Solution corresponds to $\nu = 0.3$ and $\sigma_{\infty}/\mu = 0.01$. 43

Figure 2-5: Overall flow chart of the elastography and parameter estimation procedures for arterial plaque characterization taken from Karimi *et al.*[72]. Frames of images, as obtained with IVUS/OCT/MRI modalities, are registered to find the strain map. The images are segmented to build a lumped mechanical model. Then an iterative scheme is used to match the strain computed by image registration and the mechanical model. Finally, when the process converges, a reliable strain/stress/modulus map is achieved. This map can be validated with histological markers of plaques (including their vulnerability level), and then can be used to build biomechanical indices for plaques vulnerability and evolutions. 44

Figure 2-6: Different steps for processing intensity frames for extraction of displacement, strain, and even stress or moduli. Note that how each simpler step might help in initializing more complicated steps. Solid dashed blue line shows a typical IEP (inverse registration problem); it starts from RP (registration problem) and ends by computing moduli. 45

Figure 2-7: Different problems in a 4x4 grid. Each arrow represents an unknown displacement vector. In RP, all nodal displacements are included in the unknown variables and there is no need for a mechanical model. IEP is based on a totally known displacement (possibly from RP), but unknown moduli. In IREP and REP only boundary nodes are considered as unknown displacements. However, IREP is based on unknown moduli, but REP is based on a known (e.g., homogenous) moduli.. 46

Figure 3-1: Human tissue: (a) interior aortic wall of a healthy sample, (b) interior aortic wall of a atherosclerotic subject died due to a cardiovascular disease, (c): atherosclerotic plaques in calcified fixed aortic valves (a surface similar to broccoli surface). Note the healthy smooth tissue versus rough arterial surface caused by atherosclerosis covering all nearby regions. 56

Figure 3-2: Mouse carotid: (a) CARS image showing different lipid structures, (b) corresponding lumped FEM. Yellow: arterial wall, red: needle-shaped lipid crystal, violet: plate-shaped lipid crystal, cyan: lipid pool (appearing as bubbles in CARS image). Image in each direction has 512 pixels with a width equal to 0.25mm. 57

Figure 3-3: Convergence versus FEM mesh size for a lumped inverse elasticity problem in a mouse carotid corresponding to Fig. 3-2. Fine 1 to Fine 4 correspond to meshes becoming finer. Y-axis corresponds to the optimization functional (proportional to the sum of the squared differences between measured displacement and FEM inverse-elasticity-problem calculated displacements). 59

Figure 3-4: Convergence versus mesh size and iteration number for different lumped regions of Fig. 3-2-b. Note that compliant regions converge quickly and stiffer regions converge slowly. 59

Figure 3-5: Recovery of a complicated low-contrast objective (shear) modulus in the invers elasticity problem for (a) Quad_4 elements and (b) Quad_9 elements. In each case, objective moduli is shown on the top figure and the calculated moduli is depicted in the below figure. Colorbars show relative shear moduli. Axis units are in pixel and each pixel is equivalent to 0.01 mm. 61

Figure 3-6: Recovery of an isolated stiff high-contrast objective (shear) modulus in the invers elasticity problem for (a) Contrast=10 (b) Contrast=100. In each case, objective moduli is shown on the top figure and the calculated moduli is depicted in the below figure. Colorbars show relative shear moduli. Axis units are in pixel and each pixel is equivalent to 0.01 mm. 62

Figure 3-7: Contrast recovery curve for an isolated stiff /compliant inclusion having the same geometry as Fig. 3-6. Modulus contrast is related to the ratio of the elastic modulus between the inclusion and the background (arterial wall). Contrast recovery ratio is almost equal to 1, for compliant inclusions; and reduced to 0.4 for a stiff inclusion with a contrast equal to 100. 63

Figure 3-8: Inverse elasticity problem following registration problem of an elastic band imaged by OCT. (a): Shear modulus field, (b): Convergence of relative shear modulus of individual elements (initial guess is equal to 1.0 for all elements). 65

Figure 3-9: OCT gray scale cross section of a uniform gel. The cyan box depicts the region of interest. Magenta and green box correspond respectively to the actual size of the kernel and the search window around each node. Nodes are depicted with blue crosses. Axes units are in pixel and each pixel corresponds to 10 microns. Nodes are separated approximately by 10 pixels, which corresponds to about 50% overlap in their corresponding correlation kernel. Magenta box represents the SB (sub block) used in Eq. 2-10. Green box represented the search domain in which correlations are calculated with FFT before optimization starts. 66

Figure 3-10: Strain estimation based on RP (Registration Problem) without any regularization applied to a simulated incompressible planar stretch of a uniform phantom gel. X-axis in all images corresponds to the applied strain. In the ideal case, the output strain (y-axis left figure) should be constant and equal to the input strain (x-axis). However, the registration generates a variable strain characterized by its average value (left figure), RMS error (root mean squared depicted in the middle figure), and the error in its average value (right figure). 68

Figure 3-11: *In vitro* feasibility of IREP. (a): OCT image of porcine aorta with a lipid pool in the center (temporally and spatially blurred with a Gaussian filter). (b,c): Elastogram corresponding to lateral and axial strains. (d): Relative modulus image. Images are partially taken from Karimi *et al.* [104]. X and Y axes units correspond to pixel indices. 70

Figure 4-1: Hydrodynamic interaction concept: If particle A is in a fluid and it is moving (e.g., to the right), then it will apply a force to the particle B. This force is non-zero, unless particle B moves with the same speed as local fluid (disturbance) velocity caused by particle A. 72

Figure 4-2: Schematic representing particle locations for $H(r_i-r_j)$ (hydrodynamic interaction tensor)........... 73

Figure 4-3: Averaged implicit hydrodynamic interaction model of Chandran *et al.* for filaments with different lengths and at different modes of rigid body movement[109]. The hydrodynamic velocity profiles are shown in gray and their approximations, based on averaged model, are shown in black. (a) Lateral movement, (b): rotation, (c-d): axial motion for two filament with different lengths. Fluctuations in c-d are due to ignoring a nonlinear term, which its effect is cancelled in the averaged model. Picture taken from[109]. 75

Figure 4-4: Comprehensive list of experimental data or computational models to obtain drag coefficients of rods in (a): lateral and (b): axial modes. (Top): drag coefficients, (Bottom): relative difference between above drag coefficient and a reference value based on SB (Swanson-Batchelor). The below graphs show why Batchelor is the best candidate among theoretical models, to be used for interpolation. Different lines/markers correspond to data from different sources[122-133]. Markers represent discrete data sets, and lines represent models based on a continuum function of aspect ratio. Please note that some data set are limited to only lateral or axial mode. 77

Figure 4-5: Drag coefficients of rods discretized into beads having different volume corrections compared against theories or experimental data in (a): lateral, and (b): axial modes for Rotne-Prager tensor. (Top): drag coefficients, (Bottom): relative difference between above drag coefficient and a reference value based on SB (Swanson-Batchelor). The below graphs show why optimal bead can be the best candidate for volume correction and discretization. Different lines/markers correspond to data from different sources[122,123,129-133]. Markers represent discrete data sets, and lines represent models based on a continuum function of aspect ratio. Please note that some data set are limited to only lateral or axial mode. .. 80

Figure 4-6: Relative error in the drag coefficients of rods discretized into beads having different volume corrections compared against theories or experimental data in (a): lateral, and (b): axial modes for (Top): Oseen tensor, (Middle): spherical bead tensor, (Bottom): Rotne-Prager tensor (the stable case). The graphs show relative difference between drag coefficient and a reference value based on SB (Swanson-Batchelor). ... 82

Figure 4-7: Relative error in the drag coefficients of rods discretized into rod segment with different number of segments in (a): lateral, and (b): axial modes for 7 different candidates, a to g, of the Stokes radius for our

Rod model. The graphs show relative difference between drag coefficient and a reference value based on SB (Swanson-Batchelor). 84

Figure 5-1: Actin molecular and macro structure. (a): F-actin (filamentous actin) is formed from two helices composed of G-Actins (Globular actin: having a known protein sequence). F-Actin is a polarized molecule having different ends. Picture is taken from Dominguez *et al.*[138]. (b) Actin organization in 3T3 cells: A) fluorescence-staining of F-actin, B-D) electron microscopic image of actin. B) Actin junction. C) Homogenous structure at the leading edge, D) polarized/ Heterogeneous structure elsewhere. Picture is taken from Svitkina *et al.*[139]. (c) Similar to (b)-A, F-actin forms different structure inside the cell and has different concentration at various locations. Some F-actins form bundles, called stress fibers, which are the key component of the cell motility (especially with the aid of focal adhesion proteins such as Vinculin, which is stained here). Focal adhesions and F-actin are visualized with anti-vinculin antibodies and phalloidin, respectively in U2OS cells. Three categories of contractile actin arrays are highlighted on the F-actin image: dorsal stress fibers (red), transverse arcs (yellow) and ventral stress fibers (green). Scale-bar: 10 micrometer. Picture is taken from Hotulainen *et al.*[140]. 90

Figure 5-2: F-actin crosslinked network at different concentration/types of crosslinkers taken from Lieleg *et al.*[137]. We are particularly interested in HMM (Heavy Myosin Motor) case, which forms isotropically crosslinked active networks. 91

Figure 5-3: Dimensionless (a) normal ($C_{\perp}$), and (b) axial ($C_{\parallel}$) drag coefficients of an actin filament (η: viscosity, U: velocity, a: filament radius). Blue line: reference values based on SB (Swanson-Batchelor) introduced in section 4.3.2 [15,16]. Dashed black line: discretized into mesh-sized, ξ, rods without HIs. Dash-dotted red line: discretized into beads with the same diameter as the filament without HIs. Inset shows different discretizations. 93

Figure 5-4: (a) Mode shapes and (b) local drag coefficient for a 0.7 μm filament at different modes. Solid blue line: rigid body lateral translational mode. Red shades: the first 10 modes. Brighter reds correspond to higher modes. Dashed and dash-dotted lines represent first and second modes respectively. This filament is discretized into 100 spherical beads each with a 7-nm diameter. 96

Figure 5-5: Normalized internal product of mode shape and hydrodynamic force, $q_i \otimes f_{h\,i}$, for different modes. Line styles match legend of Fig. 5-4-b. This internal product represents a power ratio (out of 1.0) for the component of the hydrodynamic force consistent with assuming a uniform drag for each mode (i.e., ignoring local variations in the drag coefficients, shown in Fig. 5-4-b, due to hydrodynamic interactions). 97

Figure 5-6: HI effects on the first 10 lateral bending modes versus actin filament length (L): The ratio of drag coefficient for a given mode compared to the drag coefficient of rigid body lateral translation is plotted here. This ratio is the same as the underestimation in relaxation time of those bending modes, if we use $\zeta_{\perp}$, instead of ζ_i Inset: the normalized root mean squared error of linear fit to examine proportionality between local velocity and local drag. Blue line: rigid body lateral translational mode. Red lines: the first 10 bending modes (brighter colors: higher modes). 99

Figure 5-7: Two F-actin filament being aligned. (a): Acto-myosin: sliding of anti-parallel filaments. (b): Zipper action for crossed parallel filaments. The same geometry also applies to passive crosslinker; although for passive crosslinkers, the directionality of F-actins is not important. 101

Figure 5-8: Acto-myosin force balance during cell migration. Myosin forces can be balanced with filament movements, force transfer to substrate via focal adhesion, retrograde flow, etc. Picture taken from danuser lab (http://lccb.hms.harvard.edu/research.html) 102

Figure 5-9: Effect of hydrodynamic interactions between two antiparallel F-actins being aligned by myosin. F represents axial force. Overlap and L are defined in Fig. 5-7. 103

Figure 5-10: Normalized force distribution, $\mathrm{F(s, Overlap)}$, for 3 overlap values: blue) side by side and maximum force, red) half side by side, black) at distance infinity corresponding to minimum force . This simulation corresponds to two 10 $\mu\mathrm{m}$ antiparallel actin filament coming side by side. We chose H=47 nm to elevate HIs and have a curve that better distinguishes the above 3 states. Nonetheless, H=707 nm results in the qualitatively similar curve, but with a less steep wave front. Force values near free ends, s=0 and 1, have fluctuations due to approximations in HIs tensor. (μ: viscosity, *U*: velocity, *a:* filament radius) 104

Figure 5-11: Effect of hydrodynamic interactions between two crossed F-actins being aligned. (a): H=707 nm, simulating myosin for crossed and parallel filaments. (b): H=47 nm, simulating passive crosslinkers representing α-actinin. T represents the torque required to rotate the filaments. θ and L are defined in Fig. 5-7. 105

Figure 5-12: Comparison of approximate rod model and bead model for effect of hydrodynamic interactions between two antiparallel F-actins being aligned by myosin. Bead model: solid line with circular marker. Rod model: dashed line with square marker. Different graphs vary on the number of rod segments used for discretization of each filament. X-axis: $\mathrm{Overlap/L}$. Y-axis: $\mathrm{F_{with\ HI}/F_{w/o\ HI}}$. F represents axial force. Overlap and L are defined in Fig. 5-7. 107

Figure 5-13: Effect of HIs between two beads moving toward each other with equal speeds on H-spaced parallel lines. Beads have a 7 nm diameter, equal to the diameter of F-actin. System geometry is shown on the subset. The ratio plotted corresponds to the force component in parallel to V. Note that maximum interaction (peak value of y-axis) does not necessary happens when the beads have the minimum distance ($\theta = 90°$). .. 108

Figure 5-14: A regular 1D actin network built from different numbers of 56 nm units is devised, and dimensionless force to impose shear (diamond marker) or stretch (square marker) is calculated. Three methods for computing hydrodynamic forces are compared: 1) bead with HIs (blue), 2) mesh-sized rod segments w/o HIs (black), and 3) beads w/o HIs (red). When HIs are small, the markers overlay to appear as hexagonal stars. Inset: deformation modes and networks discretized into beads for N=1 and N=3 units. Beads are colored according to z-coordinate for 3D visualization. 109

Figure 5-15: Dimensionless (a) loss modulus and (b) dissipative power per unit volume versus network/system size with HIs included (blue) and excluded (red), for uniform strain rate in pure axial elongation (square marker), and simple shear (diamond marker). Without HIs, the red markers overlay to appear as hexagonal stars. Solid dotted line in (a): L^2 scaling as the expected behavior when HIs are excluded and filaments are homogenously distributed. Gray dashed line in (b): F-actin concentration in mg/ml (on average 1 mg/ml). Subsets in (a): corresponding cubic networks for S=0.7 μm and 1.4 μm discretized into beads (colored according to z-coordinate for 3D visualization). 111

Figure 5-16: Simplification of a regular network into a 3D cross. (a): A regular network formed from filaments representing cubic units. This network is extended to infinity, but for simplicity only 3 units in each direction are plotted. Filaments are colored for better 3D visualization, but they are all identical. (b): 3D-cross as the repetitive unit of the network in part (a). All members of the cross have the same length (equal to mesh size: ξ). (c): 3D-cross discretized into beads. This specific number of beads correspond to $\xi/(2a)$=11 (a: filament radius). Beads are colored according to z-coordinate for better 3D visualization. 114

Figure 5-17: Viscoelastic moduli of F-actin at (a) 1.0 mg/ml, and (b): 0.3 mg/ml concentrations compared between 1P, 2P and bulk rheology. Bead radius: 0.42 μm. Picture is taken from Garden *et al.*[143]. 118
Figure 5-18: Viscoelastic moduli of F-actin at 1.0 mg/ml concentrations compared between 1P, 2P and bulk rheology for varying filament (contour) lengths: (a): 0.5 μm, (b): 2 μm, (c): 5 μm, (d): 17 μm. Bead radius: 0.42 μm. Picture is taken from Liu *et al.*[156]. Solid blue line represents $\omega^{3/4}$ scaling. 119
Figure 5-19: Viscoelastic moduli of F-actin transiently crosslinked with Rigor HMM compared between micro and macro rheology. Bead radius: 0.42 μm. Picture is taken from Lieleg *et al.* supplemental material[142]. 120

List of Tables

Table 3-1: Material properties selected for nonlinear ABAQUS simulation corresponding to Fig. 3-2-b. 58
Table 3-2: Error quantification for pure registration in static case (similar frames at different times) and rigid body displacement (due to moving scanner head). 67
Table 4-1: Drag coefficients for low aspect ratio rods, adopted from computational data in Table IV by Swanson *et al.*[123]. These discrete data points are combined with C values from Eq. 4-1 at $A = 15$ to be interpolated of at $1 < A < 15$ 78
Table 4-2: Different methods to discretize a filament into stacked beads starting from shish kebab's model, followed by different ways to compensate for volume and finally our proposed model. Schematic shows a filament composed of 3 beads, but effective bead diameters and overlaps are not to actual scale. Filament radius, effective radius, hydrodynamic radius and bead spacing are represented by a, ae, RH and s respectively. 79
Table 5-1: Nomenclatures used in analyzing filament fluctuations. 95

Chapter 1: Introduction to Cardiovascular Mechanobiology

1.1 Cardiovascular Disease and Atherosclerosis

Cardiovascular disease (CVD) holds the first rank in the mortality and morbidity rate in the United States[1]. Furthermore, the world health organization (WHO) is expecting that CVD will become the major killer globally within 9 years[2]. In the United States, CVD has been the first killer since 1900, every year but 1918. Recent mortality data shows that CVD, as the underlying cause of death, accounted for 33.6% of all 2,423,217 deaths in 2007, or 1 of every 3 deaths in the United States[1]. Moreover, CVD claims more lives each year than the next four leading causes of death combined, which are cancer, chronic lower respiratory diseases, accidents, and diabetes mellitus in the United States[3]. CVD not only is a leading cause of death, but also is expected to cost about $286 billions for Americans in 2007[1]. Consequently, CVD prevention, early diagnosis, and treatment can save thousands of lives and dollars.

Apparently the most frequent CVD diseases are stroke, heart attack, high blood pressure, congenital cardiovascular defects, arrhythmias (disorders of heart rhythm), arterial diseases, bacterial endocarditis, and cardiomyopathy. However, many of these diseases can be the direct or indirect consequence of atherosclerosis. Atherosclerosis word comes from the Greek words *athero* (paste) and *sclerosis* (hardness)[4]. This disease is an inflammatory process, which involves deposits of fatty substances, cholesterol, cellular waste products, calcium and other substances in the arterial wall.

These deposits are called plaques and they typically affect large and medium-sized arteries. Three proven causes of damage to the arterial wall are[4]: 1) elevated levels of cholesterol and triglyceride in the blood, 2) high blood pressure, and 3) tobacco smoke.

These plaques (or atheromas) produce enzymes that enlarge the artery over time. As long as the artery enlarges sufficiently to compensate for the extra thickness of the plaque, then stenosis (narrowing of the flow cross section) will not occur (Fig. 1-1). If the enlargement is beyond the proportion of the atheroma thickness, then the less frequent disease of aneurysm will happen.

Stenosis or atherosclerosis is usually divided into two categories: coronary artery disease (CAD) and peripheral arterial disease (PAD). CAD involves the coronary arteries, but PAD occurs outside the heart (e.g., in the brain, kidneys, legs or arms). There are four major PAD types/sites: Cerebrovascular PAD, PAD of renal arteries, PAD of the lower extremities, and PAD of the mesenteric arteries.

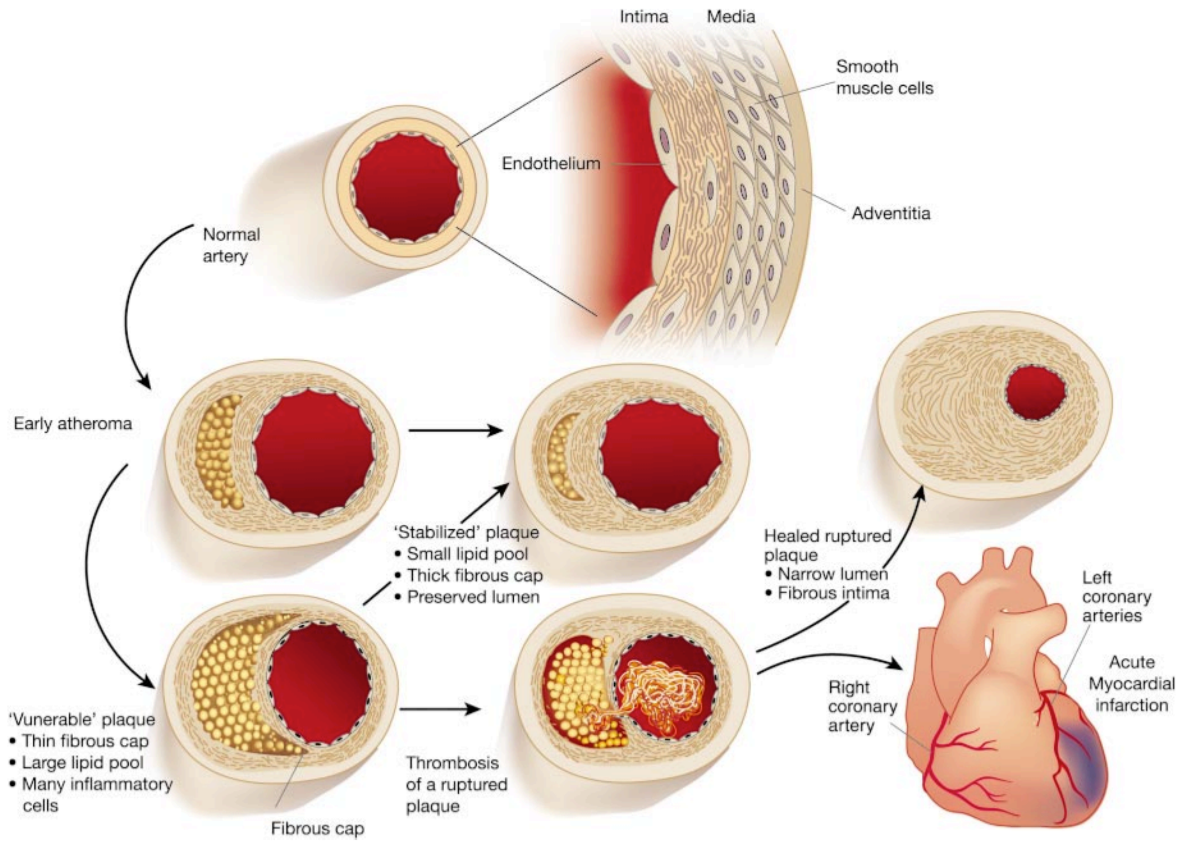
Intima
Media
Smooth muscle cells
Endothelium
Adventitia
Normal artery
Early atheroma
'Stabilized' plaque
• Small lipid pool
• Thick fibrous cap
• Preserved lumen
Healed ruptured plaque
• Narrow lumen
• Fibrous intima
Left coronary arteries
Acute Myocardial infarction
Right coronary artery
'Vunerable' plaque
• Thin fibrous cap
• Large lipid pool
• Many inflammatory cells
Fibrous cap
Thrombosis of a ruptured plaque

Figure 1-1: Development of atherosclerosis and stenosis leading to acute myocardial infarction (AMI), taken from[5].

Stenosis can impose local or global blood pressure problems. For example, in renal arterial disease, stenosis increases blood pressure indirectly and eventually even kidneys might fail. As another example, PAD of the lower extremities happens to be a major cause of diminished ability to walk, pain in legs and in advanced cases leg amputation. Moreover, less frequent PAD of the mesenteric arteries (mesenteric arterial disease) can cause severe pain, weight loss and death from intestinal gangrene.

Furthermore plaques might become unstable and rupture. Their rupture can release some chemicals in the blood stream, which in turn ends to clot formation. The blood clot (thrombus) can totally block the blood flow in the arteries. The clot can block blood flow in the arteries in which it is formed or it might move to smaller arteries, block them and cause embolus. The destination organ determines the kind of apparent disease. For example, thrombosis in coronary leads to heart attack. Moreover, thrombosis in arteries supplying blood to brain, like carotids, ends to cerebrovascular disease which is the number one reason for stroke and disability in the United States[1].

1.2 Pathogenesis of Atherosclerosis

There are major evidences and motivations for standing against atherosclerosis. Section one of this thesis aims to test and develop elementary principles of a new diagnostic technique for atherosclerosis. Any technique is highly dependent on complicated pathological and mechanobiological evolution of plaques and so enhancing our knowledge about pathogenesis of atherosclerosis is a critical step. Here a brief summary of process leading to development of atherosclerosis, its underlying structure and its rupture is presented.

For years, atherosclerosis was thought to be a natural response to aging. Then it was found that hypercholesterolemia plays a major role in pathogenesis of atherosclerosis[6]. Since mid 1980[7], several groups have investigated the inflammatory pathway in atherosclerosis[5,8-12]. Consequently, markers of inflammation like CRP (C-reactive protein), IL-6 (Interleukin), or VEGF (Vascular endothelial growth factor) can be utilized for cardiovascular risk assessment[13].

1.2.1 Plaque Formation

At the beginning, the endothelium increases its permeability to lipoproteins and other plasma constituents. This event is mediated by nitric oxide, prostacyclin, platelet-derived growth factor, angiotensin II, and endothelin. Other mediators include: up-regulation of leukocyte and endothelial adhesion molecules and also migration of leukocytes into the artery wall. This migration is mediated by oxidized LDL (low-density lipoprotein), MCP-1 (monocyte chemoattractant protein), IL-8 (interleukin), platelet-derived GF (growth factor), M-CSF (macrophage colony stimulating factor), and osteopontin[10].

Atherosclerosis begins with arterial wall injury. However, vascular progenitor cells, especially EPCs (endothelial progenitor cells produced primarily by bone morrow), have an intrinsic capacity for repair of the vascular wall and are important contributors to the vascular repair process. Such cells are released in response to signals derived from the injured vascular wall and anchor at the sites of arterial lesions. Evidence for their contribution to the repair of the arterial wall is emerging. Their absence or dysfunction result in more advanced vascular lesions, whereas their administration to animals deprived of competent vascular progenitor cells can retard the onset of vascular disorders[14].

Under ordinary conditions, the endothelial cells oppose against the firm adhesion of leukocytes. However, endothelium dysfunction, caused by inflammatory cytokines provides initial adhesion of leukocytes. Those cytokines in turn can be produced by lipoprotein oxidation following hyperlipidemia. Other triggers like smoking, hypertension, hyperglycemia, obesity, or insulin resistance, can also initiate the expression of adhesion molecules by endothelial cells[15].

The specific roles of monocytes, T-lymphocites, and mast cells are demonstrated in Fig. 1-2. All these leukocytes are the primary cells in the formation of atherosclerotic plaques but monocytes are the most important ones. As demonstrated by Fig. 1-2-A, monocytes adhere to the endothelium layer mostly via VCAM-1 (vascular cell adhesion molecule). After adhering, leukocytes are pulled to the tunica intima by chemoattractant gradient via endothelial cell junctions. For example, blood monocytes are derived primarily by interaction of MCP-1 with its receptor CCR2. Once monocytes enter intima, they go through a series of events, acquire macrophage characteristics, replicate and finally form "foam cells". Within intima, monocytes over express scavenger receptors from modified lipoproteins such as SRA (scavenger receptor A) and CD36. Modified LDL taken up via scavenger receptors is delivered to lysosomes, where enzymes hydrolyze cholesterylesters to free cholesterol and fatty acids. These lipid-laden macrophages, known as foam cells, characterize the early atherosclerotic lesion. Macrophages within atheroma also secrete a number of growth factors and cytokines involved in the lesion progression and complication[5].

Lipid-laden monocytes, macrophages (foam cells), and T-lymphocytes (T-cells) form initial fatty streaks. Subsequently, various SMCs (smooth muscle cells) migrate to the lesion as well. This migration is stimulated by platelet-derived GF, fibroblast GF-2, and transforming GF-β. Similarly, T cells become activated when they bind to antigen processed and presented by macrophages (Fig. 1-2-B). T-cell activation amplifies the inflammatory response due to the secretion of cytokines like IFN-γ (interferon), TNF-α and β (tumor necrosis factor). Furthermore, blood platelets adhere and aggregate to the arterial wall stimulated by integrins, P-selectin, fibrin, thromboxane A_2, tissue factor, and other factors responsible for the adherence and migration of leukocytes. Meanwhile, foam cell formation is mediated by oxidized LDL, M-CSF, TNF-α, and IL-1[10].

Fatty streaks progress to intermediate and advanced lesions by forming a fibrous cap that surrounds the injury site. The fibrous cap forms due to decreased connective-tissue degradation and increased activity of platelet-derived GF, transforming GF-β, IL-1, TNF, and osteopontin. The fibrous cap contains a mixture of leukocytes, lipid, and debris, which may form a necrotic core. These lesions expand at their shoulders by means of continued leukocyte adhesion and entry. The necrotic core represents the results of apoptosis and necrosis, increased proteolytic activity, and lipid accumulation. The principal factors associated with macrophage accumulation in this period include M-CSF, MCP-1, and oxidized LDL[10].

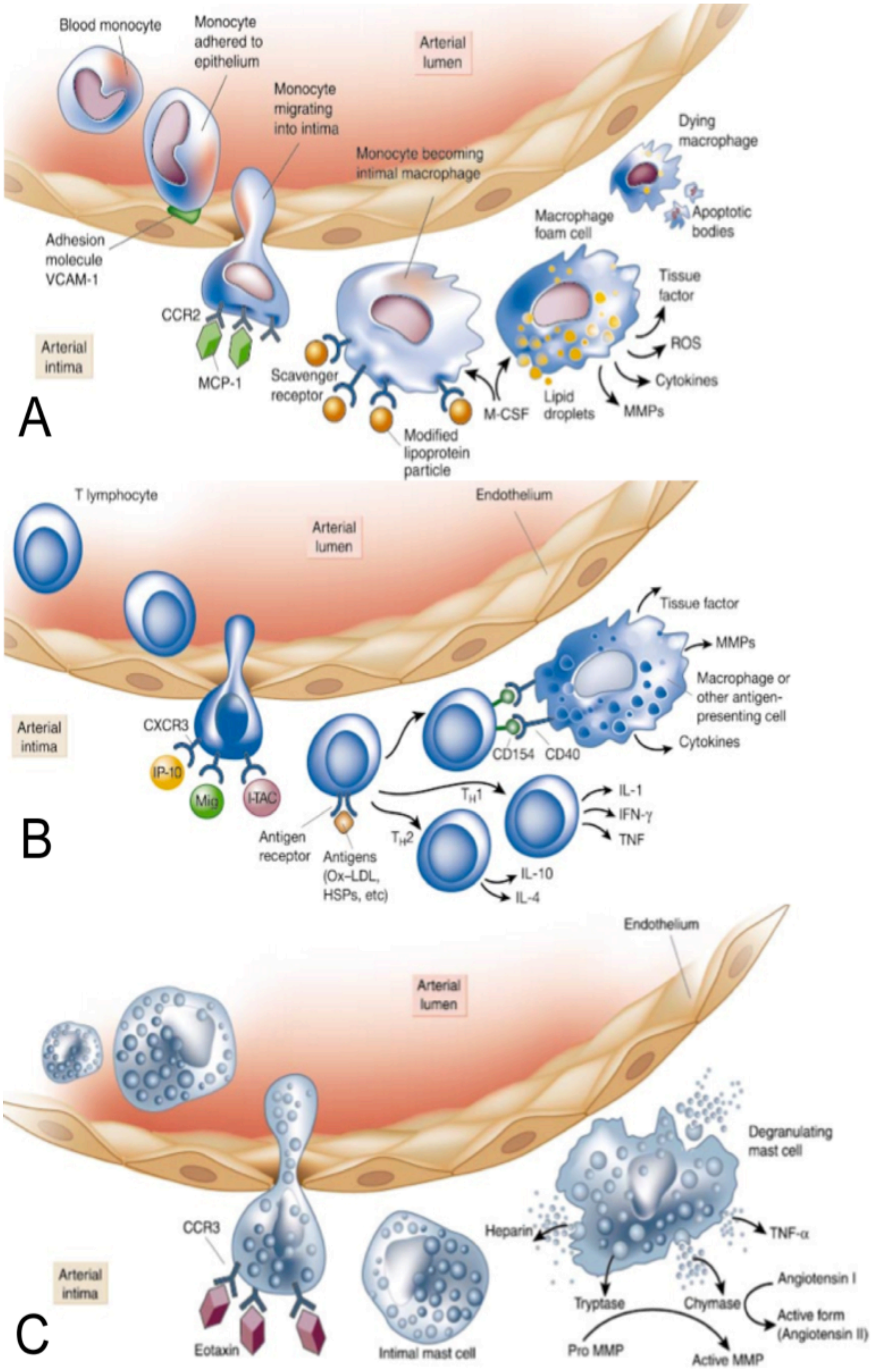
Blood monocyte
Monocyte adhered to epithelium
Arterial lumen
Monocyte migrating into intima
Monocyte becoming intimal macrophage
Dying macrophage
Apoptotic bodies
Adhesion molecule VCAM-1
Macrophage foam cell
Tissue factor
CCR2
ROS
Arterial intima
Cytokines
MCP-1
Scavenger receptor
M-CSF
Lipid droplets
MMPs
A
Modified lipoprotein particle
T lymphocyte
Endothelium
Arterial lumen
Tissue factor
MMPs
Macrophage or other antigen-presenting cell
Arterial intima
CXCR3
CD154
CD40
Cytokines
IP-10
Mig
I-TAC
T_H1
IL-1
IFN-γ
TNF
B
Antigen receptor
Antigens (Ox-LDL, HSPs, etc)
T_H2
IL-10
IL-4
Endothelium
Arterial lumen
Degranulating mast cell
CCR3
Heparin
TNF-α
Arterial intima
Angiotensin I
Tryptase
Chymase
Active form (Angiotensin II)
C
Eotaxin
Intimal mast cell
Pro MMP
Active MMP

Figure 1-2: Primary leukocytes active in the atherosclerosis plaque and their individual transformations: A) monocyte, B)T-lymphocite, and C)mast cell; taken from[5].

1.2.2 Life-Threatening Plaque

Atherosclerosis begins very early in the life. Indeed one-sixth of American teenagers already have pathologic intimal thickening in their coronary arteries[16]. However, it takes several decades, for initial fatty streak to be transformed to an advanced lesion and result in clinical issues.

Higher shear stress due to stenosis or remodeled artery can stop plaque size growth and stabilize its geometry. In fact stenosis by itself is not a major health issue compared to thrombosis and plaque rupture. Indeed, only in 15% of cases studied by serial angiogram data extreme stenosis occurred weeks or months before MI[17]. Additionally, as mentioned earlier, coronary arteries can enlarge and compensate for plaque enlargement, thus preserving the flow of blood to the myocardium. This mechanism becomes overwhelmed only when the stenosis occupies 40% of the arterial lumen[18].

Rupture or ulceration of the fibrous cap, can rapidly lead to thrombosis and usually occurs at sites of cap thinning in the advanced lesions. Thinning of the fibrous cap is apparently due to the continuing influx and activation of macrophages, which release metalloproteinases and other proteolytic enzymes at these sites. These enzymes cause degradation of the matrix, which can lead to hemorrhage from the vasa vasorum or from the lumen of the artery, and can result in thrombus formation and occlusion of the artery[10].

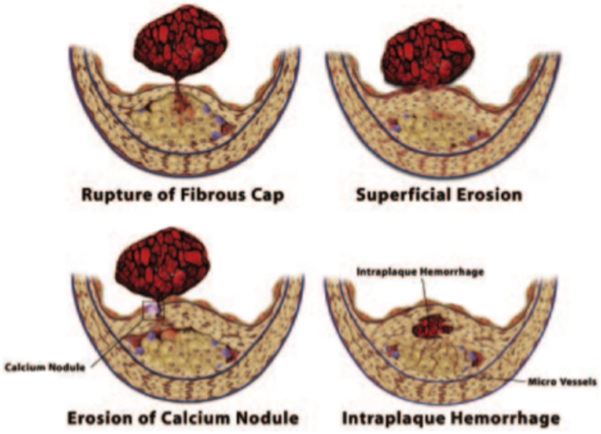

Figure 1-3: Primary mechanisms in plaque rupture and thrombosis formation, taken from[19].

As demonstrated by Fig. 1-3 four mechanisms can lead to plaque rupture and thrombosis formation. Rupture of fibrous cap is responsible for about two third, to three quarters of fatal coronary thrombosis. Superficial erosion occurs in one fifth, to one quarter of all cases of fatal coronary thrombosis. Erosion of a calcium nodule may also cause plaque disruption and thrombosis. In addition, friable microvessels in base of atherosclerotic plaque may rupture and cause intraplaque hemorrhage. Consequently, local generation of thrombin may stimulate SMC proliferation, migration, and collagen synthesis, promoting fibrosis and plaque expansion on subacute basis. Similarly, severe intraplaque hemorrhage can cause sudden lesion expansion by mass effect acutely[19].

1.3 Biomechanics of Atherosclerosis

The hemodynamic forces play a major role in the formation, development and eventual rupture of atherosclerosis plaques. Unlike ordinary passive structures exposed to fluid forces, the cardiovascular system is a highly active system and adapts itself to flow conditions, as well as to other body signals. Consequently, from the biomechanical point of view, there are almost two separate ongoing areas of research emphasizing the biomechanics of atherosclerosis. The first area of research is the evolution of plaque due to biomechanical forces, and is highly linked to the second one, plaque rupture. Here we are interested in the second one, and we want to utilize this for diagnostic analysis.

The first area of research is dealing with the long-term effects of hemodynamic forces on the plaque formation and composition, artery remodeling, and related gene expressions. This can be connected to the second section of this thesis dealing with actin as the primary component of the cytoskeleton. However, the second area of research, is mostly concerned with the final event of plaque fissure, in order to build a plaque vulnerability index. The first area mostly deals with the biological evolution of plaque, while the latter evaluates mechanical forces that might lead to plaque rupture. It is clear that both areas of research are highly linked and this is just a simplification for dividing the research.

Evaluation of related mechanical factors is more complicated when we are concerned about evolution than when we are interested in rupture. For the rupture case, we might neglect fluid structure interactions (FSI) and simplify our FEM (finite element modeling) analysis. This relies partly on the fact that the lumen tensile stress induced by blood pressure load is several orders of magnitude larger than that induced by wall shear stress (WSS)[20]. However, as we will see, when we are dealing with plaque evolution analysis, the interaction between wall and fluid shear force has a major biological role in the plaque formation.

1.3.1 Biomechanics in evolution of plaque

Since the early 1960s, research has been conducted on the effects of hemodynamics forces on the development of plaques[21-25]. However, only recent discoveries and novel available technologies let us have a better understanding of the exact biological and molecular pathways of mechanotransduction in the arterial wall[20,26-28].

The development of atheromas cannot be blamed only on hyperlipidemia, inflammatory response, smoking or other general factors. In fact, while the whole body receives the same blood, only certain locations in the arterial tree are prone to atherosclerosis. These focal sites are those associated with complex hemodynamics, such as bifurcations, junctions, regions of high curvature or anywhere there is an abrupt change in flow conditions[29].

As a result, many researchers have attempted to correlate flow indices to pathological indices of atherosclerosis evolution. The most and the longest studied index is the wall shear stress (WSS)[30]. Wall shear stress is thought to be markedly different in focal sites of atherosclerosis and considerable attention has been paid to it.

Traditional hypotheses declare that regions with high and low wall shear stress are both dangerous. However, now we know that high shear stress is not severely dangerous and in fact temporal or spatial derivative of shear stress might be more important than its absolute value[29]. In other words, the flow condition can be divided with respect to being laminar or turbulent.

Still our knowledge about hemodynamic effects is considerably limited and there are several contradictory opinions. Part of this controversy relies on the multifactorial and multistage development of atherosclerosis. Consequently, we do not expect any more, that a single hemodynamic factor can characterize the entire life of all types of plaques. For example, it is believed that low shear stress provides favorable conditions for atheroma initiation and as a simple explanation, low shear stress facilitates the adhesion of leukocytes to the endothelial layer. On the other hand, high shear stress might accelerate endothelial injury and erosion, and finally lead to plaque rupture and thrombosis.

In summary, shear stress can induce atherogenic or atheroprotective effects via several molecular and cellular pathways. Those pathways mostly interact with vascular endothelium cells, which have different behaviors for different flow regimes. Nonlaminar flow promotes changes to endothelial gene expression, cytoskeletal arrangement, wound repair, leukocyte adhesion as well as to the vasoreactive, oxidative and inflammatory states of the artery wall. Disturbed shear stress also influences the focal pattern of atherosclerotic, associated wall remodeling, plaque vulnerability, stent restenosis and smooth muscle cell intimal hyperplasia in venous bypass grafts[31].

Investigation of shear stress role in atherosclerosis is not of our immediate interest and this discussion is closed here. Yet, it should be taken into account that an accurate analysis of plaque evolution and rupture cannot be carried out without monitoring biomechanical factors such as shear stress over a long time span. In addition, there are still several unknown pathways by which interacting mechanical and chemical signals can alter plaque evolution. For example, high cyclic mechanical strain is known to have a considerable effect on atherosclerosis. It is demonstrated that cyclic strain up regulates the expression of eNOS (endothelial nitric oxide synthase) transcripts and protein levels in bovine aortic endothelial cells[32]. Kakisis *et al.* and Lee *et al.* provide further details in their reviews about mechanotransduction pathways of cyclic strain on vascular cells[33,34].

1.3.2 Biomechanics in plaque fissure

For more than two decade, there has been an intense interest in studying biomechanical factors affecting atherosclerosis. Those data can help us to suppress this disease and propose new therapeutic methods as well as better stents. In addition, diagnostic techniques and assessment of plaque vulnerability highly relies on state of hemodynamic forces. No one can propose a vulnerability index without considering the chance of plaque rupture, and no rupture can be analyzed without evaluation of stress and strain patterns.

Our ultimate objective is to develop a mechanical vulnerability index for plaque rupture. The ruptured fibrous cap causes some three-quarters of acute myocardial infarctions, still most episodes probably cause no clinical symptoms[5]. However, 70% of high grade stenosis have had a prior disruption that healed[35]. Moreover, vulnerable plaques are not isolated, so even if one plaque rupture does not lead to a clinical syndrome, a nearby plaque might soon cause a fatal event[36]. These facts together emphasize that plaque rupture is the most serious event that should be prevented and that is why many researchers have focused on identifying rupture sites. Although, a future research might focus on predicting which plaque disruption is dangerous and causes ischemia or thrombosis.

Plaque rupture can be analyzed as a totally mechanical event, provided that we have a reasonable set of parameters for constitutive stress-strain relations, as well as a rupture criterion. On the other hand, it can be rather reliably predicted by knowing plaque composition and geometry. However, as a matter of fact, we have neither a perfect set of mechanical parameters nor a good imaging modality to reveal both geometry and composition of plaque accurately. Consequently, we seek to combine imaging data with a mechanical model to further develop vulnerability indices[37]. In the next parts, we will discuss how to obtain those parameter sets and which imaging modalities to utilize. Now, we briefly review the feasibility of using stress and strain patterns to predict plaque rupture sites.

Plaques have an astonishingly complicated 3D geometry with anisotropic and non-homogenous mechanical behavior. Nonetheless, simple 2D and 3D linear isotropic models have shown satisfactory results in predicting rupture sites. No one has ever proposed a sophisticated rupture model and basically in all studies sites of elevated stress, strain or cyclic strain are interpreted as rupture prone sites. Holzapfel *et al.* provide an excellent review on the attempts to determine mechanical properties of atherosclerosis plaques[38]. Meanwhile, it should be noted that stress values are not very sensitive to variation in material properties. In other words, prescribed force boundary condition (applied as blood pressure) suppresses stress variation due to constitutive relation, even if we use a model with anisotropic or nonlinear material properties[39].

By 1989 the connection between plaque rupture and blood pressure load was identified using finite element modeling (FEM) and postmortem pathological comparisons[40], although earlier, attention was focused on the shear stress effects. Since then, FEM modeling has been extensively used to study biomechanics of plaque rupture. Several 2D and 3D models have been built and various effects by utilizing fluid only, structure only and fluid-structure interacting models have been studied[41-43].

In particular, it has been demonstrated that sites of stress concentration are severely vulnerable. Good correlation has been found between increased circumferential tensile stress and sites of plaque rupture, usually located near thin cap shoulders[44]. This is a well accepted hypothesis for plaque vulnerability assessment[40,45-48]. Other risk factors, like elevated strain levels, have also been studied but they are not directly correlated to plaque rupture and they seem to be more involved in morphological changes of tissue[33,49].

Additionally, a newer study proposed a fatigue model for studying the plaque rupture. It demonstrated that cracks begin at the lumen wall at areas of stress concentration, depending on the shape of the lumen, thickness of the fibrous cap, and stiffness of the plaque components. Mean or pulse pressure did not affect initiation location. Cracks extended radially and grew at a rate that was highly dependent on both mean and pulse pressure and on lipid stiffness. It was concluded that a fatigue mechanism reconciles clinical evidence of acute plaque rupture at seemingly low stress levels[41]. Yet, the crack develops at location of elevated stress and in summary, if we can identify stress concentration sites we have identified vulnerable plaque rather reliably.

1.4 Elastography and Elastic Modulus Estimation

In the previous section, we demonstrated that plaque evolution and rupture is related to mechanical factors, stress and strain. Currently, we want to study how related mechanical parameters can be measured. As stated earlier, Holzapfel *et al.* provide a good review on attempts to quantify mechanical parameters of atherosclerosis plaques[38]. While *in vivo* we have biaxial loading, most studies have used *in vitro* uniaxial tension tests and the results are sensitive to the specific test setup[47].

Additionally, the numerical values proposed by literature vary widely, for example they cover four orders of magnitude for lipids[50,51]. This variation is mostly due to the large morphological extent that a plaque and its constituents may cover[44,52]. Furthermore, within even a single plaque there are different stiff and compliant components like fibrous, calcified, smooth muscle cells and lipid pools. Consequently, it is prohibitively hard to isolate a uniform region suited for uniaxial tension tests, which require a sample size at least 0.5×3.0 mm^2.

As a result, for a reliable mechanical analysis, we need to probe the tissue mechanical properties specifically and locally. This has emerged development of indirect measurement techniques like elastography and modulus estimation via inverse elasticity problem. Historically, these techniques emerged from palpography, and later their application was extended to identification of mechanical properties and eventually analysis of plaque rupture.

In palpography, a physician touches patient tissue, and if he/she observes any abnormality in tissue stiffness he can expect it to be a sign of some malfunctioning behavior of tissue. In other words, often changes in tissue associated with a disease result in varied mechanical properties and provides us with an indirect technique to test tissue healthiness. Palpography has been an important and simple non-invasive test for detection of breast cancer. However, human fingers have limited sensitivity and usually miss early, deep or small cancer nodules. Consequently since 1990, the palpography concept has been exploited via elaborate imaging systems and a major effort has been focused on developing related techniques to more accurately and quantitatively analyze tissue stiffness. Ophir *et al.* proposed to measure the strain after a uniform load has been applied to the tissue. Hence, strain levels can reflect tissue elasticity and the strain image called "elastogram" can be interpreted for medical purposes[53]. This technique is called either elastography or palpography by alternative groups[54,55], with the corresponding image named as either elastogram or palpogram.

To relate elastogram to tissue elasticity, it is typically assumed that the tissue is experiencing a uniform load, for example by a uniform boundary pressure, causing uniaxial compression. However, first this uniform load can only be applied in boundaries and in fact in most cases instead, a uniform displacement condition is imposed via rigid compressors. Furthermore, even if we apply a uniform stress at boundaries, the presence of inclusions or nodules will change the stress fields; consequently strain levels are not linearly related to tissue elasticity. Hence, the elastogram has several artifacts like target-hardening and stress concentration near inclusions[56]. These artifacts can be avoided when there is only a single inclusion, but when there are several inclusions or the noise level increases, it becomes hard to distinguish between real inclusions and artifacts.

Consequently, several groups have proposed to reformulate the problem as an inverse problem (IP), in which we know the boundary conditions and inside displacements, and we seek to find the elastic properties[57-60]. This is called the Inverse Elasticity Problem (IEP) as opposed to the Direct Elasticity Problem, in which we know the material properties and boundary conditions, and we seek to find the displacement field. As summarized in Fig. 1-4, the solution of IEP provides us with elastic modulus field, which can be interpreted as another image beside elastogram. IEP can be cast as a general parameter estimation problem, and we will discuss it further in the next chapters.

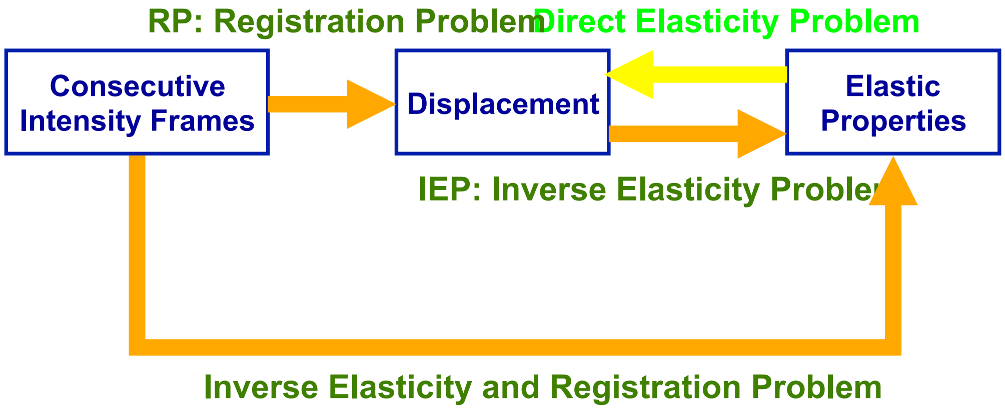
RP: Registration Problem
Direct Elasticity Problem
Consecutive Intensity Frames
Displacement
Elastic Properties
IEP: Inverse Elasticity Problem
Inverse Elasticity and Registration Problem

Figure 1-4: Schematic depicting conventional procedure to solve the inverse elasticity problem following registration problem. In this thesis, we present a new method to directly relate elastic properties to the image frames (IREP: Inverse Elasticity and Registration Problem).

Elastography and modulus estimation has been successfully applied to various tissues and organs. Elastography, for the first time, was utilized for *in vivo* imaging of the breast tissue and skeletal muscle[61-63]. In addition, the elastography community has focused on prostate cancer diagnosis[64-67]. Conventionally, ultrasound modality is used for elastography, but MRI (magnetic resonance imaging) is also emerging as a successful modality for elastography. MRI elastography (or viscoelastography) uses a similar approach, but instead of elastic properties, it measures viscoelastic properties of a tissue imposed to shear wave vibrations[68].

1.5 Thesis Plan

In Part I, Chapters 1-3, we describe and develop models for μm to mm-sized tissue elasticity analysis. In particular, we focus on how to register two images by incorporating tissue mechanics as side constraints in the registration process. The eventual output of our results will be elastic modulus for a given region of the material. In Part II, Chapters 4-5, we focus on hydrodynamic interaction (HI) phenomenon, and eventually utilize it for viscoelastic loss modulus of actin network, the primary component of the cytoskeleton, in the nm to μm size range. Taken together, this thesis covers viscoelasticity at different scales for both tissues and cell constituents. Initially, we use experimental top-down approach in Chapters 2 and 3, and finally in Chapters 4 and56, we use theoretical bottom-up approach.

1.5.1 Part I-Elastic Moduli Estimation with Image Registration and Inverse Elasticity

Part I of this research aims to develop new imaging and image processing techniques for assessment of arterial diseases such as atherosclerosis. By developing elastography and modulus estimation techniques we will have:

1. New images based on strain/stress and modulus distribution.
2. Local elastic properties of arteries as a highly non-homogenous material: these data can be used for further biomechanical analysis and simulations.
3. Third and finally the most important one: a risk assessment technique based on more realistic values of higher levels of stress/strain instead of relying only on the geometry.

While, the elastography can be applied to different imaging techniques, here we focus on its application to optical coherence tomography (OCT) as our imaging modality of the best interest. Optical coherence tomography provides high resolution, high contrast image of arteries and seems as a promising modality for atherosclerosis diagnosis[69]. Optical coherence tomography is also capable to distinguish tissue types directly, which can be used as a priori-information for image analysis[70,71].

As stated by now, the Chapter 1 of thesis dealt with background information and tried to provide a brief review about arterial biomechanics and atherosclerosis. Interested readers are encouraged to follow up our references for further information.

The Chapter 2 deals with mathematical background of this work. Initially, our mechanical model is explained and later a code to create finite element models (FEM) is verified. Next, inverse elasticity problem is explored and then it is linked to registration problem. New techniques for simultaneous solution of inverse elasticity problem and registration problem are provided there. After that, we explore different regularization techniques thoroughly. Finally, at the last section of that chapter, numerical techniques to solve the problem, including adjoint and Newton methods, are briefly discussed.

The Chapter 3 presents some of our results about inverse and registration elasticity problem. Initially, it tries to investigate the feasibility of elastography and modulus estimation of arteries based on a perfectly registered displacement field. First, the implemented method is verified and then the code efficiency is discussed. Then, we try to answer whether it is possible to reconstruct the complicated modulus field or not. It should be noted that the conventional elastography deals with breast cancer nodules, in which we have an isolated large inclusion surrounded by a background within the same order of the elasticity. On the other hand, in arteries we have fatty streaks, several plaques and etc., which shape a complicated modulus field. Furthermore, elastic modulus of plaques covers different order of magnitudes and this brings an extra complexity in arterial elasticity reconstruction. We also try to identify limiting bounds on registration problem. Uniform strains and rigid body displacements are of especial interest because they can characterize the noise effect on image registration. Later, we deal with simultaneous solution of image registration and inverse elasticity problem. The findings from previous chapter, as two ideal cases, are utilized for further analysis of the results and assessment of benefits, disadvantage and limits of our techniques. The method is applied to artificially generated OCT images, real phantom images and an ascending aortic sample under *in vitro* uniaxial stretch.

1.5.2 Part II-Viscoelasticity of Actin Networks, Dependence on Hydrodynamic Interactions

In Chapter 4, we begin by introducing the concept of the hydrodynamic interactions. We present the standard bead method, based on discretizing filaments into side-by-side stacked spherical beads. We use Rotne-Prager tensor for hydrodynamic interactions and briefly review other tensor forms. We cover various methods to compensate for the discretization errors due to geometrical difference between stacked spheres and a cylinder. Next, we introduce an optimal bead method, where instead of spherical beads, we use disk-shaped beads to build an exact cylindrical filament. Then, we introduce the Swanson-Batchelor formulation to calculate the drag coefficients of filament at both large and small aspect ratios. Next, we develop a new simplified rod method to account for HIs. The method uses Swanson-Batchelor formulation, mixed with Rotne-Prager tensor to calculate HIs between rod segments. We further quantify accuracy of this method and examine different candidates for its Stokes radius. The basic method and our new rod methods are used in the next chapter for analysis of HI effects in the mechanics of the cytoskeleton.

In Chapter 5, we begin by introducing the F-actin structure and its prominent role in cell mechanics. Next, we focus on the role of HIs on altering actin mechanics and dynamics at different length scales and structural levels. We begin by looking at the role of HIs at a single filament level in rigid body motion and diffusion, as well as filament lateral fluctuations. We specifically investigate how HIs can alter mode shapes or relaxation times. Next, we look at the HIs effect for aligning filaments during bundle formation. We study acto-myosin alignment for antiparallel filaments and crossed parallel filaments. We also study zipper action for aligning crossed filaments by invoking several passive crosslinkers. Later, we focus on the role of HIs in the network model. We begin by examining a regular 1D network and move toward a random physiological 3D network. In this part, we report the viscoelastic loss modulus and discuss its relation with the system size and the alternative poroelastic model. Finally, we introduce a 3D cross, as an idealized basic unit to build a regular 3D network, and find simple estimates on how loss modulus might be affected by HIs effect in a random 3D network.

At the end in Chapter 6, we summarize both Parts of this thesis. There, we conclude our work and provide a summary of research outcomes. We also try to shed light on future possible directions and other applications of interest.

Chapter 2: Mathematics of Elastography

2.1 Introduction

This chapter presents mathematical backgrounds required for elastography part of this thesis. In the beginning, we explain the mechanical model, introduce direct elasticity problem and verify our custom-built finite element modeling (FEM) code. Later, inverse elasticity problem is explored and then it is linked to registration problem. New techniques for simultaneous solution of inverse elasticity problem and registration problem are provided there. After that, we explore different regularization techniques thoroughly and finally, at the last section of this chapter, a brief review about numerical techniques to solve the problem, including adjoint and Newton methods, is presented.

2.2 Direct Elasticity Problem

Materials are divided to rigid or deformable ones. "Mechanics (of Materials)", as a branch of science, investigates how objects are deformed, when forces are applied to them. A special group of deformable materials are elastic materials, in which upon removal of force, objects go back to their original undeformed shape. Direct elasticity problem is the problem in which we seek to find how an elastic body will deform when a special set of loads are applied to it. This in turn relies on how a local loading (expressed as stress or force per unit area) will cause local stretch or strain.

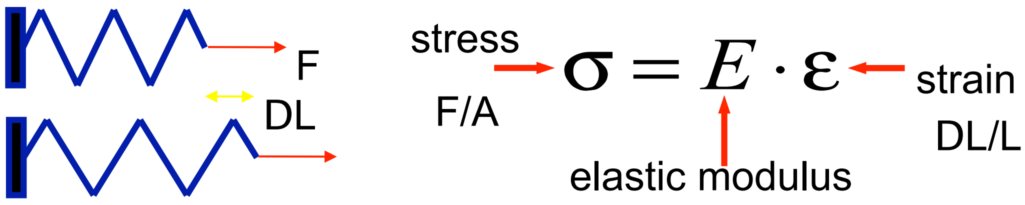

Figure 2-1: Simple depiction showing relation between force/displacement with stress/strain. A: Area, L: Length.

Stress and strain are the macroscopic versions of force and deformation due to displacement, as shown in Fig. 2-1. The relation between stress and strain is called stress-strain constitutive relation. This relation and boundary conditions (including loads) are known in the direct elasticity problem and we want to compute the displacement field. However, sometimes we know how an elastic object is deformed (as well as its original shape), and we are interested to know the stress-strain constitutive relation. The latter problem is called inverse elasticity problem. To solve the inverse elasticity problem, we assume a specific kind of constitutive relation and then we try to see if that constitutive relation can reproduce a displacement field similar to the observed displacement field. Consequently, to solve the inverse elasticity problem, we should be able to solve the direct elasticity problem for an *assumed* form of stress-strain constitutive relation.

In general, any experiment for computing elastic constants can be cast as an inverse elasticity problem. However, the inverse elasticity problem is usually used for non-homogenous materials, whose elastic constants are a field function (a function of spatial coordinates). On the other hand, for lumped models we have only a few unknowns as opposed to a field function. Hence, for a lumped model, we can estimate more complex (nonlinear) stress-strain relationships and yet rely on simpler numerical approaches like brute force or genetic algorithm, as employed by Karimi *et al.*[72] or Khalil *et al.*[73].

2.2.1 Stress-Strain Constitutive Relations for Vascular Tissues

Prof. Fung made major contributions to the field of biomechanics. He can be called the "the father of modern biomechanics"[74]. His books e.g., Biomechanics: Circulation or Biomechanics: Properties of Living Tissues[75,76], can be the best sources for getting a through understanding about cardiovascular biomechanics. Here we briefly summarize popular constitutive relations for cardiovascular tissue. However, interested readers are encouraged to study Fung's circulation book, or the newer book by Guccione *et al.*[77]. We have also discussed different relations for ascending aorta, based on our experimental data[78].

Various stress-strain constitutive relations have been utilized for different tissues. Relative slow motion of arterial tissues results in negligible inertial forces. Moreover, we have small strains when we consider two consecutive image frames of arteries. Furthermore, we can note that we have a rather stable periodic excitation by heart-beats and hence neglect stress relaxation or any other viscous behavior. Here we restrict ourselves to consecutive relations on which loading history, or strain rate, is not important. Nonetheless, we should be careful about how to interpret elastic constants, which indeed might refer to instantaneous, harmonic or relaxed loading.

The simplest constitutive relation between stress and strain is the linear relation, in which we have only two unknown constants namely μ, λ or Lame's constants as follows:

$$\sigma_{ij} = 2\mu\varepsilon_{ij} + \lambda\varepsilon_{kk} \qquad i,j = 1...3$$ Eq. (2-1)

$$\varepsilon_{kk} = \varepsilon_{11} + \varepsilon_{22} + \varepsilon_{33}$$ Eq. (2-2)

Here $\sigma_{ij}, \varepsilon_{ij}$ refer to the components of stress and strain tensors accordingly. The above notation follows "Einstein's Index Notation".

Lame's constants can be expressed in terms of other linear elasticity constants, e.g., E, v or "Young's Elasticity Modulus" and "Poisson's Ratio". They both can be directly measured from experiments and related to the Lame's Constants:

$$\mu = \frac{E}{2(1+v)} = G \;\; G\text{: Shear Modulus}$$ Eq. (2-3)

$$\lambda = \frac{Ev}{(1+v)(1-2v)}$$ Eq. (2-4)

Poisson's ratio indicates that how a uniaxial stress generates transverse strains. In most loading cases, biological tissues are rather incompressible due to presence of water. Incompressibility condition can be expressed mathematically as $v \to 0.5$. Unfortunately direct application of this condition into equations leads to singularities in computing λ. The singularity introduces another unknown field (beside the displacement field), namely presser field, which is defined as follows:

$$p = -\frac{\sigma_{kk}}{3}$$ Eq. (2-5)

Some numerical approaches consider this second unknown field and use "u,p formulation" where u stands for displacement field. While this is the right approach, it is rather complicated and most authorities simplify it by just choosing a v not equal to 0.5, but very close to it like: 0.49, 0.499, 0.499, 0.4999 and so on. Due to presence of above singularity, this condition is extremely sensitive to problem type and truncation errors. Numerical solution might be stopped by a phenomenon called "locking" and finite element modeling can only be done by extra tricks and only through a few families of elements used for numerical discretization[79,80]. This is beyond the scope of this brief review and interested readers are referred to above references.

Here we try to follow the guideline given for this case without using “u,p formulation”.

By assuming a known value for Poisson’s ratio, we are left with only one unknown in our constitutive relation, which hugely simplifies the inverse elasticity problem. Due to the difficulty of the inverse elasticity problem and also troubles associated with its solution uniqueness, almost all groups have used a linear isotropic incompressible model as their constitutive relation[56,81-84].

A few researchers have also computed the Poisson’s field as well as Young’s or shear modulus field[85]. To the best of our knowledge, no one has ever tried to compute a nonlinear elastic field due to its complexity, but we have estimated the nonlinear mechanical properties of the lumped models[86]. In this work, we assume a linear isotropic incompressible model. However, to have a better understanding that where this model stands among other models describing vascular tissue mechanics, we will briefly review alternative models.

Deviation from linear isotropic incompressible non-viscous model comes primarily from these facts:

1. Anisotropic behavior: mainly originated from the directionality of the fibers composing tissue (e.g., collagen fibers).
2. High level of stress or strain: will result in nonlinear kinematics and tissue softening/hardening.
3. Viscous behavior: not of our interest but yet incorporated in apparent modulus for our period loading.

The anisotropic linear elastic behavior can be expressed by generalized linear elastic relationship:

$$\sigma_{ij} = C_{ijkl}\varepsilon_{kl} \quad i,j,k,l = 1 \ldots 3 \qquad \text{Eq. (2-6)}$$

Above relation incorporates 81 elastic coefficients, however Voigt inherent symmetries ensure that there are only 21 independent constants for the most generalize anisotropic linear elastic material. Moreover, if there exists one symmetry plane we will end up with only 13 coefficients. Furthermore, for an orthotropic material, i.e., having three mutually perpendicular symmetry planes, we have only 9 independent coefficients. Finally for a transversely isotropic material, we have only 5 independent coefficients.

An elastic isotropic tissue can have a macro structure composed of randomly oriented elements. On the other hand, when symmetric elements are oriented toward a specific direction we have a transversely isotropic behavior. This behavior is a good approximation for many tissues including muscle fibers. Unfortunately, unequal pre-stretches in the transverse directions can render a transversely isotropic material as an orthotropic one. This can be a common case for arterial tissues. Now we should think that what justifies our assumption of an isotropic behavior?

Problem complexity is the main reason for assuming an isotropic model. In fact, to estimate more constants, we need to observe our deformed shape under different (and independent) loading conditions[87,88]. However, in our application we have only one independent loading condition (varying blood pressure), and hence we almost have to restrict ourselves to one unknown. Nonetheless, it should be noted that the reasonable assumption of the plane strain in the axial direction of the arteries, can help us to not worry about the anisotropic behavior in that direction. We also have to restrict ourselves to small strains, mainly due to registration problems associated with higher strains like strain induced speckle decorrelation[89]. Despite the nonlinear behavior of cardiovascular tissue at large strains, a linear form can be derived for small strains. For example, the following model is a common generalized hyperelastic relation for soft tissue[75]:

$$W = \frac{C}{2}(e^{Q} - Q - 1) + \frac{q}{2}$$

Eq. (2-7)

In the above relation, W represents the strain energy density from which Cauchy stresses can be computed. E_{ij} are the components of the Green strain tensor[1] [90,91]. Q and q are both quadratic functions of E_{ij} with up to nine unknown coefficients. q accounts for linear elasticity, and Q accounts for nonlinear terms provided that the C coefficient is not zero. For initially isotropic material, the above relation can be simplified by using strain invariants I_i:

$$W = f(I_1, I_2, I_3)$$

Eq. (2-8)

Finally, for an incompressible tissue, we have $I_3 = 1$ and hence the strain energy function can have a simpler form. The most commonly used nonlinear model for the arterial component is the Mooney-Rivlin model, as follows:

$$W = C_1(I_1 - 3) + C_2(I_2 - 3)$$

Eq. (2-9)

---

[1] Cauchy stress: the load divided by the undeformed cross-sectional area.
Green strain: exact nonlinear strain based on undeformed coordinate system.
Green strain: exact nonlinear strain based on undeformed coordinate system.

In the above equation, C_1 and C_2 coefficients can be related to linear elasticity constants such as μ and λ [92]. Hence, by elastography at low strain and estimating the apparent modulus in that regime, we can still properly identify the material constants for nonlinear behavior.

2.2.2 Custom-Built Finite Element Software and its Verification

For an efficient solution of the inverse elasticity problem, we require direct access to the mechanical variables to differentiate them (i.e., to calculate gradients/Jacobian/Hessian for the numerical schemes). However, all commercial FEM software have limited output and we have to only rely on numerical differentiations based on perturbation analysis[93]. This perturbation analysis is erroneous and slow. Furthermore, while in a typical inverse elasticity problem we have fixed elements and nodes, in all iterations, FEM software starts from scratch to compute elemental stiffness matrices and to assemble them. Consequently, we opted to do our analysis based on a home-built finite element package. Direct access to the FEM matrices let us explore new numerical techniques such as adjoins that are faster[82,94]. This direct access and avoiding redundant FEM calculations enabled us to reduce the calculation time from 14 hours to 5 seconds, which means our technique can be utilized for live diagnosis.

Our FEM software is implemented mainly in Matlab (MathWorks, Natick, Massachusetts, USA) and uses Matlab for visualization as well as pre/post-processing. It can generate structured mesh for simple geometries, use 2D Delaunay triangulation, or import the mesh from alternative software (e.g., Abaqus, LS-Dyna, and Adina). Matlab will carry (stiffness) calculation for each element, but their assembly and the solution of the linear set of the equations can be carried out either in Matlab or a computational code written in C++. This C++ core communicates with the Matlab code with both *.mat files and text-files used for input setting. In summary, computationally intensive (and repetitive) work can be carried out in C++, but the algorithmically complicated yet computationally simple parts are carried out only in Matlab. With this collaboration between Matlab and C++, we can enjoy the benefits of both and reduce both the computational cost and the implementation cost in an optimal way.

FEM implementation mainly follows guidelines suggested by Bathe and Hughes books [79,80]. Our code is capable of solving linear and nonlinear 2D and 3D problems involving a given constitutive relation and inertial properties. All of these capabilities are verified against standard problems, and the convergence rates (versus mesh size) have followed the expected behavior. However, since we only use 2D modeling for the inverse elasticity problem, we only present verification problems related to the 2D implementation.

Our FEM code can utilized 3D Quad-27 elements, as well 2D elements such as Quad-9, Quad 8, Tri-6, and Tri-3 (triangular or quadrilateral elements). All elements types have passed the patch test as a necessary condition to ensure proper implementation. The patch test examines the code on a domain consisting of several arbitrary elements, where the exact solution is known. Typically, in mechanics, the prescribed exact solution consists of displacements that vary as linear functions in space (called a constant strain solution). The elements pass the patch test if the finite element solution is the same as the exact solution[95,96].

For all types of 2D elements, there are two options: plane strain or plane stress. In arterial mechanics, plane strain is commonly used for 2D modeling since arteries are relatively long and they do not experience any axial strain[37]. On the other hand, thin objects are usually modeled as plane stress in 2D modeling, because we ignore any stress perpendicular to their surface.

Each 2D element type is tested against constant axial strain (in two directions) and shear strain. Hence, each 2D element requires six patch tests to cover all stress cases ($2\times(2+1)=6$). For all element types, all series of patch tests have shown satisfactory results and relative errors around the numerical precision ($\sim 10^{-16}$ for double numbers typically used in Matlab). A typical patch test is demonstrated in Fig. 2-1.

Next, we examine elasticity problem for a plate in plane strain with a circular hole in the middle as depicted in Fig. 2-2-b. Equations of the linear elasticity in this case can be solved exactly and they can be used to examine the convergence rate of our implementation. In this problem, it is assumed that a uniform stress, σ_∞, is applied at infinity in X direction. However due to symmetry, we only model 1/4th of the hole located in the corner of a finite size square (6 times the radius of the hole). We apply prescribed displacement boundary conditions, based on the exact solution, to the straight edges and stress free boundary conditions to the curved edge.

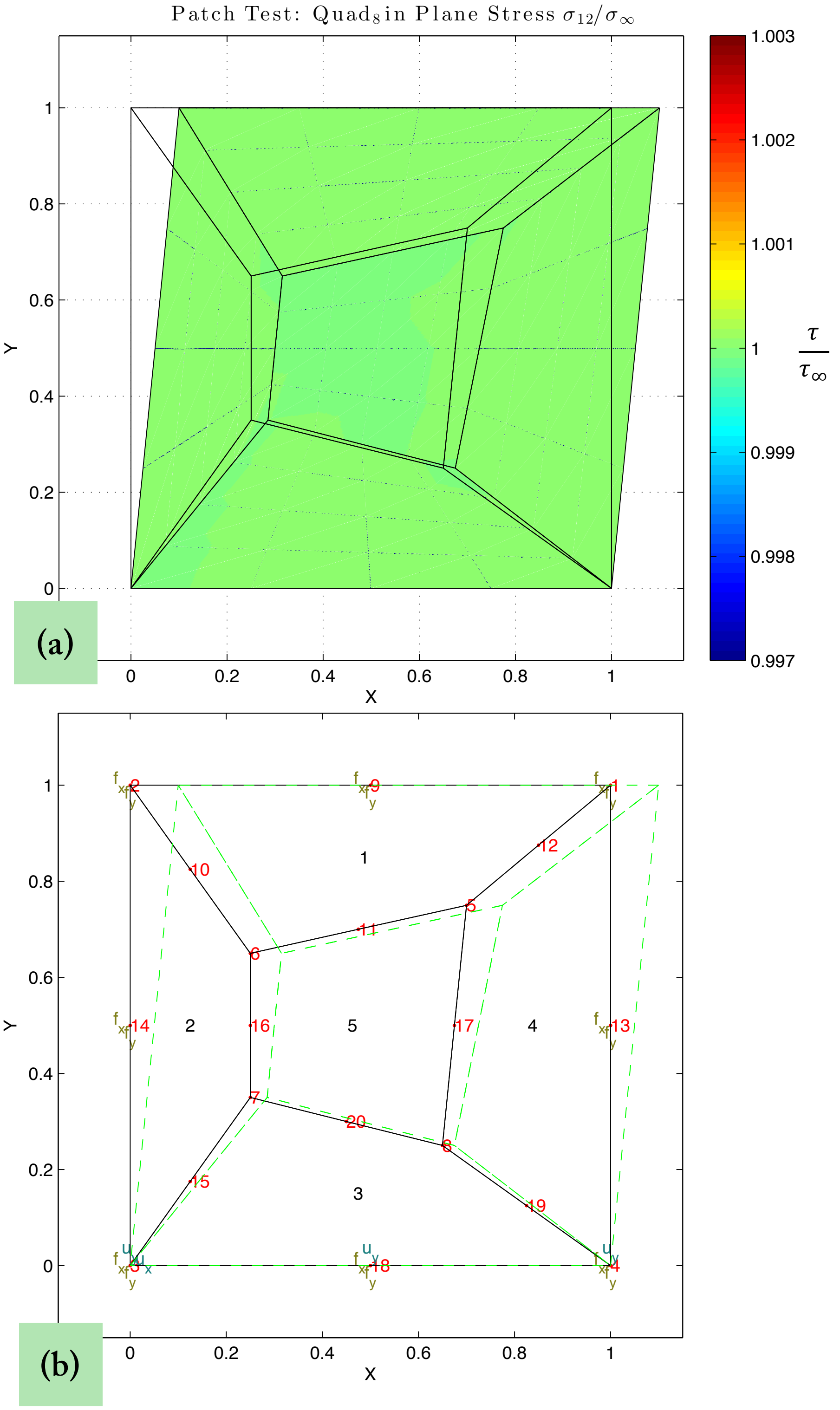

Figure 2-2: Patch test for the Quad_8 element in the plane stress and shear mode. (a): Normalized shear stress, (b): element and node indices as well as boundary conditions (red: node index, black: element index, f: force boundary condition, u: displacement boundary condition). Solution corresponds to $\boldsymbol{\nu = 0.3}$ and applied stress of $\boldsymbol{\tau/\mu = 0.01}$ ($\boldsymbol{\tau}$: shear stress). The deformations are scaled by 10 times.

According to the exact solution, maximum stress (or stress concentration: $\frac{\sigma}{\sigma_\infty}$) is 3 and it happens in the upper edge of the hole (where hole edge is parallel to the X direction). Furthermore, σ_{xx} is equal to zero at the lower edge of the hole (where hole edge is perpendicular to the X direction). Both these values of stress can be checked in the Fig 2-2-b. In fact, with refined mesh we have better matches for these values. Furthermore, convergence rate can be confirmed versus element order for different element types and in all cases shows satisfactory results. For example, energy error norm versus number of elements follows a quadratic form for our Tri_6 elements as expected for this quadratic element type (Fig. 2-2-a).

We also checked our FEM convergence for a singular problem. We modeled a crack in plane strain for an infinity large domain as depicted in Fig 2-3-b. The crack covers the entire negative X-axis. Despite the infinite size of the domain, in our FEM model, we only model a rectangular region. This rectangle has a length two times the length of the crack and a width the same size as the crack size (Fig. 2-3-c). We apply stress free boundary conditions to free edges and prescribed displacement boundary conditions to the rest of the edges based on the exact solution.

Due to singularity, an infinite stress concentration exists in the center (edge of the crack), and no matter how refined our elements become, we cannot fully model the stress pattern by simple FEM. Hence, the convergence rate of FEM will be slow and this can be checked in Fig. 2-3-a. Nonetheless, the stress pattern and contours are in accordance with the exact analytical solution (Fig. 2-3-c).

Above examples, and others not shown here, demonstrate that our finite element modeling and implementation are correct and hold satisfactory results. Next, we focus on the registration problem and describe how to use our finite element modeling to arrive at a model-based registration.

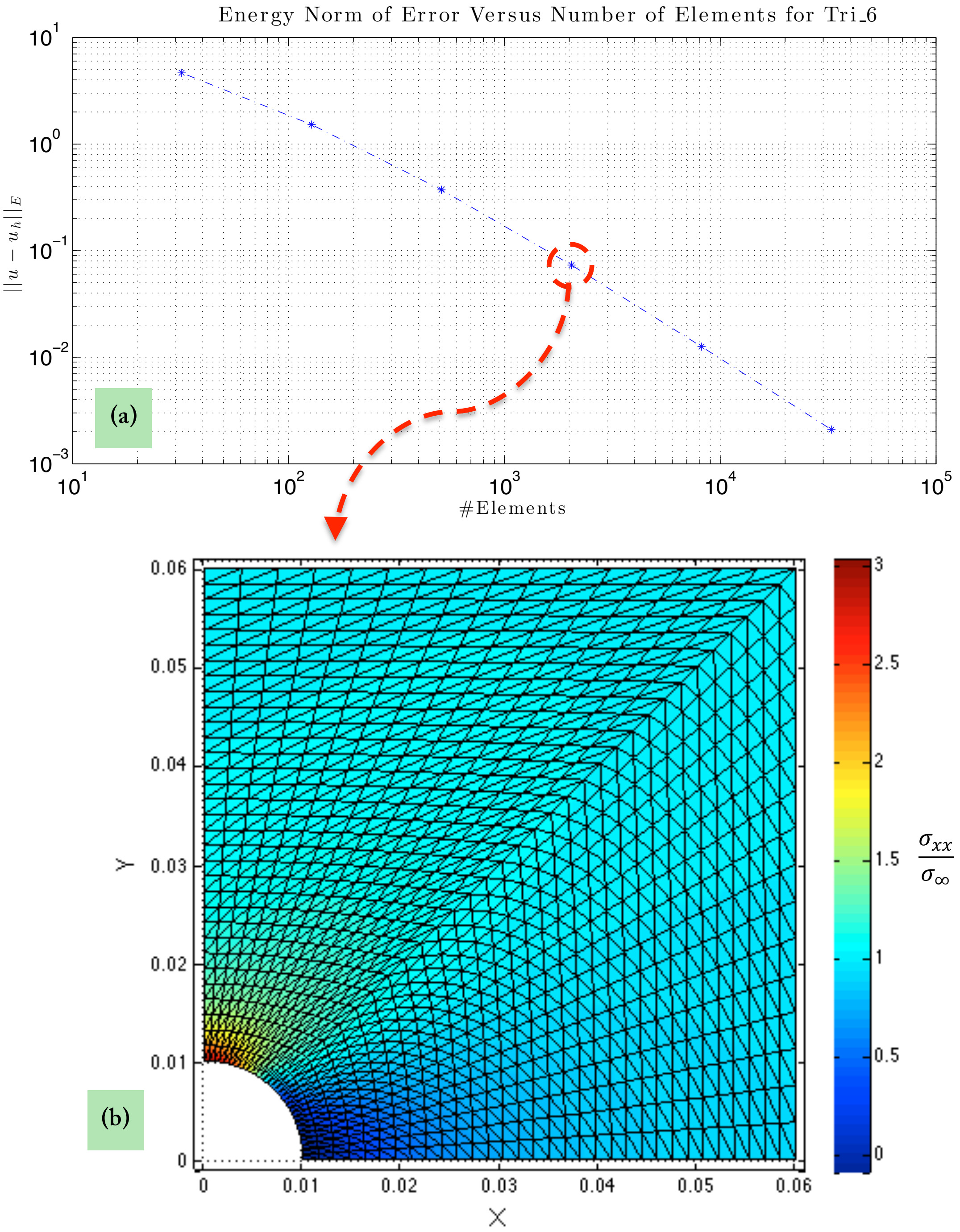

Figure 2-3: Stress concentration in a circular hole in plane strain. (a): Energy norm of error versus number of elements follows a quadratic form for Tri_6 element type, (b): Normalized $\boldsymbol{\sigma_{xx}}$ corresponding to the 4th data point in curve (a). Solution corresponds to $\boldsymbol{\nu = 0.3}$ and $\boldsymbol{\sigma_\infty/\mu = 0.01}$.

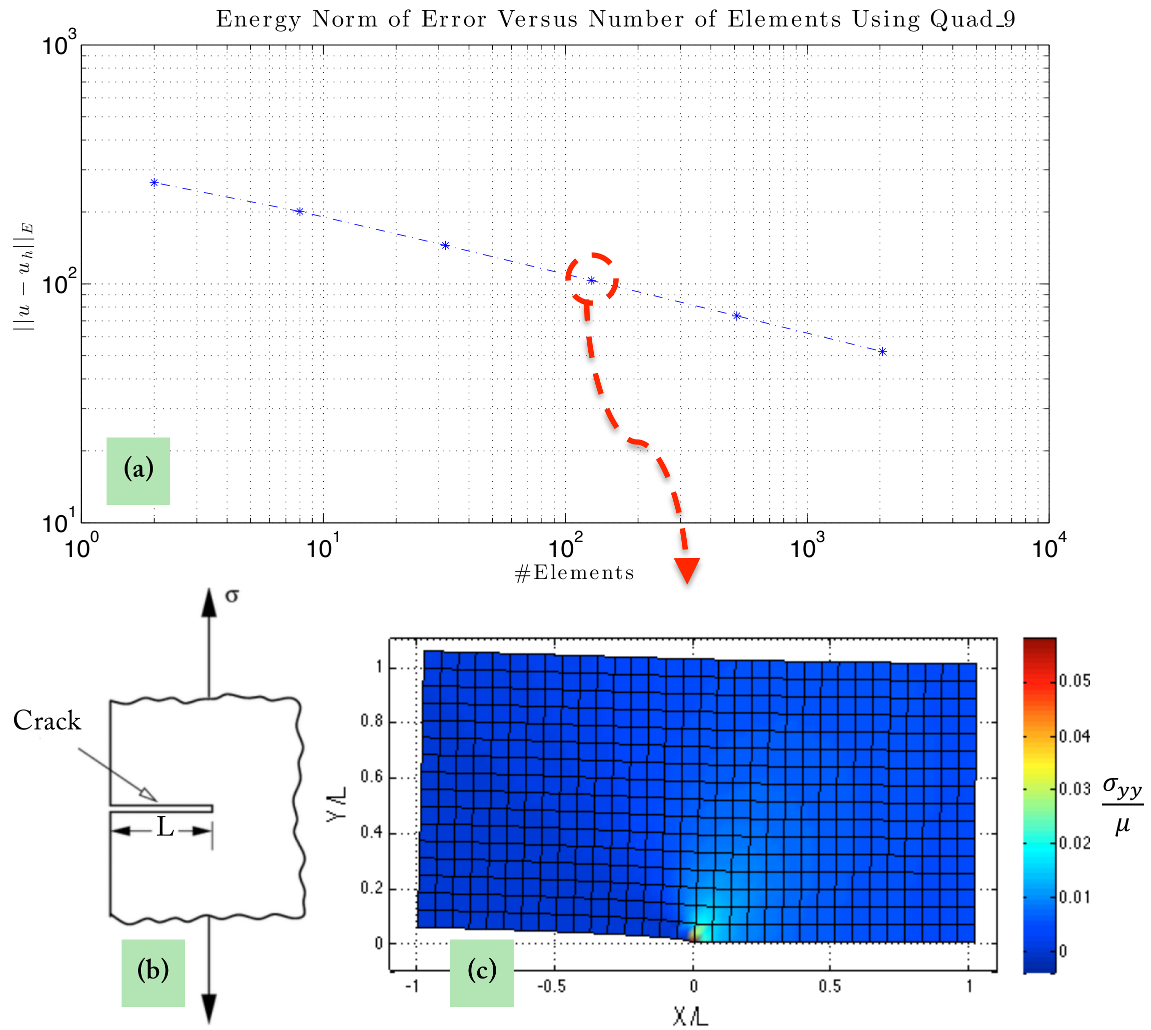

Figure 2-4: Stress pattern near a crack. (a): Energy norm of error versus number of elements shows a slow convergence for our Quad_9 element type, (b): Geometry and loading depiction, (c) Normalized $\boldsymbol{\sigma_{yy}}$ corresponding to the 4th data point in curve (a) plotted in the deformed configuration (10 times actual deformation). Solution corresponds to $\boldsymbol{\nu = 0.3}$ and $\boldsymbol{\sigma_\infty/\mu = 0.01}$.

2.3 Registration Elasticity Problem

We have shown the overall flow of information from the medical images to the diagnostic assessment in Fig. 2-4. Typically, images are registered to find the displacement field. At the same time, images are segmented and a mechanical finite element model is built to relate the displacement field to the stress values. The displacement field of this mechanical model is compared with the displacement field computed by the registration. Inverse elasticity problem is used to match both displacement fields by varying mechanical parameters. When we achieve a satisfactory match, we can rely on it to assess the stress field and use it for diagnostic purposes. Actual level of stress/strain/elasticity-modulus can be compared against indices describing severity of atherosclerosis plaques. These indices rely on geometrical data, easily observed in images, as well as chemical factors that can be measured by histological markers. For the verification purpose, we can perform histological sectioning of tissue *in vitro* and compare it with our mechanical vulnerability indices.

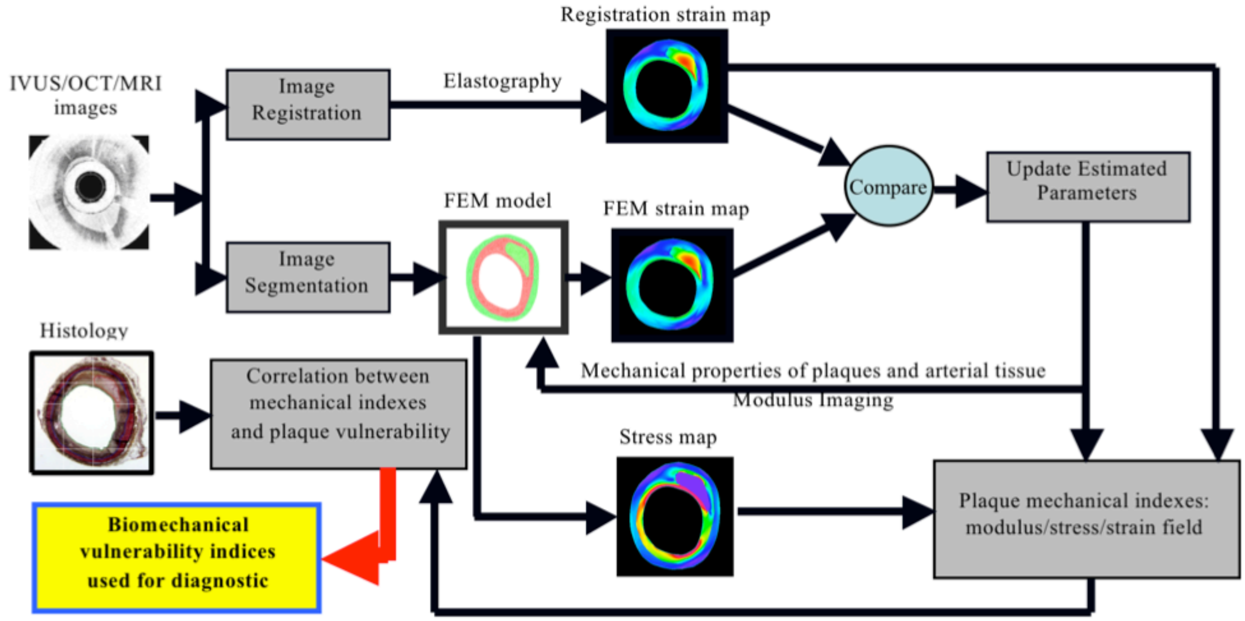
Registration strain map
IVUS/OCT/MRI images
Image Registration
Elastography
Compare
Update Estimated Parameters
FEM model
FEM strain map
Image Segmentation
Histology
Mechanical properties of plaques and arterial tissue
Modulus Imaging
Correlation between mechanical indexes and plaque vulnerability
Stress map
Biomechanical vulnerability indices used for diagnostic
Plaque mechanical indexes: modulus/stress/strain field

Figure 2-5: Overall flow chart of the elastography and parameter estimation procedures for arterial plaque characterization taken from Karimi *et al.*[72]. Frames of images, as obtained with IVUS/OCT/MRI modalities, are registered to find the strain map. The images are segmented to build a lumped mechanical model. Then an iterative scheme is used to match the strain computed by image registration and the mechanical model. Finally, when the process converges, a reliable strain/stress/modulus map is achieved. This map can be validated with histological markers of plaques (including their vulnerability level), and then can be used to build biomechanical indices for plaques vulnerability and evolutions.

Generally sequential frames are registered via block matching algorithms and then the resulting displacement field is further processed for the inverse elasticity problem (IEP). Conventional registration schemes typically produce poor displacement estimates[97,98]. In a previous work, our group developed a robust registration method that extensively improved elastogram estimates by exploiting kinematical constrains into registration[89]. Later, our group applied this robust registration technique to solve the IEP in uniform materials like hydrogels and elastic bands. There, we needed to iterate between two steps to justify the balance between regularization and data fidelity[93]. This motivated us to the current approach where we have unified both steps within a single framework. The new approach is computationally more efficient, and more importantly has better regularization characteristics resulting in more realistic solutions.

The improvements in the Chan *et al.* study were obtained by exploiting the kinematics of incompressible tissue as side constraints within the registration process[89]. In block matching, the displacement is solely computed by image correlation, while he also penalized strain non-smoothness as well as incompressibility of the displacement field. Building on this foundation, here we proceed to incorporate FEM-derived mechanics directly into the registration process. In other words, earlier we only penalized kinematically impossible motions, while here we restrict our registration to produce kinetically feasible motion with a minimum number of unknowns.

Elastic energy has been used extensively for regularization in the image registration in the past[99]. However, in our new approach, we reduce the number of independent displacement unknowns. We limit our unknowns to the displacement of the perimeter nodes, and relate the motion of the internal nodes to the boundary nodes via an elastic model. Similar ideas have been applied to the ultrasound data[100,101] and in all of them, including multi-resolution[89,99], the number of unknowns has been decreased in the beginning. Indeed, with gradual increase of the unknowns (in another words the solution's degrees of the freedom), we can better monitor the solution progress and ensure that it leads to a realistic and physically meaningful answer. Limiting the number of unknowns to the boundary nodes significantly reduces the computational cost by decreasing the spatial dimension of the unknowns (i.e., instead of having nodes in all areas of the 2D image, having them only on the 1D perimeter).

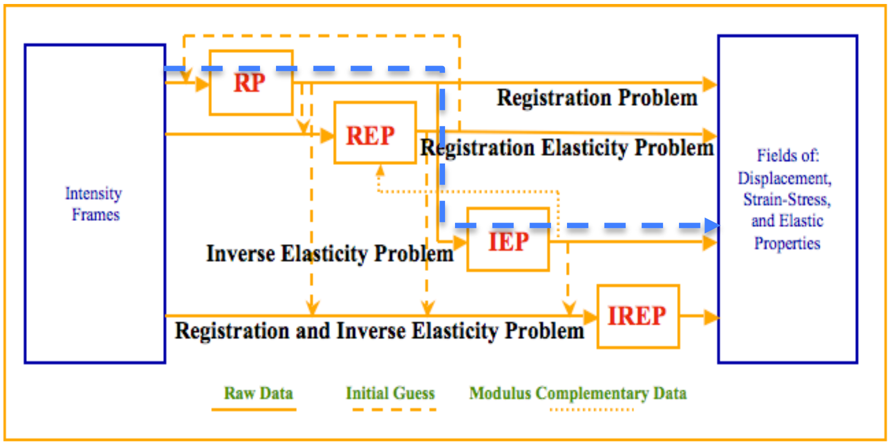
Intensity Frames
RP
REP
IEP
IREP
Registration Problem
Registration Elasticity Problem
Inverse Elasticity Problem
Registration and Inverse Elasticity Problem
Fields of: Displacement, Strain-Stress, and Elastic Properties
Raw Data
Initial Guess
Modulus Complementary Data

Figure 2-6: Different steps for processing intensity frames for extraction of displacement, strain, and even stress or moduli. Note that how each simpler step might help in initializing more complicated steps. Solid dashed blue line shows a typical IEP (inverse registration problem); it starts from RP (registration problem) and ends by computing moduli.

A careful plan is required to relate intensity images to the mechanical parameters. In one side, we have intensity frames and in the other side, we are looking for displacement, strain, stress and elastic properties as depicted in Fig. 2-5. All information is derived from images, but its fidelity and utility depends on how smart the registration. In other words, the registration should circumvent image noise and the potential local minima to achieve at useful data. To ensure that the solution progresses accurately and quickly, we derive it from simple steps. All steps can be imagined as different combinations of registration and elasticity problem. Accordingly, we define a series of terminologies, each corresponding to a single step in the solution progress:

- RP - Registration Problem: finding the displacement from the intensity frames based on either pure block matching or a block matching with kinematical constraints.
- IEP - Inverse Elasticity Problem: finding elastic modulus from the displacement.
- REP - Registration Elasticity Problem: finding the displacement of the boundary nodes from the intensity frames based on block matching (possibly including kinematical constraints) while internal points move according to an elastic model.
- IREP - Registration and Inverse Elasticity problem: same as REP but elastic modulus also varies.

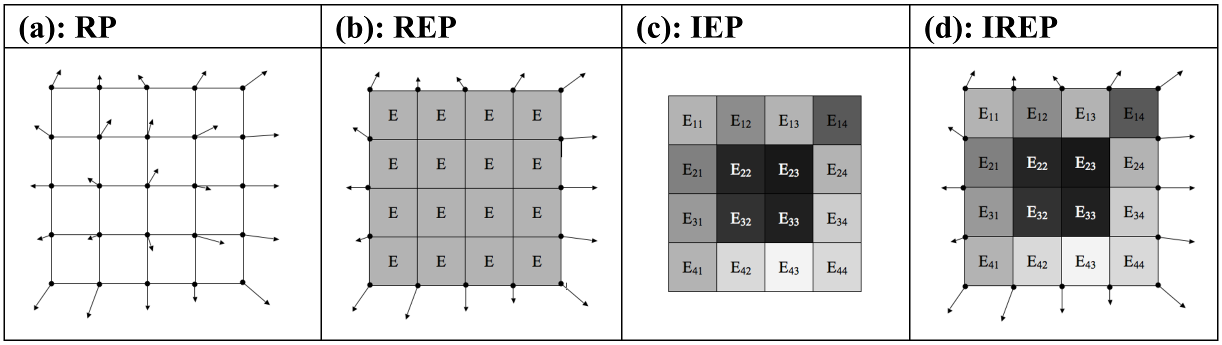
(a): RP
(b): REP
E
(c): IEP
E_{11} E_{12} E_{13} E_{14}
E_{21} E_{22} E_{23} E_{24}
E_{31} E_{32} E_{33} E_{34}
E_{41} E_{42} E_{43} E_{44}
(d): IREP

Figure 2-7: Different problems in a 4x4 grid. Each arrow represents an unknown displacement vector. In RP, all nodal displacements are included in the unknown variables and there is no need for a mechanical model. IEP is based on a totally known displacement (possibly from RP), but unknown moduli. In IREP and REP only boundary nodes are considered as unknown displacements. However, IREP is based on unknown moduli, but REP is based on a known (e.g., homogenous) moduli.

These different steps correspond to different sets of the unknowns as depicted in Fig. 2-6. The conventional elastography is a non-penalized (no kinematical constraints) RP followed by an IEP. In RP, we only compute strain filed; but in IEP, REP or IREP we also compute stress. Furthermore, in IEP or IREP we can compute the elastic moduli, while in REP we need to know elastic moduli in advance.

IEP uses displacement of a registered image to compute elastic field, while RP, REP, and IREP use similarity measure for registration of two frames. RP is based solely on kinematics, so it varies displacement at every node. On the other hand both REP and IREP use a mechanical model for registration and vary only displacement of boundary nodes. However, REP uses a given (uniform) elasticity field, while IREP in a scheme similar to IEP, computes its own elasticity field. REP technique alone can be used as a fast registration scheme; and furthermore it can be used to initialize RP and to eliminate the need for multi-resolution initialization of RP.

All these problems are cast as a one/multi-step nonlinear optimization problem and then they can be solved with BFGS (Broyden-Fletcher-Goldfarb-Shanno) optimization scheme[102]. It is vitally important to properly initialize these high dimensional optimization problems. Hence, in all cases we first find an average displacement (all nodes have the same displacement) corresponding to a rigid body displacement. Sometimes, we start the optimization at different initial conditions covering a rectangular grid around zero displacement. Varying initial conditions ensure that the average displacement calculated is around the right value.

Secondly, we find the displacement field corresponding to the uniform (incompressible) strain case and then we use it to initialize RP, REP or IREP. In fact, we apply a uniform stress/strain and this uniform strain initiates the full registration problem with values that ignore non-homogenous elasticity (for a homogenous material, a uniform strain results in a uniform stress and vice versa). Interestingly, our rigid and uniform body displacements usually reduce the number of iterations required for the registration problem by 3 fold. Hence, they significantly contribute to reduction of the computational cost, and furthermore, they ensure that the solution progresses in the right channel.

The former two steps, average displacement and average uniform strain, are not shown in Fig. 2-5. However, in that figure we show that how each simpler step can be used to initiate (provide initial value for the optimization) more complex schemes. For example, REP has fewer unknowns than RP and by assuming a known (uniform) elastic modulus we can solve REP and initialize RP. Later, RP solution can be used to solve IEP. Then we might rely on modulus computed from IEP to redo REP; however instead we can follow REP with IREP and simultaneously find the modulus field and the boundary displacements that maximize image similarities. In this way, IREP produces the best answer and we are ensured that it is properly initialized.

2.3.1 Formulation

Here, we present the mathematical formulation for all above problem. We model all of them within a vibrational framework, and then use optimization techniques to solve those problems. Registration problem is solved on a specific region of interest, called $\Upsilon,$ which is fully captured in all sequential frames. This region should have low imaging aberrations and a high signal to noise ratio (i.e., be near surface).

Here, the formulation is presented for the 2D (two dimensional) case, but can be easily extended to the 3D cases. Image similarity is measured based on cross correlation. The study by Chan *et al.* provides a detailed explanation of cross correlation theory for OCT (Optical Coherence Tomography)[89]. We utilize the final version of their results and extend it to include kinematical constraints:

$$\rho_{x,y}(u,v)=\frac{\int_{SB}\left[I_R(x'-x,y'-y)-\bar{I}_R\right]\left[I_S(x'-x-u,y'-y-v)-\bar{I}_S\right]dA}{\left[\int_{SB}\left[I_R(x'-x,y'-y)-\bar{I}_R\right]^2 dA\int_{SB}\left[I_S(x'-x-u,y'-y-v)-\bar{I}_S\right]^2 dA\right]^{1/2}} \qquad \text{Eq. (2-10)}$$

x and y are spatial coordinates of image points (i.e., pixel indices). $dA = dx'dy'$ is an area differential. SB is the sub-block, kernel, window, or template wherein cross correlation is computed (all dA put together). I is the image density (pixel value) and $\bar{I}$ is the average density within each SB. S and R refer to the sample and reference images. $\rho_{x,y}(u,v)$ is the normalized cross correlation at x,y; when SB has moved an amount equal to u,v from the reference frame to the sample frame.

Cross correlation is computed efficiently with FFT (fast Fourier transform) for some discrete levels of possible motions of a node (within a small block) before iterations. During registration iterations, for a given u,v values, $\rho_{x,y}(u,v)$ and its derivative with respect to u and v are computed by cubic interpolation from initially calculated discrete levels of $\rho_{x,y}(u,v)$. Currently, image is discretized into different nodes and image similarity is based on a summation of $\rho_{x,y}(u,v)$ value at different nodes. Alternatively, given a displacement field, sample frame can be transformed into the reference position, and then, image similarity can be computed based on the difference of the intensity between the reference and the transformed sample frame. We can use either sum of squared differences (SSD) or sum of absolute differences (SAD), both covering all pixels inside the region of interest Υ. However, sum of absolute differences (SAD) is slower and is not well aligned with optimization techniques.

All costs are integrated over, and normalized by, Υ area ($A = \int_{\Upsilon} dA$). As a result, weights are image size independent and we can easily manipulate different mesh densities at different locations or have different grids for image and finite element model. For example, E_s or similarity energy is defined as:

$$E_s(V(x,y)) = -\int_{\Upsilon} \rho_{x,y}(u,v)dA \,/ \int_{\Upsilon} dA = -A^{-1}\int_{\Upsilon} \rho_{x,y}(u,v)dA, \quad dA = dxdy \qquad \text{Eq. (2-11)}$$

V is the displacement function (i.e., $V(x,y) = [u(x,y) \quad v(x,y)]$), corresponding to the vectors of all nodal displacements for the discrete case. The pure block matching can be cast as an optimization problem (Eq. 2-12), in which $\hat{V}$ is our best estimate of the displacement minimizing similarity energy (or maximizing image similarity):

$$[\hat{V}] = \underset{[V]}{\arg\min}\, E_s(V) \qquad \text{Eq. (2-12)}$$

Next, we introduce kinematical constraints. The most important constraints are incompressibility and strain smoothness. Here, it is vitally important to have a formulation that can be represented by invariants of the strain tensor. Otherwise, the formulation will have inherent mathematical issues and the solution will depend on the coordinate system. The first and second strain or ε invariants ($\lambda_{i,\varepsilon}$) can be found as:

$$[\varepsilon] = \frac{1}{2}\left(\nabla V + (\nabla V)^T\right) = \begin{bmatrix} \varepsilon_{xx} & \varepsilon_{xy} & \varepsilon_{xz} \\ \varepsilon_{xy} & \varepsilon_{yy} & \varepsilon_{yz} \\ \varepsilon_{xz} & \varepsilon_{yz} & \varepsilon_{zz} \end{bmatrix}, \begin{cases} \lambda_{1,\varepsilon} = \varepsilon_{xx} + \varepsilon_{yy} + \varepsilon_{zz} \\ \lambda_{2,\varepsilon} = \varepsilon_{xx}\varepsilon_{yy} + \varepsilon_{yy}\varepsilon_{zz} + \varepsilon_{zz}\varepsilon_{xx} - (\varepsilon_{xy}^2 + \varepsilon_{yz}^2 + \varepsilon_{xz}^2) \end{cases} \qquad \text{Eq. (2-13)}$$

The first invariant must be zero for the incompressible case. Furthermore, for pure incompressible planar motion, when all “z” components of strains are zero, the second invariant can be simplified to $\lambda_{2,\varepsilon} = -\left(\frac{1}{2}\left(\varepsilon_{xx}^2 + \varepsilon_{yy}^2\right) + \varepsilon_{xy}^2\right)$. The $\lambda_{2,\varepsilon}$ term can be used to penalize high strain levels or to form an invariant for computing strain smoothness. Alternatively, $\|\nabla^2 V\|$ term can be employed to penalize high levels of the strain variation (this term is zero for uniform strain)[89]. The kinematical cost or energy, E_k, can be computed from below relation where α_i defines relative strengths of different constraints. In this relation, we have three α_i

values corresponding respectively to incompressibility, strain smoothness, and low-level strain constraints:

$$E_k(V) = A^{-1} \int_{ROI} \left[\alpha_1 \lambda_{1,\varepsilon}^2 + \alpha_2 \left\| \nabla^2 V \right\|^2 - \alpha_3 \lambda_{2,\varepsilon} \right] dA \qquad \text{Eq. (2-14)}$$

Above integrals are approximated by areal weighted summation of integrand value (summation at the center of elements in the discrete problem). To compute the strain smoothness, we compute areal weighted average of strain at nodes; and then we use finite element interpolations to compute the gradient of the strain at the center of elements. For the discrete case, with careful manipulation and selection of proper norms, we can assemble all terms as a quadratic function (of the displacement vector) prior to the beginning of the iterations. This prior term assembly accelerates the computation and simplifies E_k value to a single quadratic matrix form. This quadratic form incorporates the displacement vector and a sparse matrix with a bandwidth dominated by $\|\nabla^2 V\|$ term.

Regardless of the way E_k is computed, our penalized robust RP (Registration Problem) can be formulated as:

$$[\hat{V}] = \underset{[V]}{\arg\min} \left\{ E_s(V) + \beta_k E_k(V) \right\} \qquad \text{Eq. (2-15)}$$

Here, β scalar refers to the penalization strength. The kinematical cost can be also used for REP. In IEP, instead of similarity cost, we have a measured displacement, $\hat{V}_m$, and we define a quadratic energy/cost associated with the deviation from the measured displacement:

$$E_m(V) = A^{-1} \int_{\Upsilon} \left\| V - \hat{V}_m \right\|^2 dA \qquad \text{Eq. (2-16)}$$

In IEP, a smooth shear modulus field $\mu = \mu(x, y)$ is preferred. Consequently, we penalize shear modulus gradient:

$$E_{\nabla\mu}(\mu) = A^{-1} \int_{\Upsilon} \left\| \nabla \mu \right\|^2 dA \qquad \text{Eq. (2-17)}$$

Other constraints can be also included for shear modulus. For example, we might have an average guess for shear modulus and impose it similar to Eq. 2-16. Furthermore, in many cases we have only displacement boundary conditions, and hence, only a relative map of shear modulus (an arbitrary scale) can be computed[88]. However, to attain a unique solution, we might additionally employ the known value of the net force to estimate the energy of the deformation. This (average) energy can be used to find the right scale of the modulus. This constraint can be formulated as:

$$E_H(\mu,V) = A^{-1}\left(\int_{\Upsilon} h(\mu,V)\,dA - H_m(V)\right)^2 \qquad \text{Eq. (2-18)}$$

Where h is elastic energy density and H_m is the net external energy inserted to the system. This external energy can be simply computed by multiplying the (net) force with the net displacement at the boundaries. Alternatively, some studies have tried to impose a uniform stress boundary condition. However, our approach (Eq. 2-18) is more accurate, and does not restrict the field of view to be wasted on regions far from inclusion (where uniform stress boundary condition applies). Remarkably, we can omit Eq. 2-18 from below functional (i.e., set $\beta_H = 0$), and instead apply the scaling value suggested by it for the modulus after the termination of iterations. Finally, we can model IEP (Inverse Elasticity Problem) as below optimization problem:

$$[\hat{\mu}] = \underset{[\mu];\ \text{s.t. } V=V(\mu,\hat{V}_m)}{\arg\min} \left\{E_m(V) + \beta_k E_k(V) + \beta_{\nabla\mu} E_{\nabla\mu}(\mu) + \beta_H E_H(\mu,V)\right\} \qquad \text{Eq. (2-19)}$$

Note that in general the displacement can be expressed as a function $V = V(\mu, V_B, S_B)$, where V_B and S_B are the displacement and stress boundary conditions. However, we assume that S_B, like pressure, is accurately known and therefore omit it from the former functionals. Finally, note that for IEP V_B is a subset of already estimated $\hat{V}_m$, and consequently, we will have $V = V(\mu, \hat{V}_m)$ for IEP case. On the other hand for IREP, the V_B must be estimated as well, and hence, the problem can be formulated as:

$$[\hat{\mu},\hat{V}_B] = \underset{[\mu,V_B]\ ;\text{s.t. } V=V(\mu,V_B)}{\arg\min} \left\{E_s(V) + \beta_k E_k(V) + \beta_{\nabla\mu} E_{\nabla\mu}(\mu) + \beta_H E_H(\mu,V)\right\} \qquad \text{Eq. (2-20)}$$

By comparing Eq. 2-19 and Eq. 2-20, we can realize that IEP and IREP differ only in terms of independent variables as well as using E_s instead of E_m. Lastly, REP (Registration Elasticity Problem) can be stated as an especial case of IREP where we set $\mu = \mu_m$ (a known value for moduli) and we arbitrarily omit E_H from Eq. 2-20:

$$[\hat{V}_B] = \underset{[V_B]\ ;\text{s.t. } V=V(\mu_m, V_B)}{\arg\min} \left\{E_s(V)+\beta_k E_k(V)\right\} \qquad \text{Eq. (2-21)}$$

Again by comparing Eq. 2-15 and Eq. 2-21, we can realize that RP and REP differ only in terms of independent variable. REP looks for the displacement at boundary points, but RP independently varies the displacement of all points. Independent unknown variables of the RP, REP, IREP and IEP are all demonstrated in Fig. 2-6 showing the optimization variables used in Eq. 2-15, and Eq. 2-19…21.

2.3.2 Numerical Implementation

Former optimization equations should be solved for a discrete system. Image is discretized into pixels, and the elastic domain is discretized into nodes and elements. Consequently, integrals are replaced with summation over nodes/elements/pixels.

Lumped systems can have a larger variation in mechanical parameters. Khalil *et al.* have used the genetic algorithm to solve for linear properties, and we, Karimi *et al.*, have used it to solve for nonlinear properties[72,73]. However, here we have restricted ourselves to systems where elastic properties are a field function (non-lumped). A simple form of above equations can be solved by either Gauss-Newton method[93], or adjoint method[82]. Former references are a good starting point to learn how to calculate the gradients/Jacobi/Hessian by above methods.

Gauss-Newton method is a second order method. It has a faster convergence rate, but it is memory intensive. On the other hand, the adjoint method is a first order method and it is much faster per iteration[94]. While we have used both methods for simple calculations, we have indeed moved forward to utilize their idea only to calculate the gradients/Jacobi/Hessian values. We use those values in more advanced optimization algorithms. We have used both Numerical Recipe package in C++ and the trust-region constrained nonlinear optimization algorithm in Matlab. Interested readers are encouraged to look at above reference. Here, we will escape the confusing details applied to all different forms of the problem (Eq. 2-15, and Eq. 2-19…21). However, details can all be checked in scripts in the accompanying CD.

The core computational codes were implemented in C++ and we used parallel processing for vectors whenever possible. The assembly of the stiffness matrix takes the largest portion of the run time and is repeated in all iterations. The matrix is usually stored in a sparse row-column format. This format is characterized with slow search for the right column. To overcome this slow search for the column index, we made a vector referring to the vectorized position of our stiffness matrix in accordance to all incidences of assembly for all elements. As a result, the assembly was accelerated and was carried within a single loop.

Analytical formulation, custom-built FEM code, C++ implementation, FFT calculation of the image correlation prior to the optimization and several other modifications made it possible to achieve a 5 sec analysis time instead of 14 hours by Khalil *et al.*[93]. This fast computational time allows us to use our technique for live diagnosis and it cannot be achieved without properly taking into account all details described in this chapter.

Chapter 3: Elastography and Registration Results

In this chapter, we present some of our results about elastography and image registration. We try to proof the feasibility of the elastography to estimate mechanical properties. We focus on the atherosclerotic plaques with their complicated geometry covering several order of magnitude changes in elastic moduli.

Our algorithms are verified by published results of the elastography for ultrasound modality. With equivalent quality, our methods produced elastogram and modulus images tested by Kybic *et al.* for two different phantom gels as well a thyroid gland[101]. Our algorithms worked despite totally different nature. However, the ultrasound images usually are less noisy and have good speckle-correlation. Hence, here we will present results of our preferred imaging modalities, OCT (Optical Coherence Tomography)[69] and CARS (Coherent Anti-Stokes Raman Spectroscopy)[103], which are less studied and more challenging.

3.1 Inverse Elasticity Problem

A typical breast cancer nodule is an isolated large tumor. Furthermore, its elastic modulus is about the same order as that of the background tissue. However, as demonstrated in Fig. 3-1 atherosclerosis is a focal disease and plaques are not isolated objects. Not only they spread and cover a full region, but also, their shape and mechanical properties are more complicated. In this section, we assume that we have an accurate measured displacement field, and we will examine whether inverse elasticity problem can be tuned to investigate the mechanical properties of arterial tissue/plaques.

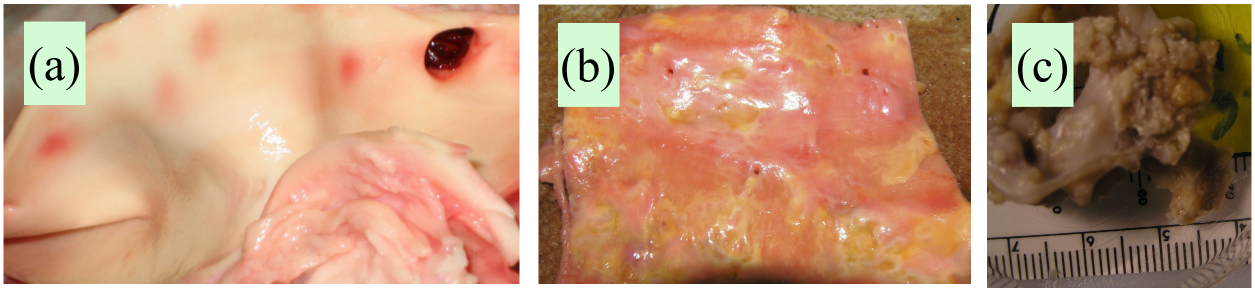

Figure 3-1: Human tissue: (a) interior aortic wall of a healthy sample, (b) interior aortic wall of a atherosclerotic subject died due to a cardiovascular disease, (c): atherosclerotic plaques in calcified fixed aortic valves (a surface similar to broccoli surface). Note the healthy smooth tissue versus rough arterial surface caused by atherosclerosis covering all nearby regions.

3.1.1 FEM model: mesh size and constitutive relation

We start by seeing whether the finite element mesh size has an effect in the inverse elasticity problem or not. We use CARS image, manually segmented by our collaborators in KRISS (Korean Research Institute of Science and Standards). In summary, CARS images are analyzed by these procedures:

1. Mimics program: it export CARS image to an image looking like CT or MRI. Then, the image can be meshed in Hypermesh program (2D and 3D are both possible). For reference, Mimics generates and modifies surface 3D models from stacked medical images such as CT, Confocal Microscopy, Micro CT, or MRI.

2. Hypermesh program: the images from Mimics are unclean and noisy. They cannot be directly used to generate mesh. Hence, they are modified neatly, and then, Hypermesh program generates meshes from corrected images.

3. Finite element program: ANSYS or ABAQUS analyze and simulate the stress/strain distribution for the meshed image. Mechanical properties should be provided for analysis.

A typical mouse carotid image, generated by z-projection (maximum projection) of the 3D stacks of CARS images, is shown in the Fig. 3-2-a. We have followed above procedure to segment and mesh the image. Then, we have imported the image into our custom-built FEM model as shown in Fig. 3-2-b. CARS imaging modality can identify different lipid structures, namely: lipid pools and needle/plate-shaped lipid crystals. These lipid structures and arterial wall are shown as different colors in Fig. 3-2-b.

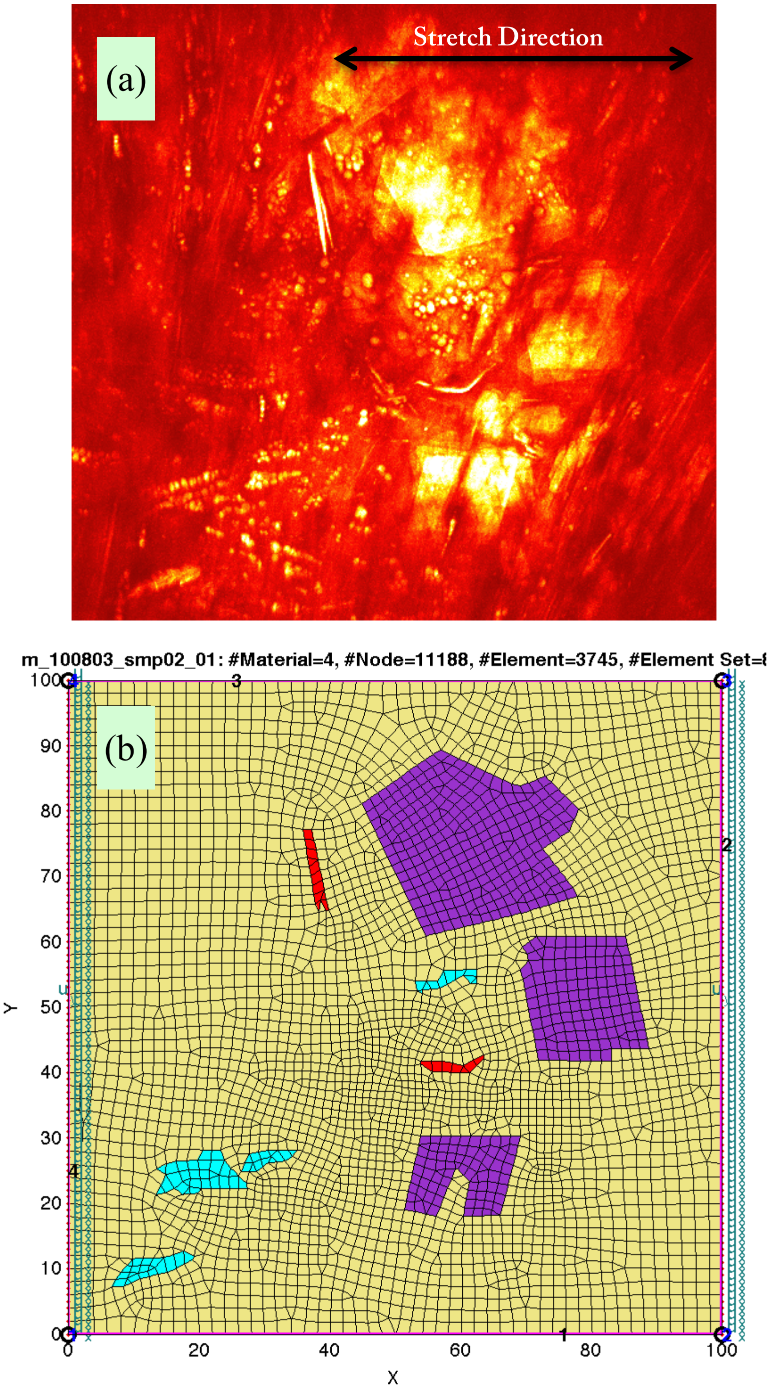
(a)
Stretch Direction
m_100803_smp02_01: #Material=4, #Node=11188, #Element=3745, #Element Set=
(b)
Y
100
90
80
70
60
50
40
30
20
10
0
X
0
20
40
60
80
100
1
2
3
4

Figure 3-2: Mouse carotid: (a) CARS image showing different lipid structures, (b) corresponding lumped FEM. Yellow: arterial wall, red: needle-shaped lipid crystal, violet: plate-shaped lipid crystal, cyan: lipid pool (appearing as bubbles in CARS image). Image in each direction has 512 pixels with a width equal to 0.25mm.

In this inverse elasticity problem, the measured displacement field are simulated by a direct elasticity problem corresponding to an artificial problem with no noise and 1% X-stretch in the boundaries (details in Fig. 3-2-b). This artificial problem corresponds to the finest possible mesh size (Fine 5), and its displacement field is compared against inverse elasticity problem from coarser meshes (Fine 1 to Fine 4). Linear elastic properties are arbitrary selected such that different moduli are sorted as below covering four orders of the elasticity:

$$E_{\text{lipid pool}} < E_{\text{wall}} < E_{\text{needle}} < E_{\text{plate}}$$

Our linearized elastic properties correspond to the Table 3-1 values used for nonlinear analysis in ABAQUS. We compared stress patterns in the linear model (estimated by the inverse problem via custom-built FEM in Matlab) with the nonlinear model (ABAQUS). We found that regions of highest von-Mises stress and its value are similar in both models, and hence, we conclude that linearized FEM does not look to compromise the highest stress values/locations commonly used as indices for the atherosclerosis risk factor.

Table 3-1: Material properties selected for nonlinear ABAQUS simulation corresponding to Fig. 3-2-b.

Material	Lipid Pool	Arterial Wall	Needle-Shaped Lipid Crystal	Plate-Shaped Lipid Crystal
Model	Hyperelastic C_1=0.01 MPa C_2=0 Eq. 2-9	Hyperelastic C_1=0.1 MPa C_2=0 Eq. 2-9	Linear Elastic E=4 MPa Eq. 2-1	Linear Elastic E=40 MPa Eq. 2-1

We also investigated the inverse-elasticity-problem convergence versus mesh size, as depicted in Fig. 3-3 and Fig 3-4. The coarsest mesh, Fine 1, does not converge, but finer meshes, Fine 2 to Fine 4, converge. Intermediate mesh size, Fine 2, converges quickly, which highlights the fact that a middle-size mesh should be selected to ensure a convergence (fine enough to capture image details) and a fast solution (coarse enough). However, in general, there should not be a problem for a fine mesh as long as we have enough computational power.

In this problem, we used Matlab trust region optimization functions and passed accurate analytical gradients to Matlab optimizers. Analytical gradient does not change accuracy significantly or does not improve stability for convergence. Interestingly, in several cases, hard-limit constrained optimization (fmincon function in Matlab) converges, while unconstrained version (fminunc function) does not. Consequently, hard-limits (e.g., Modulus is positive or is less than 1.0 GPa) can play important roles in the convergence; although, they are not typically included in the Gauss or adjoint methods.

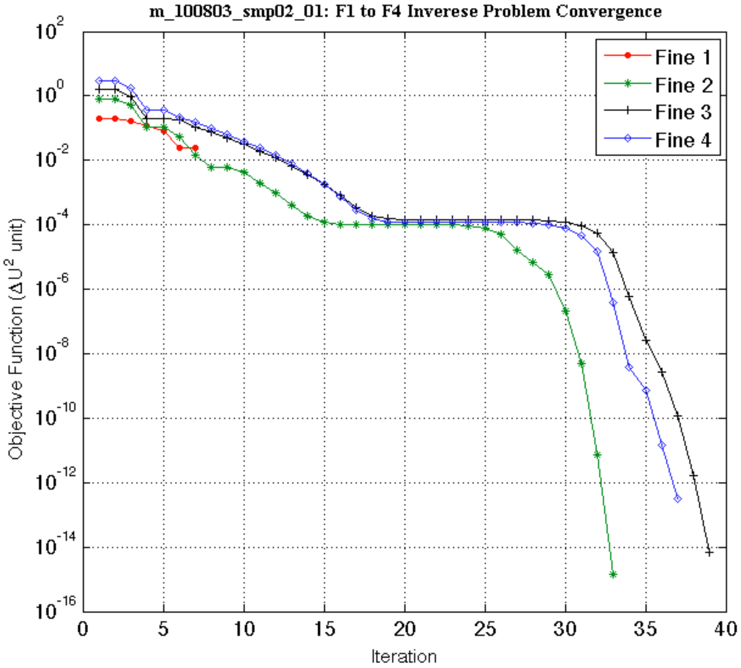

Figure 3-3: Convergence versus FEM mesh size for a lumped inverse elasticity problem in a mouse carotid corresponding to Fig. 3-2. Fine 1 to Fine 4 correspond to meshes becoming finer. Y-axis corresponds to the optimization functional (proportional to the sum of the squared differences between measured displacement and FEM inverse-elasticity-problem calculated displacements).

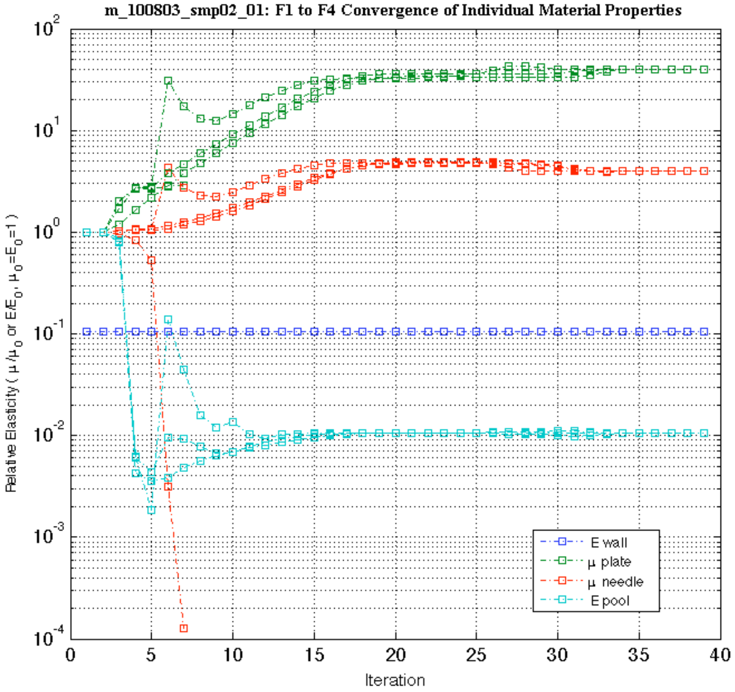

Figure 3-4: Convergence versus mesh size and iteration number for different lumped regions of Fig. 3-2-b. Note that compliant regions converge quickly and stiffer regions converge slowly.

3.1.2 Shape Complexity and Contrast Recovery Ratio

We used one of our own OCT images to find the shape of a typical plaque. Then, we meshed that image and generated several complicated low-contrast[2] shapes of shear modulus field (varying shear modulus for different elements). In all cases, our inverse elasticity algorithm converged qualitatively and quantitatively to the desired shear modulus field. One of these complicated shapes, alternative rows of hard and compliant tissue, is depicted in Fig. 3-5. We tested several element types and found that simpler elements (i.e., lower number of nodes) can converge better to the objective modulus field. In this simulation and the next one, we used BFGS optimization with the same parameters. Similar results were obtained regardless of the choice of Newton or adjoint method. We used prescribed displacement boundary conditions, and hence, we can only compute a relative shear modulus field. Following Eq. 2-18, shear moduli are normalized such that average moduli are constant, meaning that the net force is almost constant.

Given that we can recover complicated shapes of low contrast, we aimed at examining the high-contrast isolated small inclusions. This is important, because unlike (breast) cancer diagnosis by ultrasound in which big nodules are dangerous; in arterial wall thin plaques/shoulders are unstable and threatening! We varied contrast ratio, elastic modulus ratio of inclusion to the background, from 0.01 to 100 covering four orders of the magnitude as expected for arterial plaques. Compliant inclusions were identified accurately, meaning that they have a contrast recovery ratio approximately equal to 1.0 . However, stiff inclusions are not identified as well, and we have shown their recovery for ratio of 10 and 100 in Fig. 3-6. For the ratio of 10, the computed contrast is 10.39, and for the ratio of 100, the computed contrast is 30.86 (contrast recovery ratio equal to 1.039 and 0.3086). The reduction in contrast recovery ratio can be related to two phenomena. First, given that our normalization ensures a constant average modulus, a uniform initial guess is close to the final solution for a compliant inclusion. However, for a stiff inclusion, the solver should go several rounds to increase the inclusion stiffness at the cost of substantially decreasing the background stiffness. Secondly and specially in real problems, a stiff inclusion's deformation is relatively small compared to the background, and hence, its registration is difficult and erroneous. Similarly, due to small displacements, it will have a small role in the functional, and hence, its accuracy can be totally compromised against other terms. Nonetheless, arterial plaques are usually compliant lipids, and hence, this error can be avoided. Interestingly, as evident from Fig. 3-4 even for a lumped model, elastic moduli of the compliant regions are found first.

---

[2] Contrast refers to the inclusion/background ratio of the elastic modulus. In a low-contrast image, the inclusion and the background have approximately the same moduli.

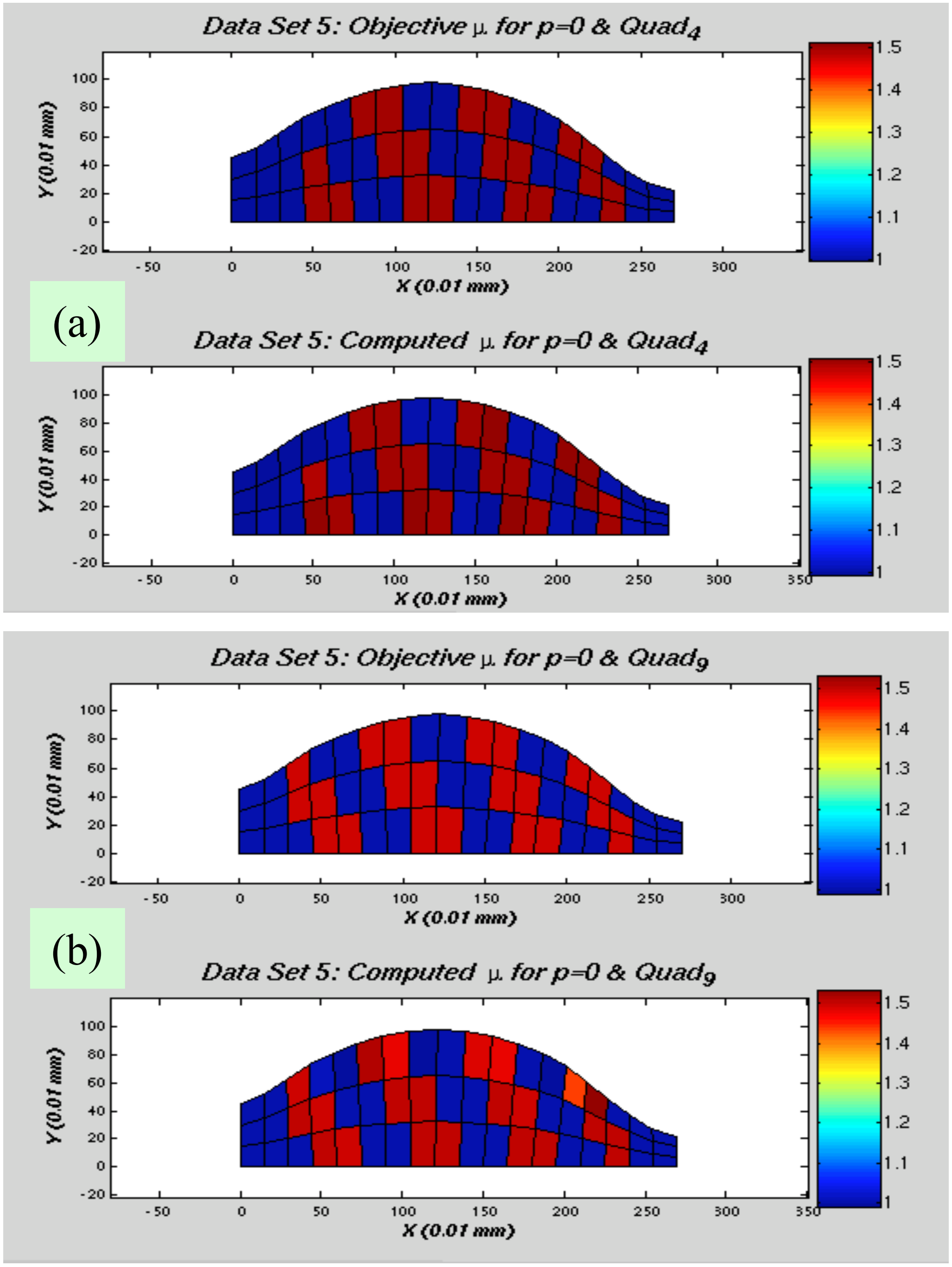

Figure 3-5: Recovery of a complicated low-contrast objective (shear) modulus in the invers elasticity problem for (a) Quad_4 elements and (b) Quad_9 elements. In each case, objective moduli is shown on the top figure and the calculated moduli is depicted in the below figure. Colorbars show relative shear moduli. Axis units are in pixel and each pixel is equivalent to 0.01 mm.

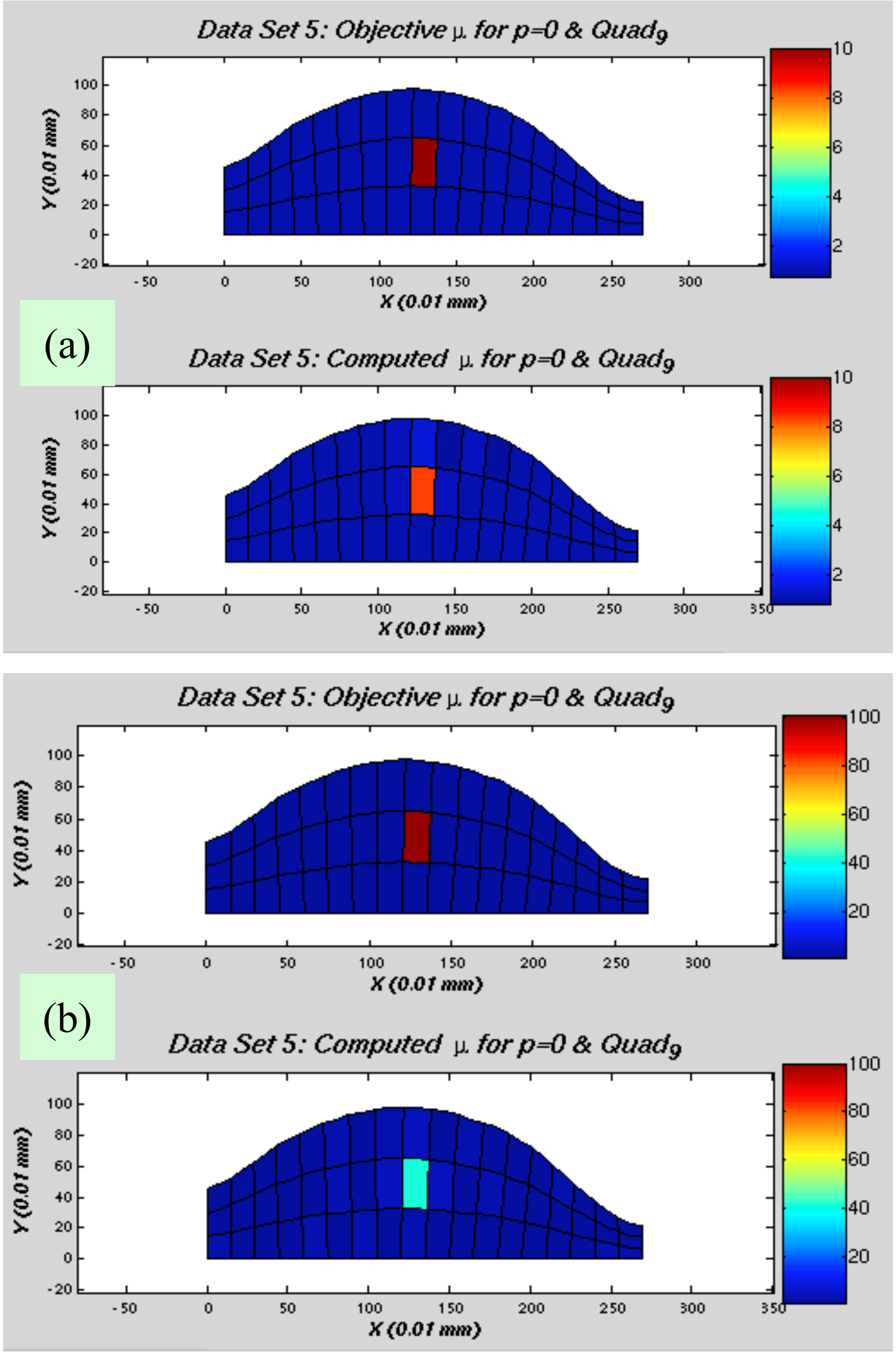

Figure 3-6: Recovery of an isolated stiff high-contrast objective (shear) modulus in the invers elasticity problem for (a) Contrast=10 (b) Contrast=100. In each case, objective moduli is shown on the top figure and the calculated moduli is depicted in the below figure. Colorbars show relative shear moduli. Axis units are in pixel and each pixel is equivalent to 0.01 mm.

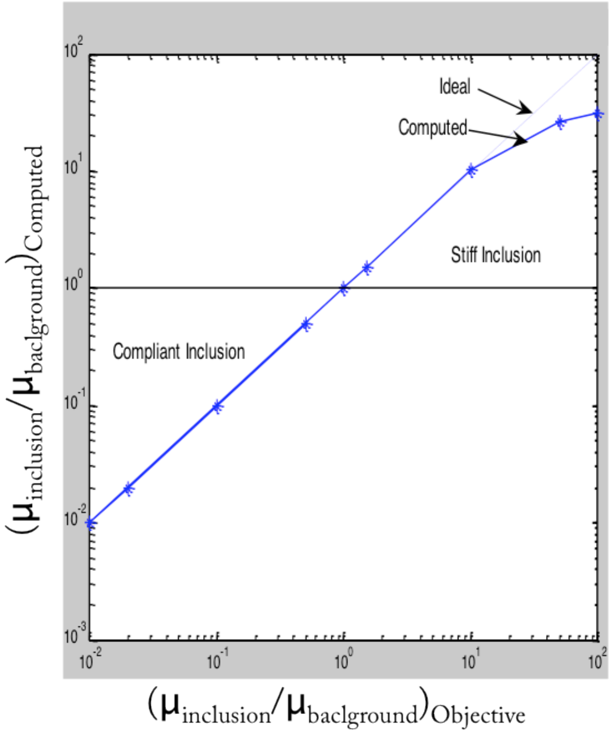

Figure 3-7: Contrast recovery curve for an isolated stiff /compliant inclusion having the same geometry as Fig. 3-6. Modulus contrast is related to the ratio of the elastic modulus between the inclusion and the background (arterial wall). Contrast recovery ratio is almost equal to 1, for compliant inclusions; and reduced to 0.4 for a stiff inclusion with a contrast equal to 100.

3.2 Registration Elasticity Problem

In the former section, we showed that given an accurate displacement measurement, inverse elasticity problem can identify complicated structural patterns of the plaques with several orders of the magnitude change in the elastic moduli. We indicated that a moderate mesh size and a linear model can reliably predict locations of increased stress/strain without significant accuracy compromise. Furthermore, we showed that the moduli of the compliant inclusions can be accurately calculated by the inverse elasticity problem, but the moduli of the stiff inclusions are conceded. Now, in this section we consider the more realistic scenario of errors being present in the displacement measurements. We identify the level of errors in the strain values. Given the errors in the pure registration problem and the pure inverse elasticity problem, we move toward simultaneous solution of the registration and inverse elasticity problem. This simultaneous solution is optimized to use the best regularization parameters based on the data fidelity calculated in the pure (disconnected) problems.

3.2.1 Registration Problem followed by Inverse Elasticity Problem for an Elastic Band

The kernel size in the image similarity measurement (Eq. 2-10) plays the most important role in determining the registration noise/resolution of the pure registration problem. Increasing the kernel size or the regularization parameters will increase the chance of convergence at the cost of decreased resolution of the elastogram. A former phantom gel study varied the kernel size by 10 pixel increments and proposed that a 41×41 kernel (41 pixels in each direction) has the best registration accuracy[98]. We used this value as the starting guide in our kernel size.

We used the robust registration algorithm suggested by Chan et al.[89], solely based on Kinematics and discussed in section 2.3, to find the displacement field between consecutive OCT images of an elastic band. We followed that by solving the inverse elasticity problem with the adjoint + BFGS method to calculate the elastic properties depicted in Fig. 3-8.

Since an elastic band is a homogenous material, the expected solution should be a constant relative modulus (e.g., all equal to 1.0). However, there is an inherent balance between enforcing the measured/registered displacement values and enforcing the uniformity of elastic modulus. For example, the solution depicted in Fig. 3-8 has a 8.0% average mismatch between computed and measured displacement of nodes, for a 4.4% standard deviation in elastic moduli of different elements.

We ask ourselves how much fidelity, and in numerical terms how big a coefficient, we can attribute to our prior information regarding each constraint and measured values. To find the proper balance between different terms, we have to quantitatively know the uncertainty/error in each term/process. Hence, in the next part we will focus on an idealized registration problem to quantify registration errors.

Alternatively, we could use REP (registration elasticity problem), based on a uniform elastic modulus, to find an idealized displacement field, and then, use it to quantify the errors in the registration problem. However, while REP is based on an idealized 2D mechanical model, a big portion of the mismatch in registration and 2D mechanical models is due to the 3D displacement (e.g., out of plane displacement which is not quantified in our experiments).

In general, errors can be attributed to factors such as OCT noise, registration error, out of plane displacements, imaging aberrations, and actual non-uniformities in the material (i.e., here elastic band). Unfortunately, these factors cannot be simply isolated. Former theoretical studies in this lab by Chan *et al.*, Khalil *et al.*, and Karimi *et al.* have partially quantified the errors introduced into the inverse elasticity problem, given that measured displacement has a given percentage error[72,89,93]. They have also used artificially built OCT images[3] to quantify errors solely due to OCT noise. However, while interested readers are encouraged to read those references, here we will present results based on actual OCT images in typical situations (which contain all sources of the errors together).

---

[3] An OCT image sequence based on PSF (point spread function) of OCT and a displacement

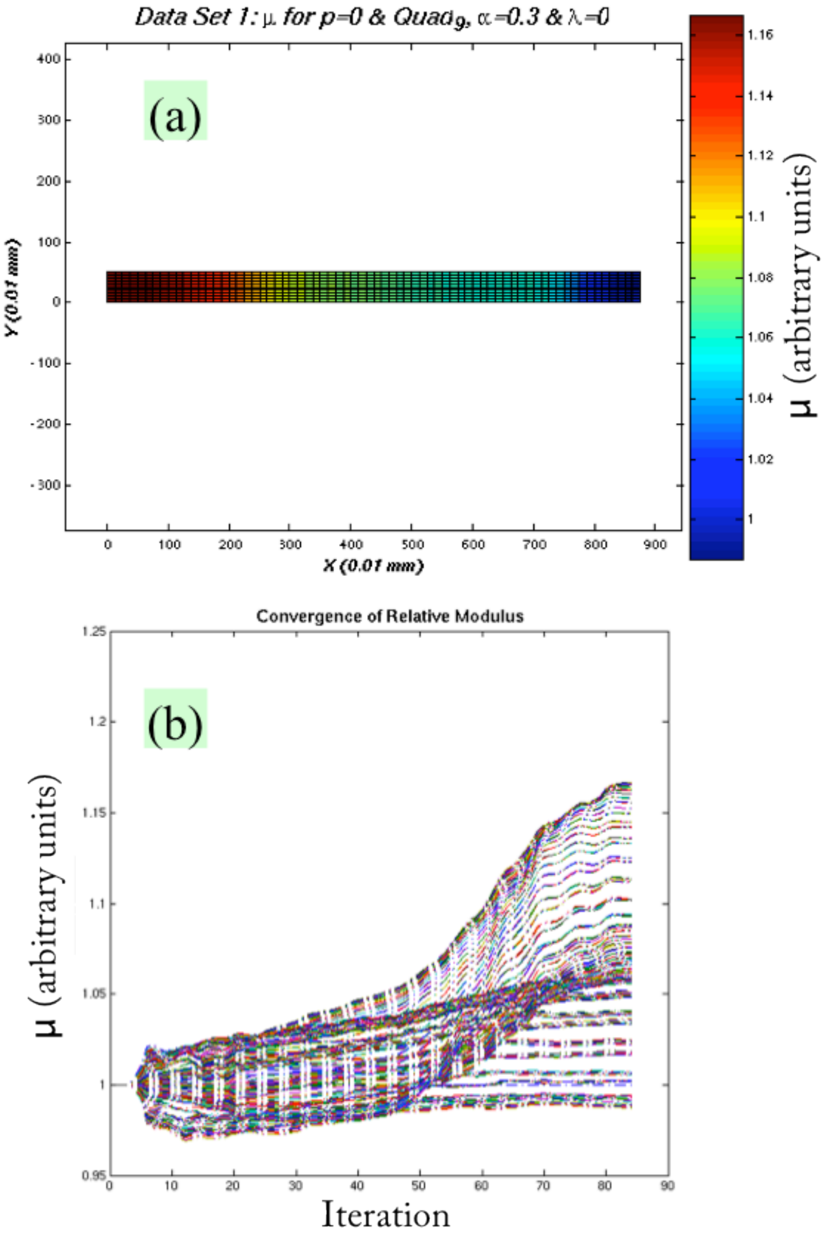

Figure 3-8: Inverse elasticity problem following registration problem of an elastic band imaged by OCT. (a): Shear modulus field, (b): Convergence of relative shear modulus of individual elements (initial guess is equal to 1.0 for all elements).

---

field provided by FEM[89].

3.2.2 Noise Reduction and Strain Limits based on Phantom Gels

We also built several polyvinyl-alcohol phantom gels and imaged them with OCT during a uniaxial stretch. Similar to the elastic band, the ideal solution is again uniform strain and modulus fields. However, our prior knowledge about uniformity can push our regularization parameters toward our desired uniform fields. To surpass this problem, we fix the regularization weights and compare the results of different experiments. In this way, we can compromise between the effects of regularization to eliminate the noise as well as the desired signals.

Since there is no alternative method to find the displacement of the samples, the accuracy and reliability of results can only be verified against uniform fields. Here, we study on an OCT image of a uniform gel, shown in Fig. 3-9, under uniaxial stretch or rigid body motion.

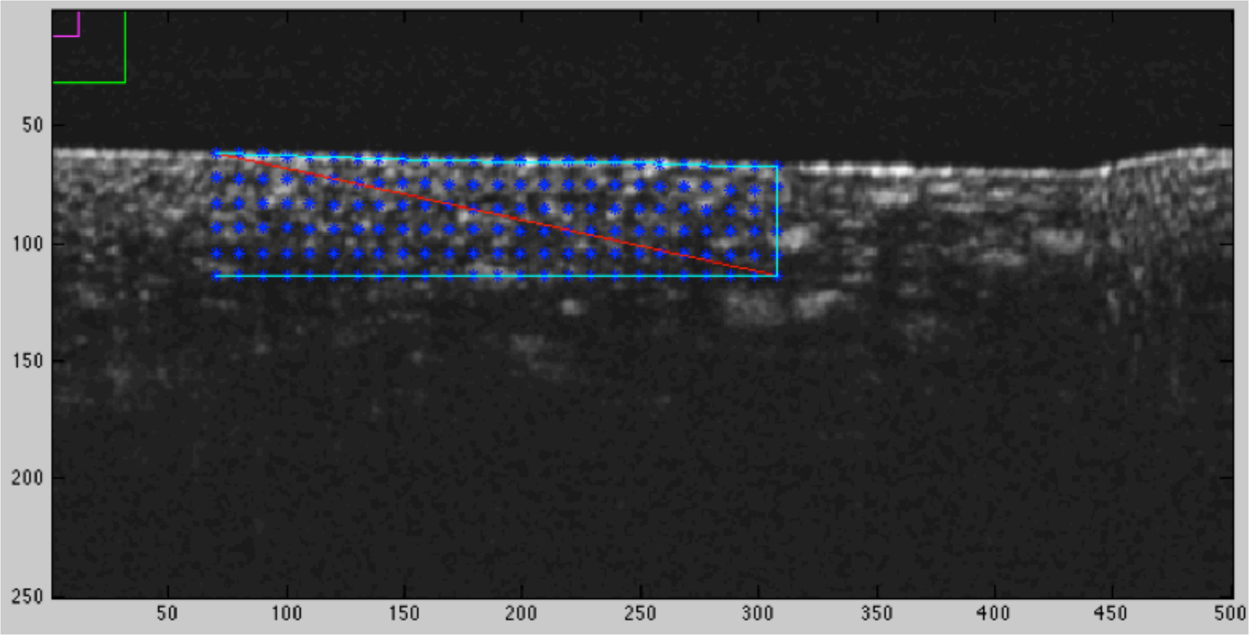

Figure 3-9: OCT gray scale cross section of a uniform gel. The cyan box depicts the region of interest. Magenta and green box correspond respectively to the actual size of the kernel and the search window around each node. Nodes are depicted with blue crosses. Axes units are in pixel and each pixel corresponds to 10 microns. Nodes are separated approximately by 10 pixels, which corresponds to about 50% overlap in their corresponding correlation kernel. Magenta box represents the SB (sub block) used in Eq. 2-10. Green box represented the search domain in which correlations are calculated with FFT before optimization starts.

First, an image sequence was generated by a 69-pixels rigid body displacement imposed by moving the scanner head. While the rigid body estimation was correct, we had a 0.5% RMS (root mean squared) error in the strain (as opposed to zero strain). Further study proved that this significant error corresponds to the image distortion in the OCT device (or probably out of plane displacement). Hence, to achieve better results and to avoid strain artifacts, we have to use the same optical region in the field of view, which means that we have to limit our studies to the smaller motions. At the same time, for the static sequences (zero motion) we had a 0.005% strain RMS (ideally should be zero); which proves that static speckle decorrelation is totally negligible. Various strain measures are listed for these two cases in the Table 3-2.

Table 3-2: Error quantification for pure registration in static case (similar frames at different times) and rigid body displacement (due to moving scanner head).

Strain Measure in % Relation between Consecutive Frame	Lateral Average	Axial Average	RMS
Static (solely due to image noise)	0.0001	-0.0005	0.005
Rigid Body Displacement (69 pixels)	0.46	-0.40	0.56

The REP or IREP could be used to improve the estimated displacement by incorporating extra constrains. However, to study the worst-case scenario, we have used the RP without any regularization for all results in 3.2.2 . In other words, we have simply done an image registration based on local block matching. Nonetheless, it must be noted that a uniform material, like gel or elastic band, has extremely few landmarks for registration, and hence within the same scenario, we might expect smaller errors in a tissue due to having a larger number of structural features.

To study the uniform strain cases, we have used a simulated 2nd frame subjected to an imposed incompressible plane strain ($\varepsilon = \varepsilon_{xx} = -\varepsilon_{yy}$, $\varepsilon_{xy} = \varepsilon_{xz} = \varepsilon_{zy} = \varepsilon_{zz} = 0$). To include some speckle noise, the 2nd frame is based on averaging two consecutive static frames. Then, this averaged frame is interpolated to the given displacement field, to generate the 2nd frame corresponding to the imposed strain.

Strains starting at 0.1% till 30% at different increments were tested as depicted in Fig. 3-10 . This range corresponds to 3 folds of variation in the average nodal normalized cross correlation. Strains more than 6% required some manipulation in initialization including: initial guesses, extended search window or a brute force search for mean displacement. However, our algorithm could not converge at all for 30% strain. This shows an upper limit in applicable strain levels probably due to breaking of the block-matching technique used for image registration.

Registration accuracy is quantified in Fig. 3-10 based on error of the average strain, as well as RMS of the strain distribution. In general, the average value had a lower error in the lateral/stretching direction, compared to the axial/depth direction. On the other hand, the RMS error of the strain was much higher in the lateral direction. Apparently, registration has an anisotropic behavior potentially due to the lower image resolution and different signal delay in the axial direction.

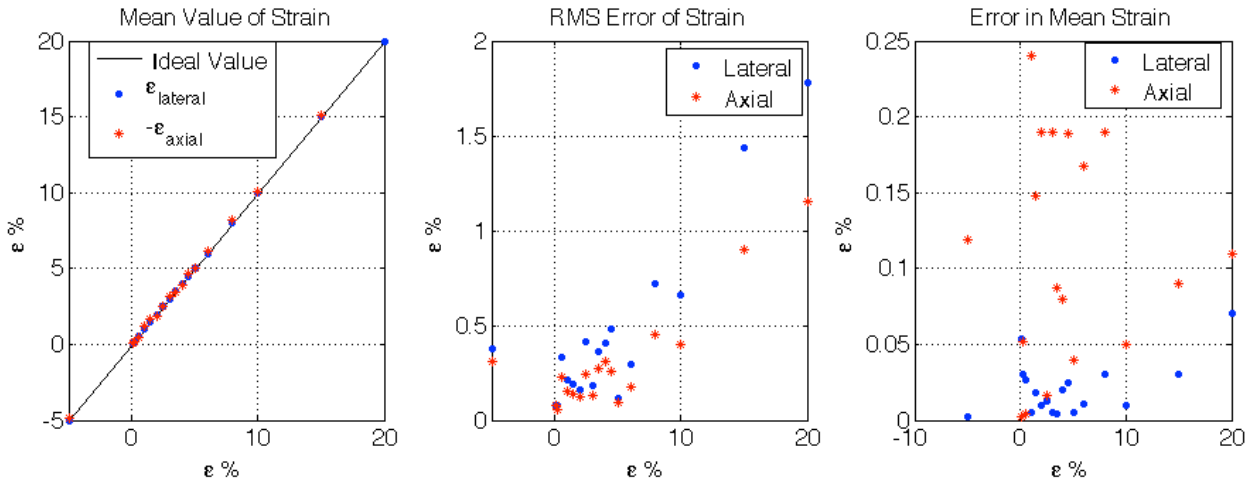

Figure 3-10: Strain estimation based on RP (Registration Problem) without any regularization applied to a simulated incompressible planar stretch of a uniform phantom gel. X-axis in all images corresponds to the applied strain. In the ideal case, the output strain (y-axis left figure) should be constant and equal to the input strain (x-axis). However, the registration generates a variable strain characterized by its average value (left figure), RMS error (root mean squared depicted in the middle figure), and the error in its average value (right figure).

Errors do not have an exactly monotonic behavior with respect to the applied strain. However, in general, the relative error of the average strain decreases with increasing levels of the applied strain. In general, it can be seen that strain RMS error and error in the average of the strain are respectively about 1/10 and 1/100 of the applied strain. This means that local variations smaller than 10% in the elastograms are not reliable/significant.

Further study of the results proves that for a relative RMS error less than 10% (of the applied strain), we should restrict ourselves to strains higher than 1%. In general, the 1-5% strains range seems to provide the best compromise for the test. Higher values of strain are susceptible to strain induced speckle decorrelation, as well as breaking apart the adopted block-matching foundation of the image registration. Lower values of the strain are not good either, because their displacement values are close to the system noise.

In summary, this study and similar studies have helped us to select the proper range of the parameters chosen for our results. This parameter set contains values such as the proper applied strain, the maximum allowable rigid body displacement, or the weights for different constraints in the optimization functional (fidelity to different prior information). We have used the same parameter set for all of our results unless otherwise noted.

3.2.3 *In Vitro* Feasibility of IREP

As a preliminary verification of *in vitro* feasibility, we injected butter into a porcine aorta's lipid pool to increase its lipid content. As depicted in Fig. 3-11, a fatty region (low elastic moduli) was identified at the center of the arterial wall, showing a higher contrast in both the elastogram and the modulus image.

These figures are generated with IREP (simultaneous registration and inverse elasticity problem), and we have used a REP-RP-IEP initialization procedure shown in Fig. 2-6. Unlike Chan *et al.* study[89], with the use of this initialization, we directly applied our technique to a fine mesh and we did not need to use a multi-resolution scheme.

It must be noted that while the lipid modulus varies in 4 orders of magnitude, our image has a greatly lower dynamic range (about 15). However, OCT image itself had a low contrast for the lipid pool (as shown in Fig. 3-11-a, lipid pool cannot be directly identified), but the modulus and elastogram images clearly show the compliant nature of the lipid pool, and hence, enhance the image contrast. Furthermore, from clinical perspective, the identification of a region of reduced elastic modulus can be more important than the measurement of an exact absolute modulus.

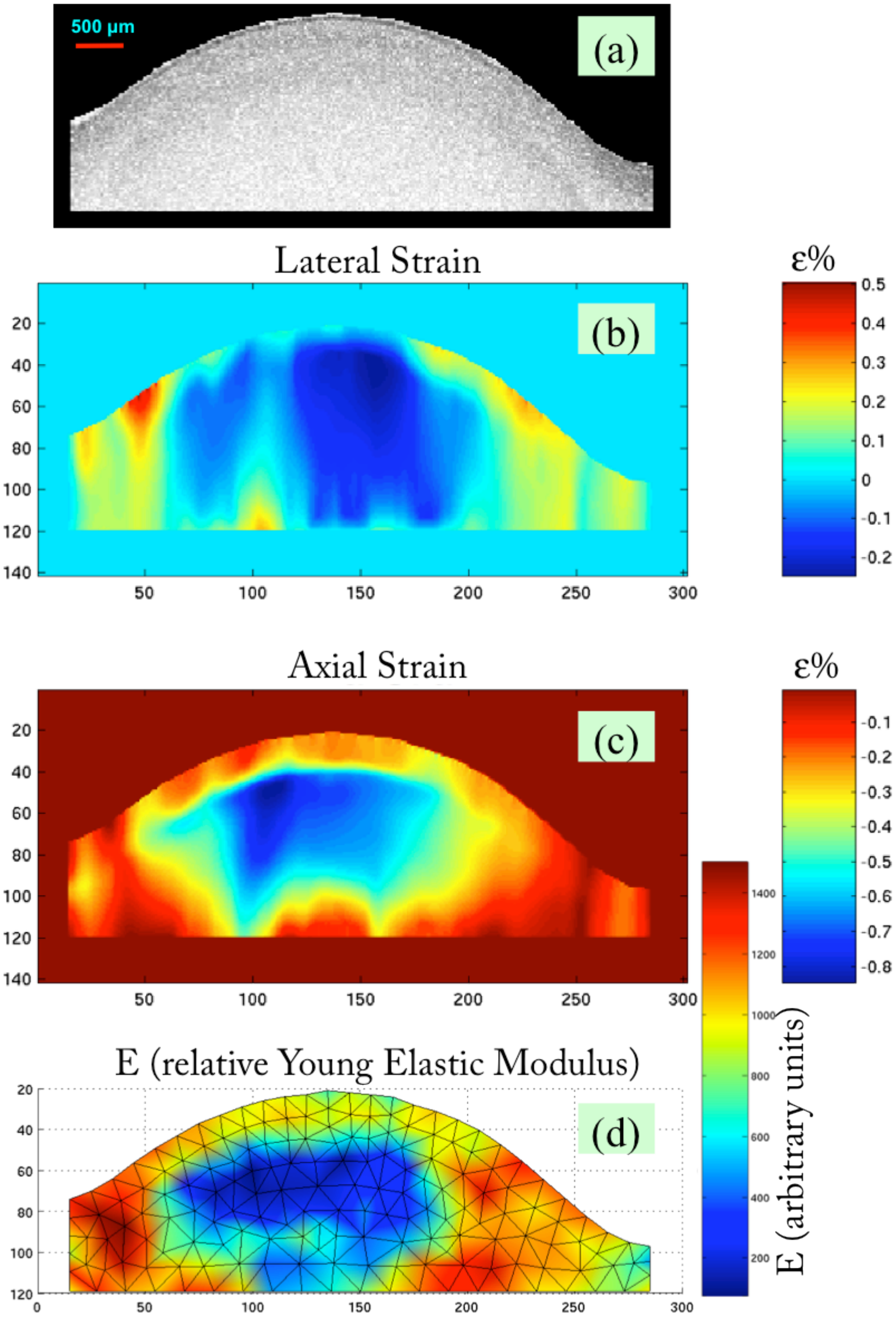
500 µm
(a)
Lateral Strain
(b)
ε%
0.5
0.4
0.3
0.2
0.1
0
-0.1
-0.2
20
40
60
80
100
120
140
50
100
150
200
250
300
Axial Strain
(c)
ε%
-0.1
-0.2
-0.3
-0.4
-0.5
-0.6
-0.7
-0.8
E (relative Young Elastic Modulus)
(d)
0
1400
1200
1000
800
600
400
200
E (arbitrary units)

Figure 3-11: *In vitro* feasibility of IREP. (a): OCT image of porcine aorta with a lipid pool in the center (temporally and spatially blurred with a Gaussian filter). (b,c): Elastogram corresponding to lateral and axial strains. (d): Relative modulus image. Images are partially taken from Karimi *et al.* [104]. X and Y axes units correspond to pixel indices.

Chapter 4: Modeling of Hydrodynamic Interactions

In the former chapters, we described and developed models for μm to mm-sized tissue elasticity analysis. In particular, we focused on how to register two images by incorporating tissue mechanics as side constraints in the registration process. The eventual output of our results was elastic modulus for a given region of the material. In this and the next chapter, we focus on hydrodynamic interaction (HI) phenomenon, and eventually analyze it in terms of the viscous constant of actin network, the primary component of the cytoskeleton, in the nm to μm size range. Taken together, this thesis covers viscoelasticity of biological tissue. Initially, we used experimental top-down approach, and finally in these chapters, we use theoretical bottom-up approach to analyze and understand mechanical properties of biological tissues and cell constituents at different scales.

4.1 Introduction

It has remained elusive how the viscous forces imposed by the fluid phase, i.e., the cytosol, can limit movement and consequently remodeling rate of the cytoskeleton. In the Stokes regime, cytosol hydrodynamic (drag) forces limit the movement of intracellular particles or relaxation time of filaments. These forces are usually calculated by using a drag coefficient based on the movement of an isolated particle. However, *in vivo* particles are not isolated and can interact with each other via the cytosol. As depicted in Fig. 4-1, a moving particle generates a flow field around itself that imposes forces on the surrounding. This phenomenon is called hydrodynamic interaction (HI) and is crucial for accurate estimation of drag coefficients and diffusion rates[105], both of which are related to relaxation times of actin filaments. HIs are responsible for organized collective motion of birds, cyclists and according to recent speculations even actin filaments in myosin motility assays[106].

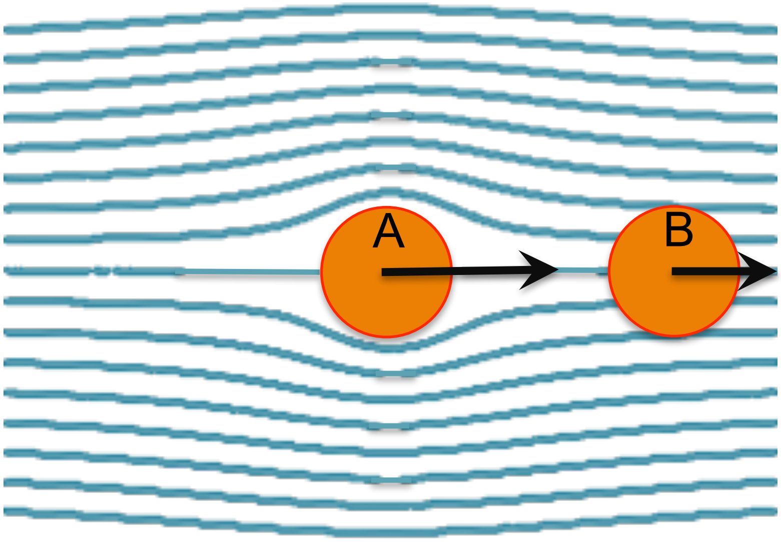

Figure 4-1: Hydrodynamic interaction concept: If particle A is in a fluid and it is moving (e.g., to the right), then it will apply a force to the particle B. This force is non-zero, unless particle B moves with the same speed as local fluid (disturbance) velocity caused by particle A.

The truncation error for an interaction decaying with r^{-n} is scaled with $\int_{\mathrm{r}_{\text{cut-off}}}^{\infty} r^{-n}\,dr$ and can be finite only for fast decaying interactions ($n > 1$). In general, the HI forces decay slowly as inversely proportional to distance (r): r^{-1}[107], and given that $\int_{\mathrm{r}_{\text{cut-off}}}^{\infty} r^{-1}\,dr$ is not finite, HI effects cannot be simplified by invoking a cut-off radius to truncate the interactions of distant elements. Consequently, HIs result in *non-sparse* matrices formed from $(3\mathrm{N})^2$ nonzero entries (N: number of particles) as opposed to *sparse* matrices for fast decaying interactions (e.g., electrostatic interaction scaled as r^{-2}). As N increases, prohibitive memory requirements and more importantly the slow convergence of the iterative procedure to solve the equations, make it almost impossible to solve the resulting linear system, explaining why HIs are usually ignored in network models.

The objective of this Chapter is to explore, describe and propose new models for HIs. Then, we can quantify HI potential role on altering the mechanics and dynamics of actin cytoskeletal networks discussed in the next chapter. Our group previously showed that an elastic Brownian dynamics rod model can replicate the dynamics of a single actin filament[108]. In a follow-up study, our group developed a 2D averaged bead model to account for HIs between multiple filaments. Despite 2D limitations, our model reproduced the experimentally observed dynamics of actin filaments and demonstrated that confinement increases persistence length[109], as observed experimentally as well[110]. Even in the absence of steric (repulsive contact) forces, HIs in the confinement alone lead to persistence length changes, suggesting that steric forces due to confinement should be distinguished from increased HIs in the confinement. Steric forces depend on inter-particle distances, but HIs are linearly dependent on the velocities and act to alter time rates of the system or vibration amplitudes. We will demonstrate that HIs have a significant role in altering actin dynamics. However, current theoretical models, including tube model, are incapable of accounting for HIs or isolating their effects at the network level[108-112]. We begin this Chapter by first presenting the standard techniques and then our new method to include HIs. We present standard bead model for spherical beads based on Rotne-Prager tensor, and then, present a new method for HI modeling of rod-shaped segments. We use these methods to analyze the role of HI in actin mechanics.

4.2 Bead Model for Hydrodynamic Interactions

Here we briefly describe the numerical scheme that we used to calculate hydrodynamic forces while taking into account nonlinear hydrodynamic interactions (HIs). All results presented here are based on this standard model, unless otherwise noted. Initially, filaments are discretized into beads with diameters equal to the diameter of the filaments, and then, we apply this model for HI.

The hydrodynamic force applied to the i$^{\text{th}}$ bead is given by $F_{h,i} = \gamma_i(U_{i-}u_i)$, where U_i is the i$^{\text{th}}$ bead velocity, u_i is the local fluid velocity (fluid velocity at the position of bead i) and γ is the friction coefficient in the Stokes regime. Quantity $u_{h,i} = F_{h,i}/\gamma_i = (U_{i-}u_i)$ is defined as the hydrodynamic velocity, which is proportional to the drag force[109]. Hydrodynamic velocity can be interpreted as the slippage velocity between particle and fluid velocity. Although in reality, there is no slip, and instead, a drag force is applied to the particle. For a spherical particle with radius a (we use $\mathrm{a} = 3.5\ \mathrm{nm}$ for actin), we can calculate friction coefficient from $\gamma = 6\pi\eta\mathrm{a}$, where η is fluid viscosity.

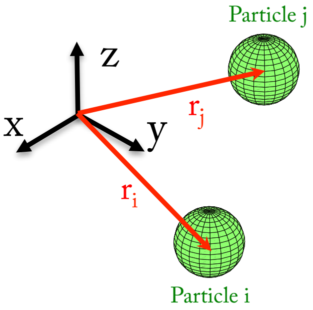

Figure 4-2: Schematic representing particle locations for $\boldsymbol{H}(\boldsymbol{r}_i - \boldsymbol{r}_j)$ (hydrodynamic interaction tensor).

Due to HI, the presence of other particles will disturb the local fluid velocity according to $u_i = u_{f,i} + \sum_{i \neq j} u_{j \to i}$, where $u_{f,i}$ is the local fluid velocity in the absence of all particles and $u_{j \to i}$ is the disturbance at the location of particle i due to particle j. Induced velocity can be obtained from $u_{j \to i} = H(r_i - r_j)F_{h,j}$ in which r is particle location and is depicted in Fig. 4-2.

H is usually calculated from $H(r) = \frac{1}{8\pi\eta|r|}\left\{\left(I + \frac{rr^T}{|r|^2}\right) + \beta\frac{a^2}{|r|^2}\left(\frac{1}{3}I - \frac{rr^T}{|r|^2}\right)\right\}$ where $\beta = 0$ would correspond to a point force (Oseen's tensor) [113,114] and $\beta = 1$ would correspond to spherical beads[109]. We use $\beta = 2$ case corresponding to the most commonly case, Rotne-Prager(-Yamakawa) tensor[115] for non-penetrating beads of the same radius ($|r| > 2a$ see Sedeh *et al.* for details [116]). Matllab is used to assemble all the linear equations and solve them to relate the bead velocities to the hydrodynamic (drag) forces. These drag forces are used for our analysis. Accuracy and proper implementation of our equations was tested against several published data, including rotating flagellum-shaped torque and trust[117], drag coefficient of different filament types (rods, S/C-shaped, and circular)[105], as well as test cases of Chandran *et al.*[109].

To model the effect of hydrodynamic interaction in a network broken down to rod segments, but without hydrodynamic interaction between those segments, we set $H(r_i - r_j)$ to zero for any two beads that do not correspond to the same segment/rod.

4.3 Rod Model for Hydrodynamic Interactions

4.3.1 Simplified Rod Model for Hydrodynamic Interactions

Our group, recently developed an averaged hydrodynamic interaction model for 2D filaments[109]. That method is based on the fact that hydrodynamic force of a rod varies almost linearly for rigid body displacement. Consequently, free ends can be treated as individual beads and beads between them are lumped together to have a linear force profile. Some sample force profiles are presented in Fig. 4-3. In this model, the lumped middle beads require several summations and approximations, which make its formulation complicated for implementation, and yet, at best they represent a shish-kebab shape instead of a cylindrical filament. Instead, this study suggests improving this former study, by replacing the lumped beads with a rod. Rod hydrodynamic properties can be taken either from experiment or currently published data. Additionally, since rod model already includes the effect of free ends, we can ignore the free-end beads. However, mixing rods and free-end beads together can make a more accurate model.

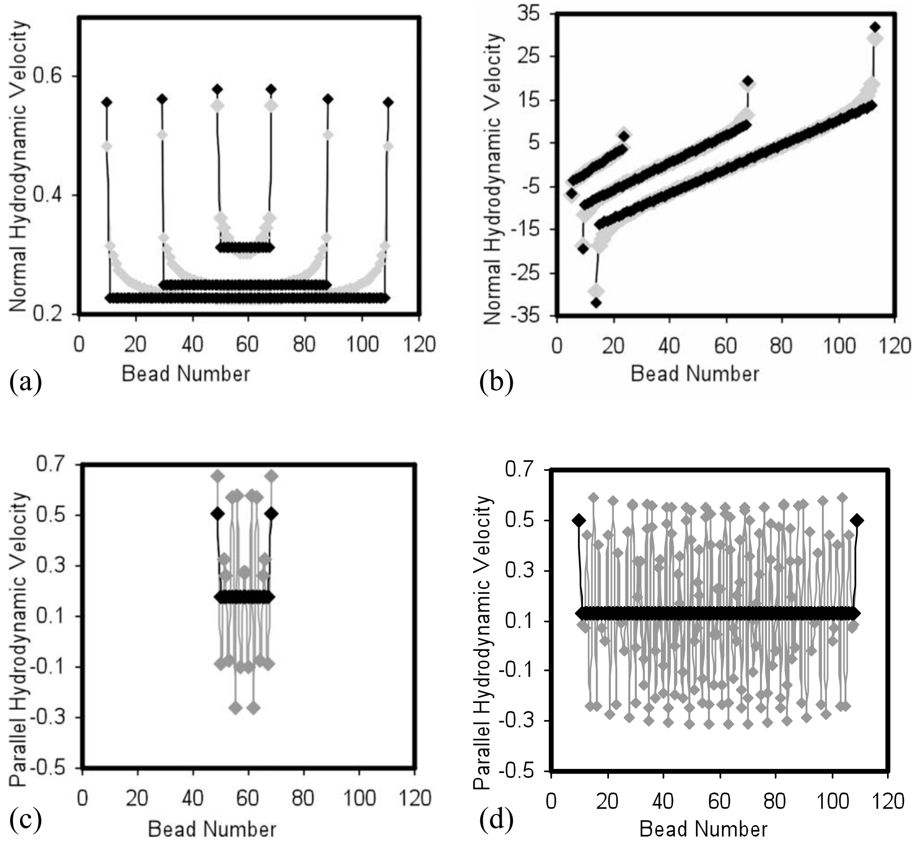

Figure 4-3: Averaged implicit hydrodynamic interaction model of Chandran *et al.* for filaments with different lengths and at different modes of rigid body movement[109]. The hydrodynamic velocity profiles are shown in gray and their approximations, based on averaged model, are shown in black. (a) Lateral movement, (b): rotation, (c-d): axial motion for two filament with different lengths. Fluctuations in c-d are due to ignoring a nonlinear term, which its effect is cancelled in the averaged model. Picture taken from[109].

Now, we have to find a way to account for hydrodynamic interactions between rods. There are already a few methods developed to approximate those interactions by doing double integrations along filament lengths approximated by Gauss quadrature[118-120]. Unfortunately despite great accuracy, those models are heavily complicated, and hence, unlikely to be adopted by most biologists. Instead, this study suggests that we can use the same beads tensor (used for hydrodynamic interaction of the beads), as rods tensor as well. Essentially, this means that rods see each other as beads and the only difference between rod and beads would be their drag coefficients. Beads have an isotropic drag coefficient, γ; whereas rods have an orthotropic drag coefficient composed of $\gamma_\perp$and $\gamma_\parallel$. This assumption about hydrodynamic interaction of the rods is a blunted assumption, but we show that the compromise in accuracy is minor in our applications (modeling actin filament). In fact, Leonardo *et al.*, independently and recently, used holographic tweezers to show that microrods interact like point particles in three dimensions at large distances, and in two dimensions for distances shorter than their length[121].

4.3.2 Rod Drag Coefficients based on Swanson-Batchelor

Drag coefficients $\gamma_\perp$and $\gamma_\parallel$ depend on the aspect ratio $\mathcal{A} = \frac{L}{a}$ (where L, a are filament length and radius accordingly). For long rods, $\mathcal{A} > 15$, we use Batchelor formula[122] and for shorter rods, $1 < \mathcal{A} < 15$, we use shape-preserving piecewise cubic interpolation of $\ln \mathcal{A}$ between discrete points of Swanson *et al.*[123] (listed in Table 4-1), and corresponding point of Batchelor for $\mathcal{A} = 15$. With this Swanson-Batchelor (SB) combination, there would not be any error in discretizing a rod into beads, if $\frac{L}{a}$ is not an even number (which can be a large error for low aspect ratios). Additionally, our rod segments can go for an aspect ratio as low as $\mathcal{A}$ =1 (i.e., a disk shape). Hence, if needed, we can discretize our rods into fine cylindrical segments, instead of usual spherical beads which are responsible for several errors in the shish kebab's model[114].

We chose Batchelor formulation due to higher accuracy especially in the low aspect ratio regime compared to the computational data of Swanson *et al.* (matched with experimental data within 0.5% error)[123]. This higher accuracy can be checked in Fig. 4-4. Furthermore, the same graphs can also be used to realize that typically different experiments and theories have a 5% difference, and hence, any attempt to provide a method with more than 5% accuracy (compared to any of those curves) is questionable.

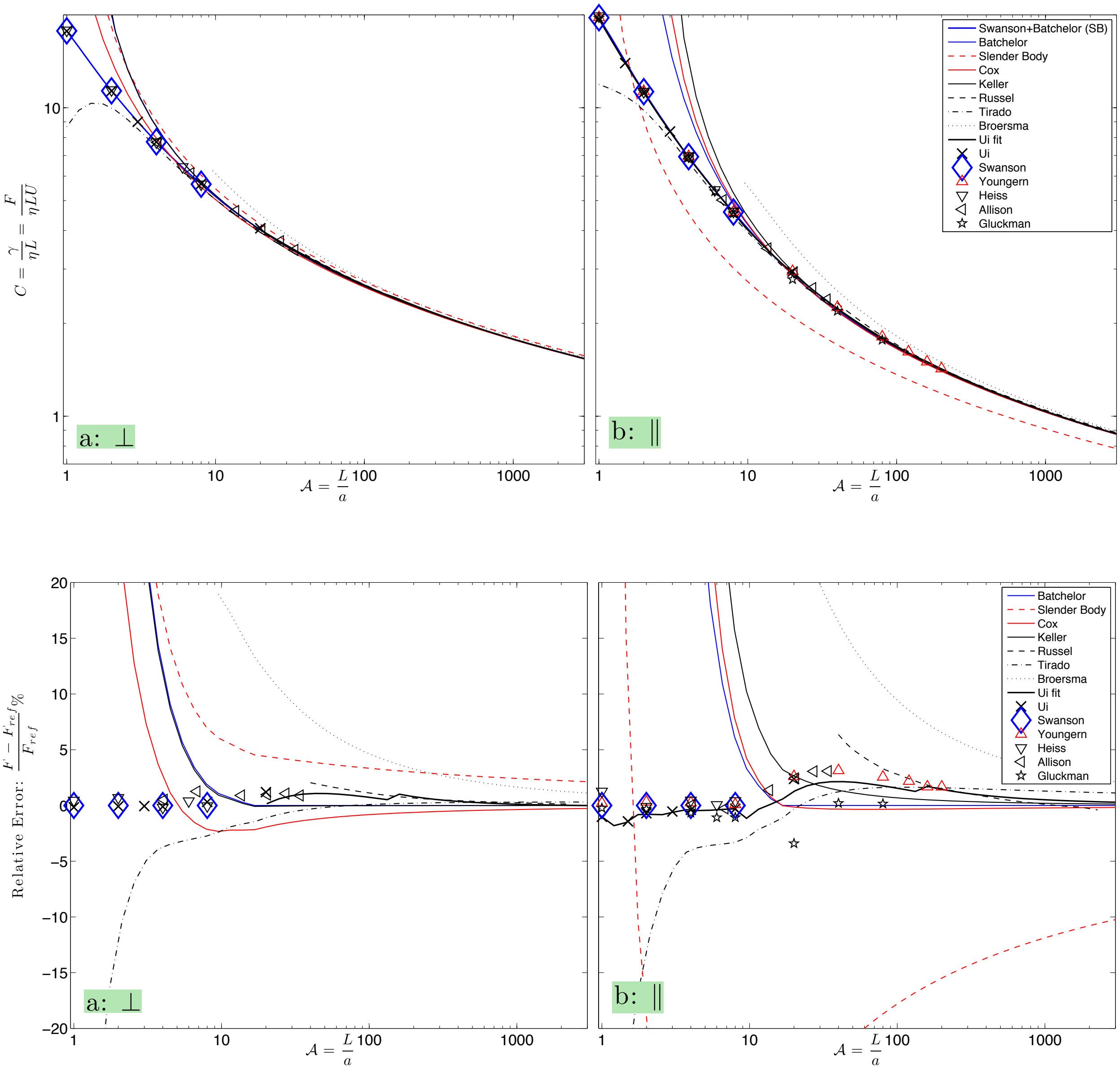

Figure 4-4: Comprehensive list of experimental data or computational models to obtain drag coefficients of rods in (a): lateral and (b): axial modes. (Top): drag coefficients, (Bottom): relative difference between above drag coefficient and a reference value based on SB (Swanson-Batchelor). The below graphs show why Batchelor is the best candidate among theoretical models, to be used for interpolation. Different lines/markers correspond to data from different sources[122-133]. Markers represent discrete data sets, and lines represent models based on a continuum function of aspect ratio. Please note that some data set are limited to only lateral or axial mode.

Rod drag coefficients are normalized by $C = \frac{\gamma}{L\eta}$. Values of C for discrete Swanson *et al.*[123] data are listed in Table 4-1 and for Batchelor regime are calculated as follows:

$$C_\perp = 4\pi\epsilon\left\{\frac{1-K_{01}\epsilon}{1+0.5\epsilon} + (K_{02} + 0.5K_{01})\epsilon^2\right\}$$

$$C_\parallel = 2\pi\epsilon\left\{\frac{1-K_{01}\epsilon}{1-0.5\epsilon} + (K_{02} - 0.5K_{01})\epsilon^2\right\}$$

$$K_{01} = \ln(2) - 1 \cong -0.307 \qquad K_{02} = 1 + {K_{01}}^2 - \frac{\pi^2}{12} \cong +0.272 \qquad \text{Eq. (4-1)}$$

$$\epsilon = \frac{1}{\ln \mathcal{A}}$$

Table 4-1: Drag coefficients for low aspect ratio rods, adopted from computational data in Table IV by Swanson *et al.*[123]. These discrete data points are combined with C values from Eq. 4-1 at $\mathcal{A} = 15$ to be interpolated of at $1 < \mathcal{A} < 15$.

$\frac{L}{a}$	1	2	4	8
$C_\perp$	17.74	11.34	7.755	5.652
$C_\parallel$	19.57	11.27	6.939	4.590

4.3.3 Volume Correction and Discretization

If a filament is discretized into beads, parts of it can be truncated, which can have an up to 20% effect on the drag coefficients (Fig. 4-5). We have listed different methods to compensate for this volume loss in Table 4-2. The effect of those methods in computing drag coefficient is plotted in Fig. 4-5. In summary, each method is good for a certain aspect-ratio range, and has a preference for either axial or lateral mode.

We have suggested a new method, called *optimal bead*, which is a special case of our rod model, in which lateral and axial drag coefficients are exactly equal. Unlike other spherical beads, this bead has a disk-like shape, and hence, can better mimic a filament by being stacked side by side. Nonetheless, since it has equal drag coefficients in all directions, at long distances, it is like a spherical bead. Hence, we can use well-developed spherical bead hydrodynamic interaction tensors already available. Consequently, we can use standard hydrodynamic interaction routines, and only change discretization schemes slightly to accommodate for the optimal bead.

We also tested force distribution for a straight filament moving laterally or axially, and we found that other than at the free-ends, these different techniques have subtle effect on force distribution.

Table 4-2: Different methods to discretize a filament into stacked beads starting from shish kebab's model, followed by different ways to compensate for volume and finally our proposed model. Schematic shows a filament composed of 3 beads, but effective bead diameters and overlaps are not to actual scale. Filament radius, effective radius, hydrodynamic radius and bead spacing are represented by a, a_e, R_H and s respectively.

Method	Bead Discretization	Volume Correction Eq.	Description
w/o Volume Correction	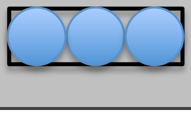	N.A.	$R_H = \mathrm{a},\ s = 2\mathrm{a}$ Filament is discretized into spherical beads stacked side by side.
1	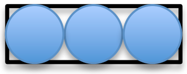	$\frac{4}{3}\pi a_e^3 = \pi a^2 \times 2a$	Use results of the first row, but multiply the hydrodynamic forces by $\frac{a_e}{a} = \sqrt[3]{\frac{3}{2}} \cong 1.1447$
2	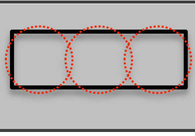	$\frac{4}{3}\pi a_e^3 = \pi a^2 \times 2a$	Use the discretization of the first row, but proceed to the hydrodynamic interactions with $R_H = a_e \cong 1.1447a$
3	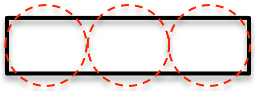	$\frac{4}{3}\pi a_e^3 = \pi a^2 \times 2a_e$	Use results of the first row for the same number of beads, but multiply aspect ratio by $\frac{a_e}{a} = \sqrt{\frac{3}{2}} \cong$ 1.2247
4	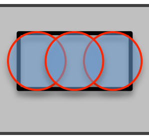	$\frac{4}{3}\pi a^3 = \pi a^2 \times s$	Similar to the first row, but beads are stacked with overlap ($s = \frac{4}{3}a$ instead of $s = 2a$)
Optimal Bead	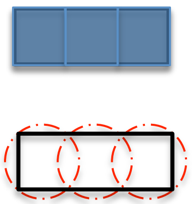	$\mathrm{C}_{\parallel} = \mathrm{C}_{\perp}$	$R_H \cong 1.1842a, \mathrm{s} \cong 1.9237a$ ($\mathrm{C}_{\parallel} = \mathrm{C}_{\perp} \cong 11.604$ for $\mathcal{A} \cong 1.9237$) Filament is discretized into disk-shaped beads stacked side by side. For each disk, transverse and axial drag coefficients are equal and hence a spherical bead can approximate those disks.

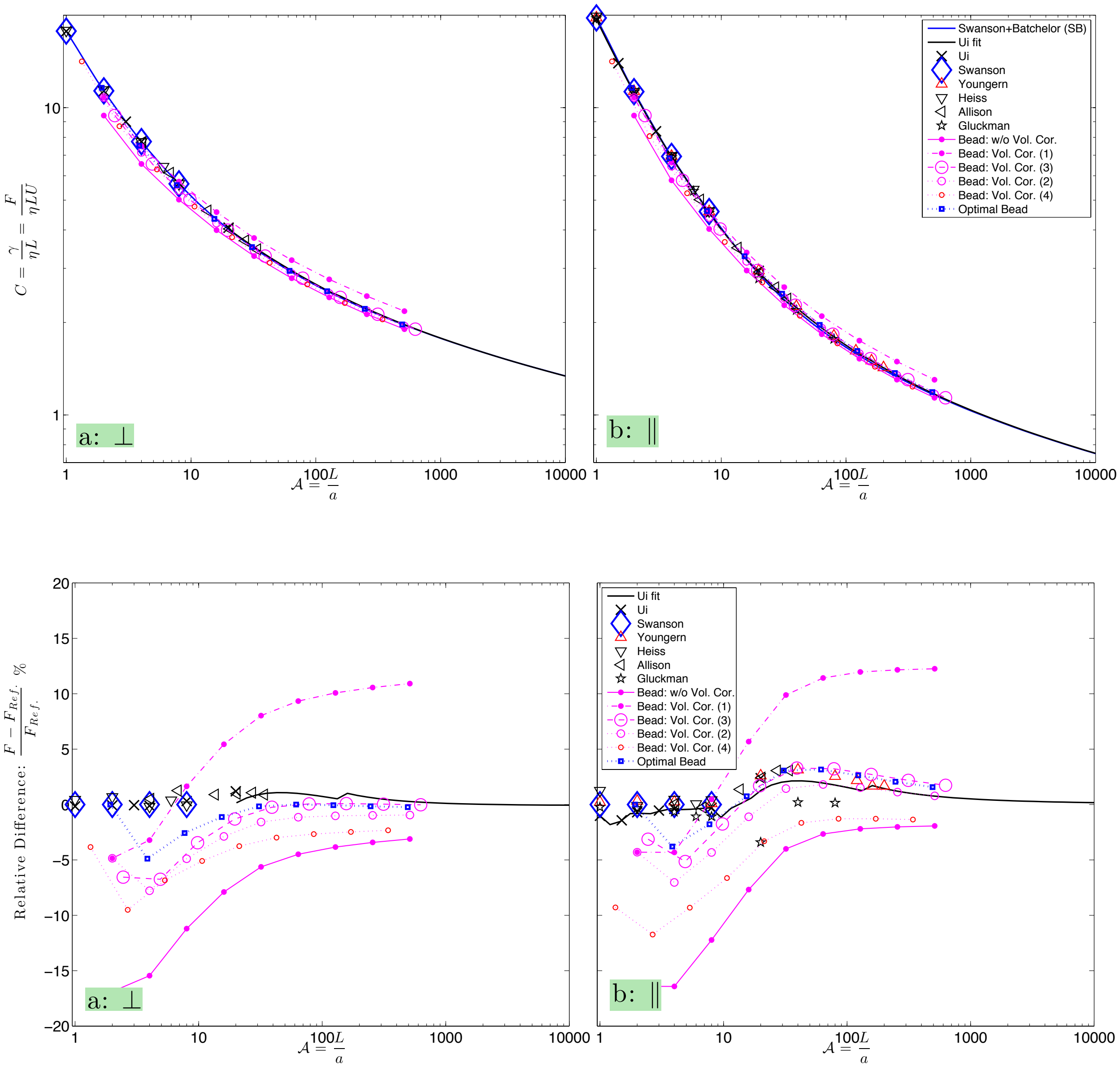

Figure 4-5: Drag coefficients of rods discretized into beads having different volume corrections compared against theories or experimental data in (a): lateral, and (b): axial modes for Rotne-Prager tensor. (Top): drag coefficients, (Bottom): relative difference between above drag coefficient and a reference value based on SB (Swanson-Batchelor). The below graphs show why optimal bead can be the best candidate for volume correction and discretization. Different lines/markers correspond to data from different sources[122,123,129-133]. Markers represent discrete data sets, and lines represent models based on a continuum function of aspect ratio. Please note that some data set are limited to only lateral or axial mode.

4.3.4 Rod Model: All components together

At this point, we can establish that Swanson-Batchelor can be used as a reliable reference benchmark to test our different hydrodynamic interaction models for the rods. According to Fig. 4-4, as long as a rod model can produce the same drag coefficients as Swanson-Batchelor (within 5%), it can be assumed to pass the minimum verification requirements. To finalize our rod model, we have to set the following two variables and we opted to test the following candidates:

1. Candidate for Hydrodynamic interaction tensor:
   a. Oseen: the simplest
   b. Spherical bead
   c. Rotne-Prager: similar to spherical bead, but can have a different form if the beads penetrate each other.

2. Candidate for Stokes radius appearing in the above tensor:
   a. Segment radius
   b. Segment length
   c. Segment equivalent Stokes radius in 2D
   d. Segment equivalent hydrodynamic radius in 3D
   e. Segment Aspect ratio
   f. Segment equivalent volumetric spherical radius: the radius for the sphere within the same volume
   g. Ignore hydrodynamic interaction!

As for the selection of the tensor, we wanted a tensor that works well with the optimal bead, as the ideal and the simplest case of the rod model. It turns out that in general, Oseen tensor and Rotne-Prager tensor behave similarly, especially at long distances, and work better than spherical bead tensor. However, both Oseen tensor and spherical bead tensor are susceptible to generate unstable solution, as can be seen in Fig. 4-6 for the axial mode. In fact, since for a straight rod individual beads moving in the axial direction have a doubled interaction, axial direction is more likely to become unstable. Indeed, that is why Rotne-Prager tensor was developed to improve the solution stability and decrease numerical fluctuations. Hence, we conclude that we will pick up the standard Rotne-Prager tensor for our rod model. That is great, because almost every custom-built hydrodynamic interaction code is based on Rotne-Prager tensor, and hence, our model can be better integrated to available codes.

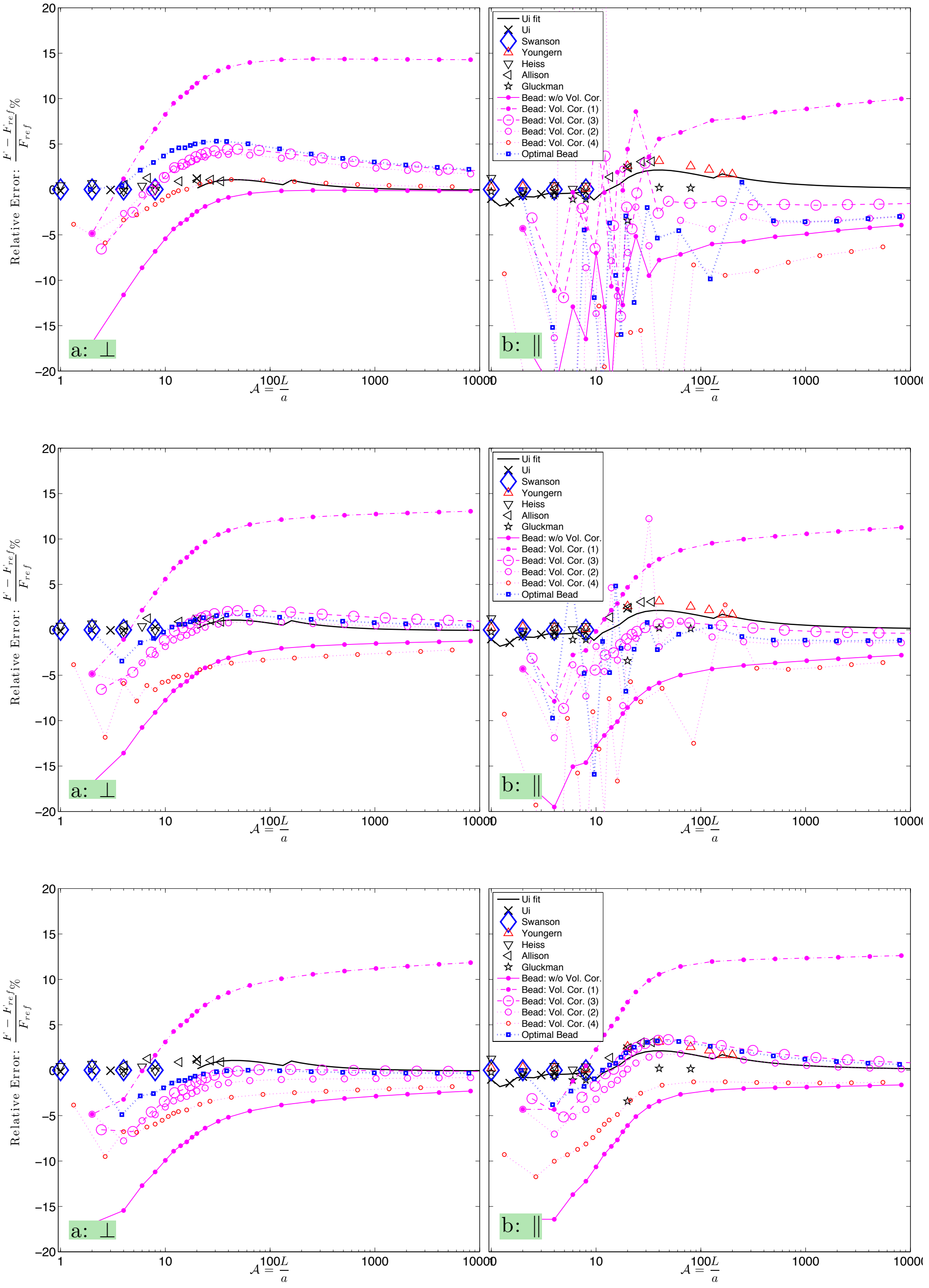

Figure 4-6: Relative error in the drag coefficients of rods discretized into beads having different volume corrections compared against theories or experimental data in (a): lateral, and (b): axial modes for (Top): Oseen tensor, (Middle): spherical bead tensor, (Bottom): Rotne-Prager tensor (the stable case). The graphs show relative difference between drag coefficient and a reference value based on SB (Swanson-Batchelor).

We also tested our rod model with different candidates for Stokes radius. We discretized rods with different aspect ratios, into different number of segments. Then we calculated the drag coefficient of the total rod and evaluated its error against the Swanson-Batchelor reference data. To our surprise, almost all a, c, d, and f candidates behave similarly with less than 5% error! Candidate b, and e are OK but only for lateral mode; however, candidate g generates huge errors as expected. All this data are shown in the Fig. 4-7.

In summary, at this point for our rods, hydrodynamic interactions are so big that it cannot be neglected (candidate g fails). However, segments geometry is such that the specific choice of Stokes radius among a, c, d or f does not make a big difference. This subtle difference is also due to the fact that each of these candidates perform well for either lateral or axial, and in a specific range of the aspect ratio. Hence, when they are compared together in general they most look alike. Nonetheless, we might pick up a specific Stokes radius based on our application.

We could also think of the alternative scenario, where these subtle similar errors are mostly due to the assumed form of the hydrodynamic interaction tensor, instead of its Stokes radius. This is likely; because we have approximated the polarized flow patterns around a rod, with a isotropic flow pattern around a sphere. Nonetheless, it is still surprising that this simple model can bring the error down to about 5%, where 5% is in fact, the uncertainty in the Swanson-Batchelor model.

We also tried candidate-a (segment radius) in a problem for two F-actins being aligned from either parallel configuration or crossed. Our results indicate that while hydrodynamic interactions could change the alignment dynamics. However, at least for this problem, candidate-a resulted in a solution similar to bead-discretized model (which means it is confirmed against standard method). Nonetheless, more complex 3D models might discriminate between our different candidates for Stokes radius. In fact, as will be noted in the network section of the next chapter, for a 3D system nearby filaments will substantially increase the role of hydrodynamic interaction, as opposed to small hydrodynamic interactions for the distant parts of the same filament. Consequently, further studies are required if this model is applied to crowded 3D or 2D networks.

Figure 4-7: Relative error in the drag coefficients of rods discretized into rod segment with different number of segments in (a): lateral, and (b): axial modes for 7 different candidates, a to g, of the Stokes radius for our Rod model. The graphs show relative difference between drag coefficient and a reference value based on SB (Swanson-Batchelor).

a. Segment radius

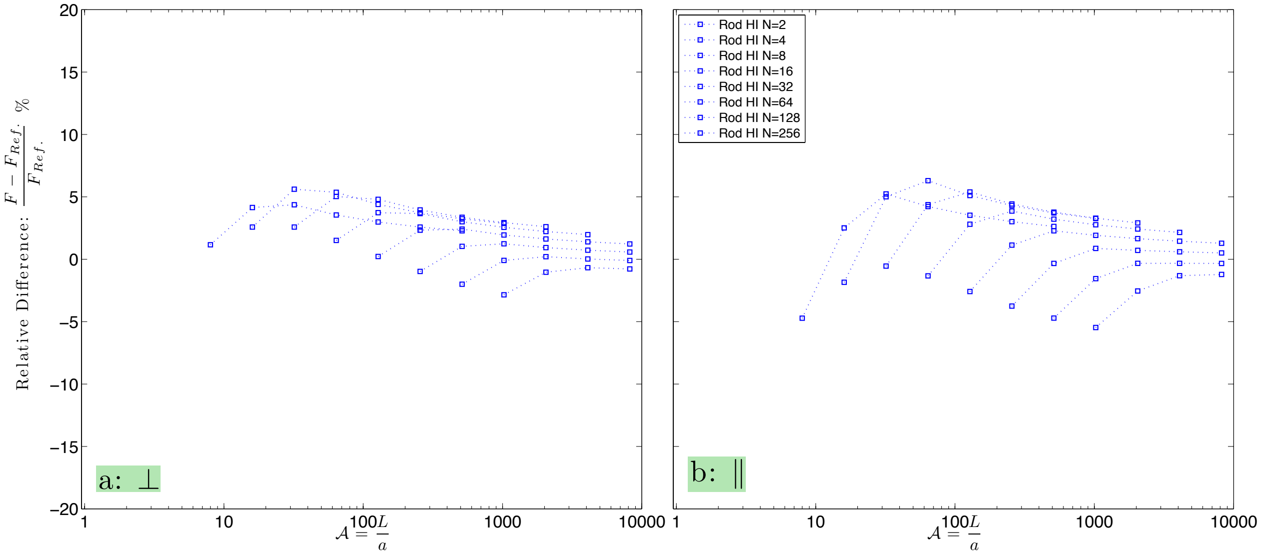

b. Segment length

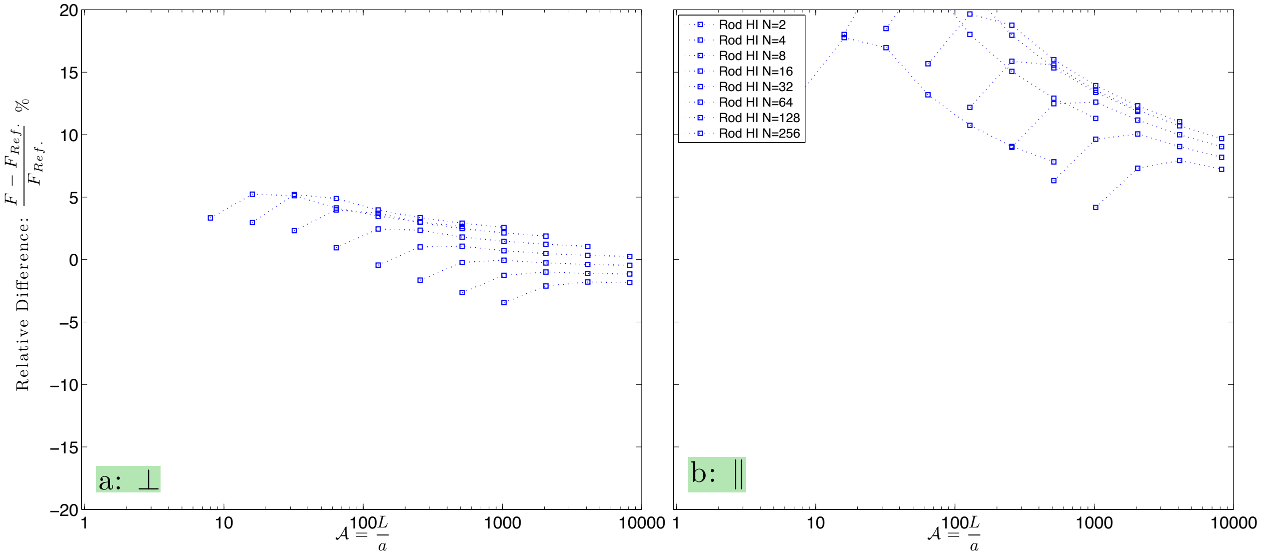

c. Segment equivalent Stokes radius in 2D

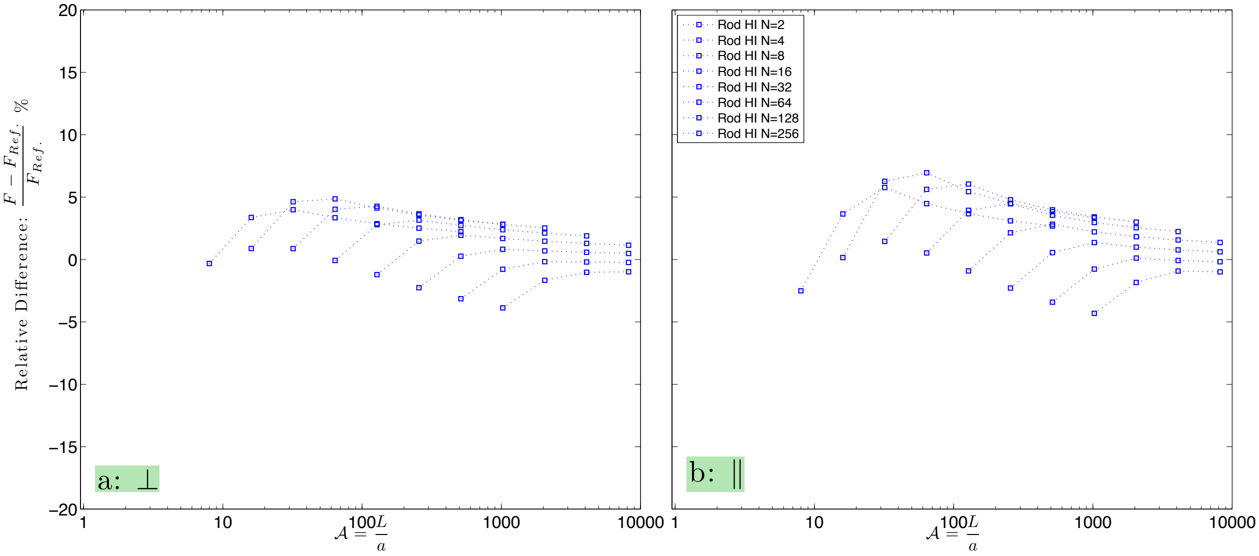

d. Segment equivalent hydrodynamic radius in 3D

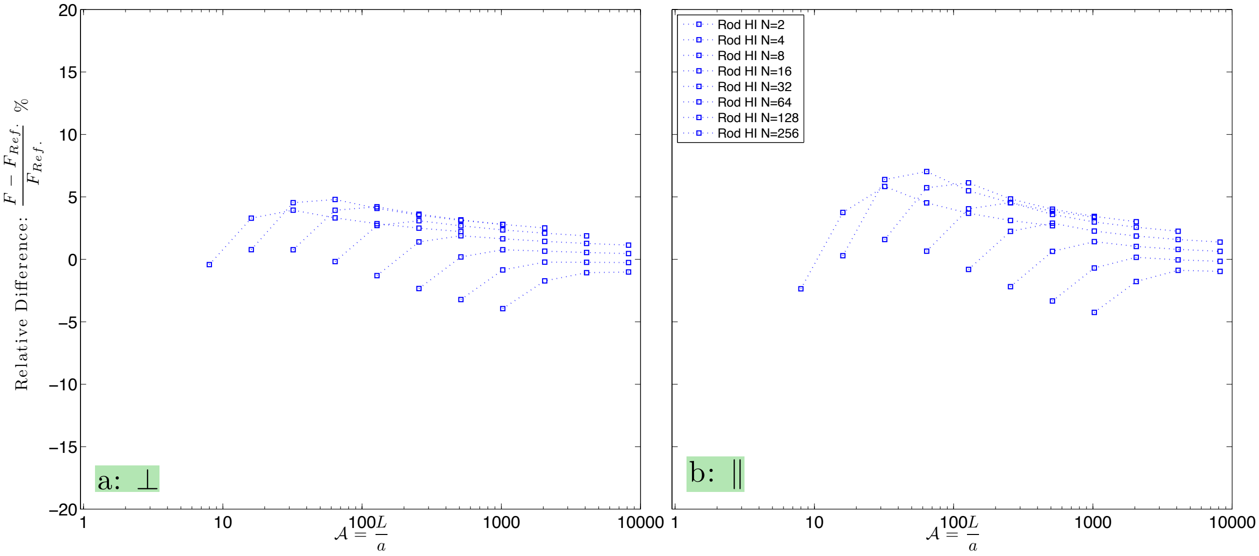

e. Segment aspect ratio

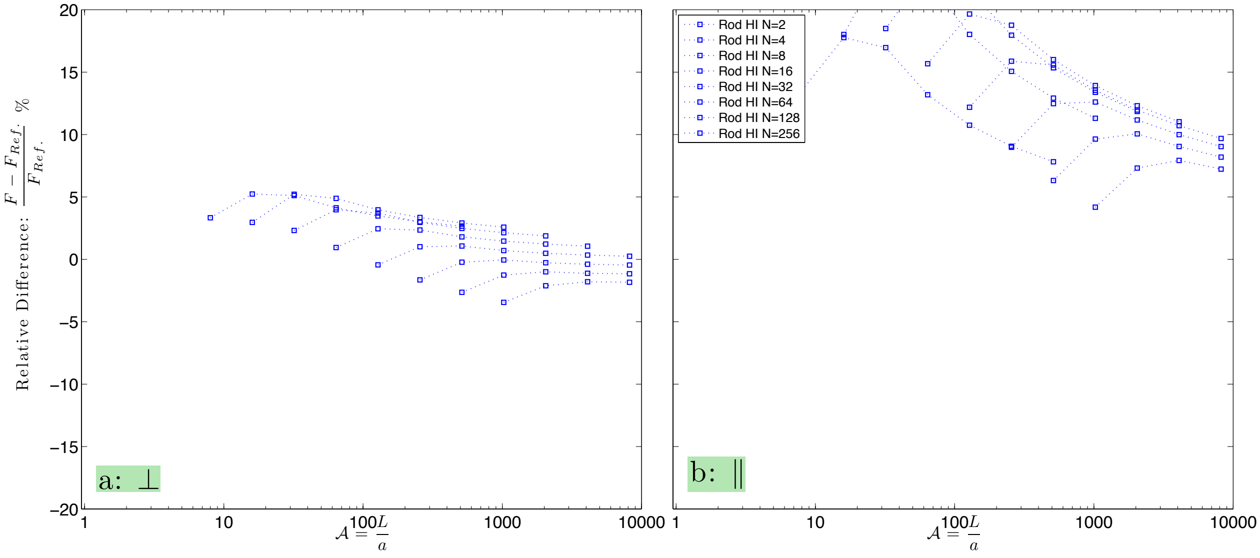

f. Segment equivalent volumetric spherical radius

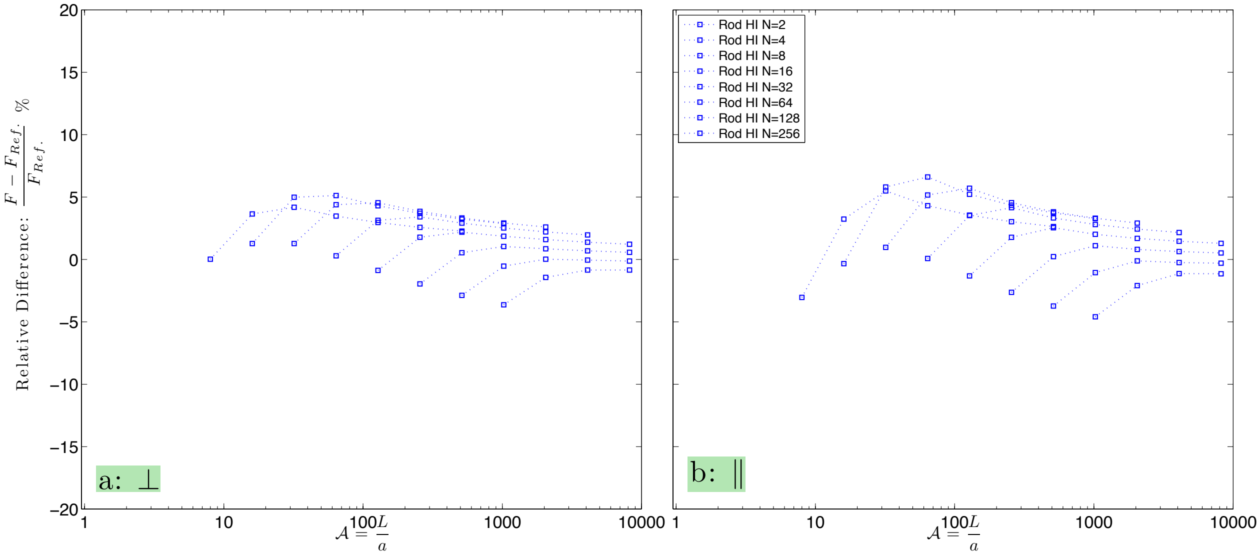

g. **Ignore hydrodynamic interaction:** errors are generally much bigger than 20%

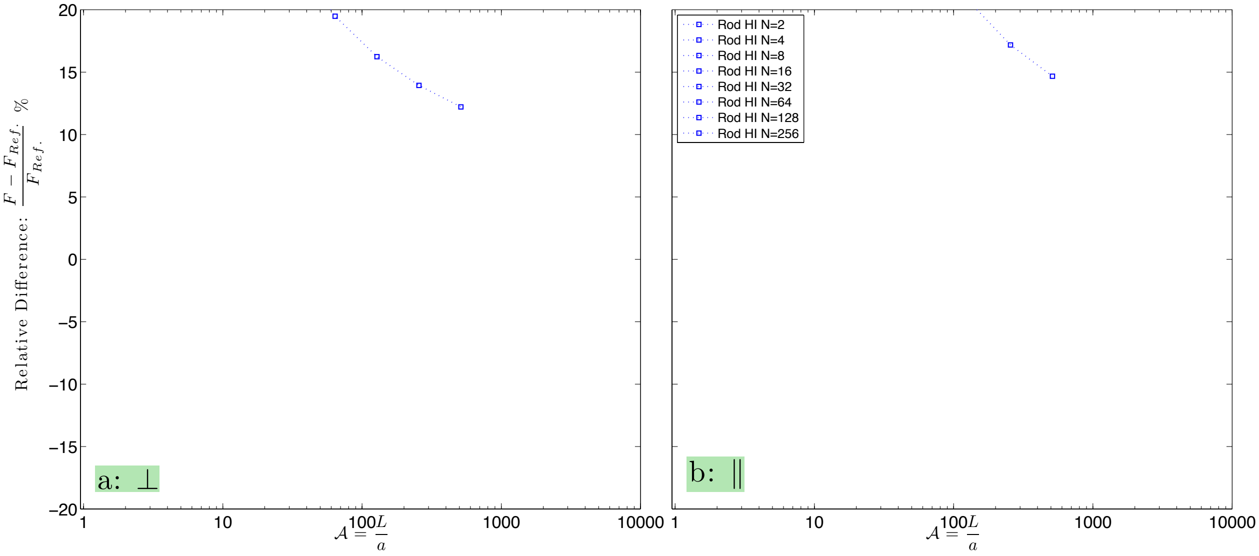

Chapter 5: Role of Hydrodynamic Interactions in F-actin Mechanics

5.1 Introduction

Cytoskeletal network is a dynamic structure in cells responsible for cellular shape, integrity, remodeling, and migration[134]. Actin is the primary structural component of the cytoskeleton, constituting up to 10% of the cell mass. Actin responds rapidly and dramatically to external forces, and is also instrumental in the formation of leading edge protrusions during cell migration[135]. Actin protein is found in all eukaryotic cells (except the nematode sperm) and its genome has been highly conserved.

As demonstrated in Fig. 5-1 and Fig. 5-2, actin builds different structures ranging from isotropically crosslinked networks to highly polarized bundles named stress fibers[136,137]. As depicted in Fig. 5-1-a, F-actin forms by the polymerization of globular, monomeric actin (G-actin) into a twisted strand of filamentous actin (F-Actin) 7–9 nm in diameter. Monomers have a molecular weight of 43 kDa and consist of 375 amino acids. F-actin is a polarized molecule having two different ends, namely a barbed end and a pointed end. ATP can bind to the barbed end, which allows for monomer addition and filament growth, whereas depolymerization occurs preferentially at the pointed ends. Hence, a tread milling process can occur which will polarize the cell, and will help in cell motility. Actin's persistence length is about $15 - 17\ \mu m$ and its Young's Modulus is about 3 GPa[135].

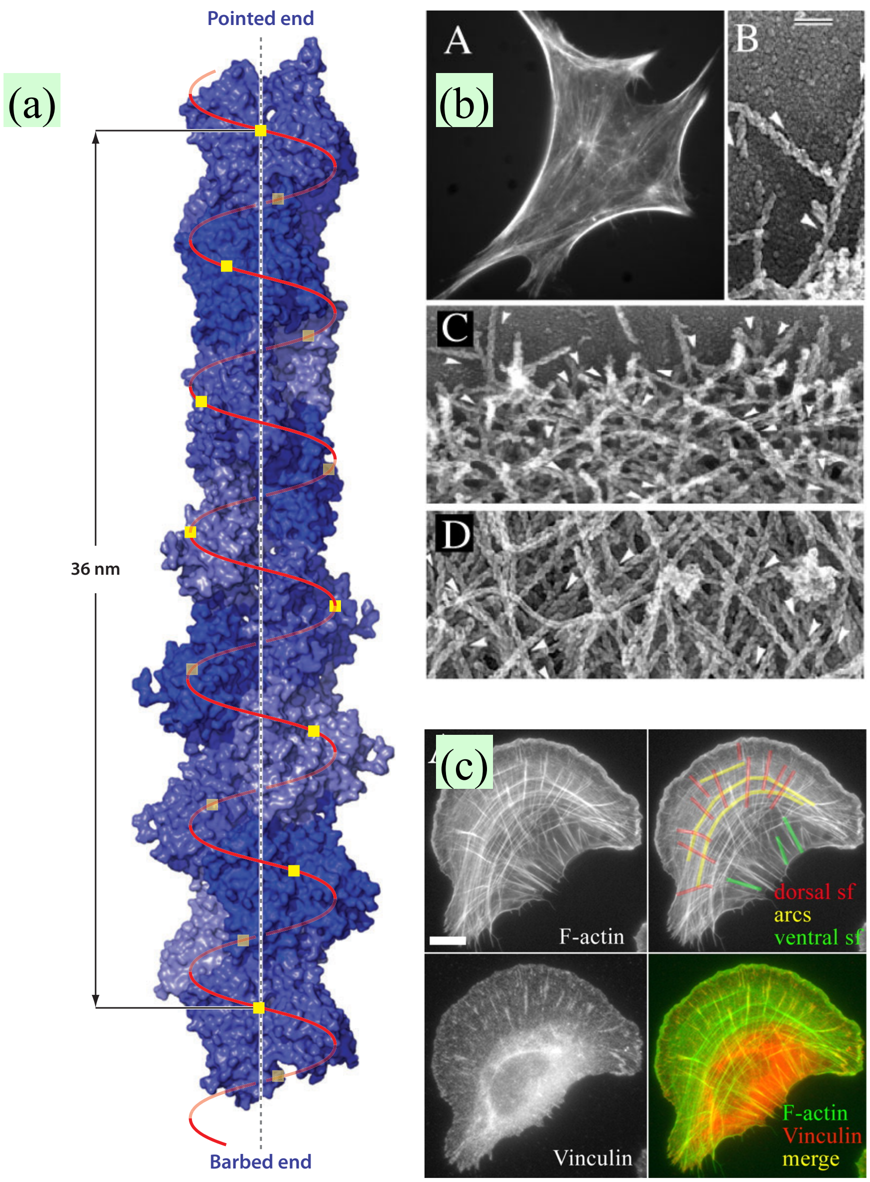

Figure 5-1: Actin molecular and macro structure. (a): F-actin (filamentous actin) is formed from two helices composed of G-Actins (Globular actin: having a known protein sequence). F-Actin is a polarized molecule having different ends. Picture is taken from Dominguez *et al.*[138]. (b) Actin organization in 3T3 cells: A) fluorescence-staining of F-actin, B-D) electron microscopic image of actin. B) Actin junction. C) Homogenous structure at the leading edge, D) polarized/ Heterogeneous structure elsewhere. Picture is taken from Svitkina *et al.*[139]. (c) Similar to (b)-A, F-actin forms different structure inside the cell and has different concentration at various locations. Some F-actins form bundles, called stress fibers, which are the key component of the cell motility (especially with the aid of focal adhesion proteins such as Vinculin, which is stained here). Focal adhesions and F-actin are visualized with anti-vinculin antibodies and phalloidin, respectively in U2OS cells. Three categories of contractile actin arrays are highlighted on the F-actin image: dorsal stress fibers (red), transverse arcs (yellow) and ventral stress fibers (green). Scale-bar: 10 micrometer. Picture is taken from Hotulainen *et al.*[140].

Actin polymorphic structure can respond to instantaneous loads and absorb extracellular shock, while for lower loading rates it can gradually release the excess stress by remodeling and relaxing. Actin's persistence length, $15-17\ \mu m$, is close to the cell size. This means that the contour length of actin filaments is typically of the same size as its persistence length, hence a semiflexible filament[135]. In contrast to flexible or rigid filaments, the dynamics of semiflexible filaments are not yet fully understood and actin has been used as a model polymer to study semiflexible filaments. Actin filament length, crosslinker density and strength can all be tuned to investigate a wide range of behavior in crosslinked/entangled networks of semiflexible filaments[110,141-143]. Superbly different forms of crosslinked actin networks are depicted in Fig. 5-2, all generated by varying crosslinker/actin relative concentration and crosslinker type.

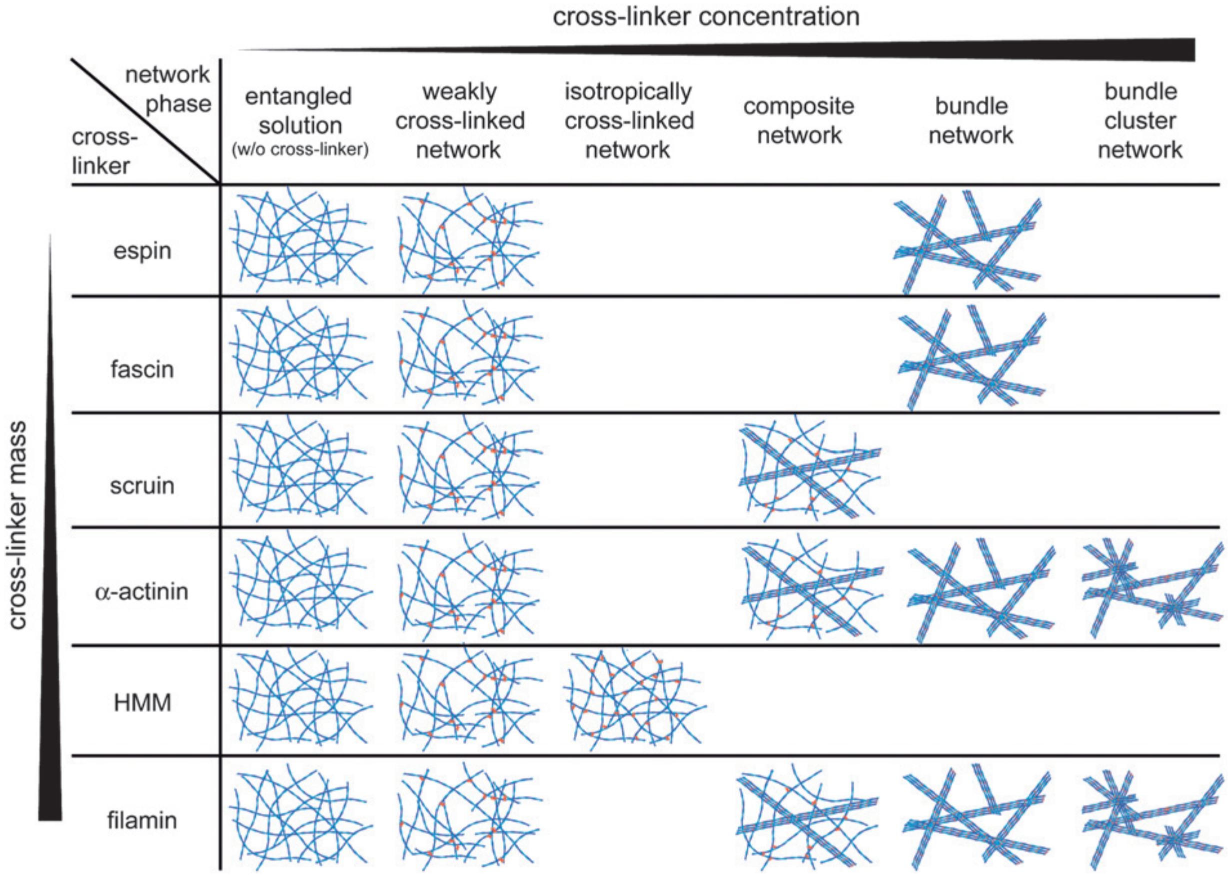
cross-linker concentration
network phase
cross-linker
entangled solution (w/o cross-linker)
weakly cross-linked network
isotropically cross-linked network
composite network
bundle network
bundle cluster network
espin
fascin
scruin
α-actinin
HMM
filamin
cross-linker mass

Figure 5-2: F-actin crosslinked network at different concentration/types of crosslinkers taken from Lieleg *et al.*[137]. We are particularly interested in HMM (Heavy Myosin Motor) case, which forms isotropically crosslinked active networks.

It has remained elusive how the viscous forces imposed by the fluid phase, i.e., the cytosol, can limit movement and consequently remodeling rate of the cytoskeleton. In the Stokes regime, cytosol hydrodynamic (drag) forces limit the movement of intracellular particles or relaxation time of filaments. These forces are usually calculated by using a drag coefficient based on the movement of an isolated particle. However, *in vivo* particles are not isolated and can interact with each other via the cytosol. As depicted in Fig. 4-1, a moving particle generates a flow field around itself that imposes forces on the surrounding. This phenomenon is called hydrodynamic interaction (HI) and is crucial for accurate estimation of drag coefficients and diffusion rates[105], both of which are related to relaxation times of actin filaments. HIs are responsible for organized collective motion of birds, cyclists and according to recent speculations even actin filaments in myosin motility assays[106].

The objective of this chapter is to explore how HIs may alter the mechanics and dynamics of actin cytoskeletal networks. Our group previously showed that an elastic Brownian dynamics rod model can replicate the dynamics of a single actin filament[108]. In a follow-up study, our group developed a 2D averaged bead model to account for HIs between multiple filaments. Despite 2D limitations, our model reproduced the experimentally observed dynamics of actin filaments and demonstrated that confinement increases persistence length[109], as observed experimentally as well[110]. Even in the absence of steric (repulsive contact) forces, HIs in the confinement alone lead to the persistence length change, suggesting that steric forces due to confinement should be distinguished from increased HIs in the confinement. Steric forces depend on inter-particle distances, but HIs are linearly dependent on the velocities and act to alter time rates of the system or vibration amplitudes. Here we demonstrate that HIs have a significant role in altering actin dynamics. However, current theoretical models, including tube model, are incapable of accounting for HIs or isolating their effects at the network level[108-112].

5.2 Hydrodynamic Interactions in Single Filament

To explore the effect of HIs on an actin network, we begin at a single filament level examining its bulk movements and vibrational modes. Next, we examine two filaments being aligned during bundle formation. Finally, we investigate the role of HIs in network level for regular 1D and 3D random networks. We examine the HIs between different filaments as well as HIs between different positions of the same filament.

5.2.1 Rigid Body Movement and Diffusion

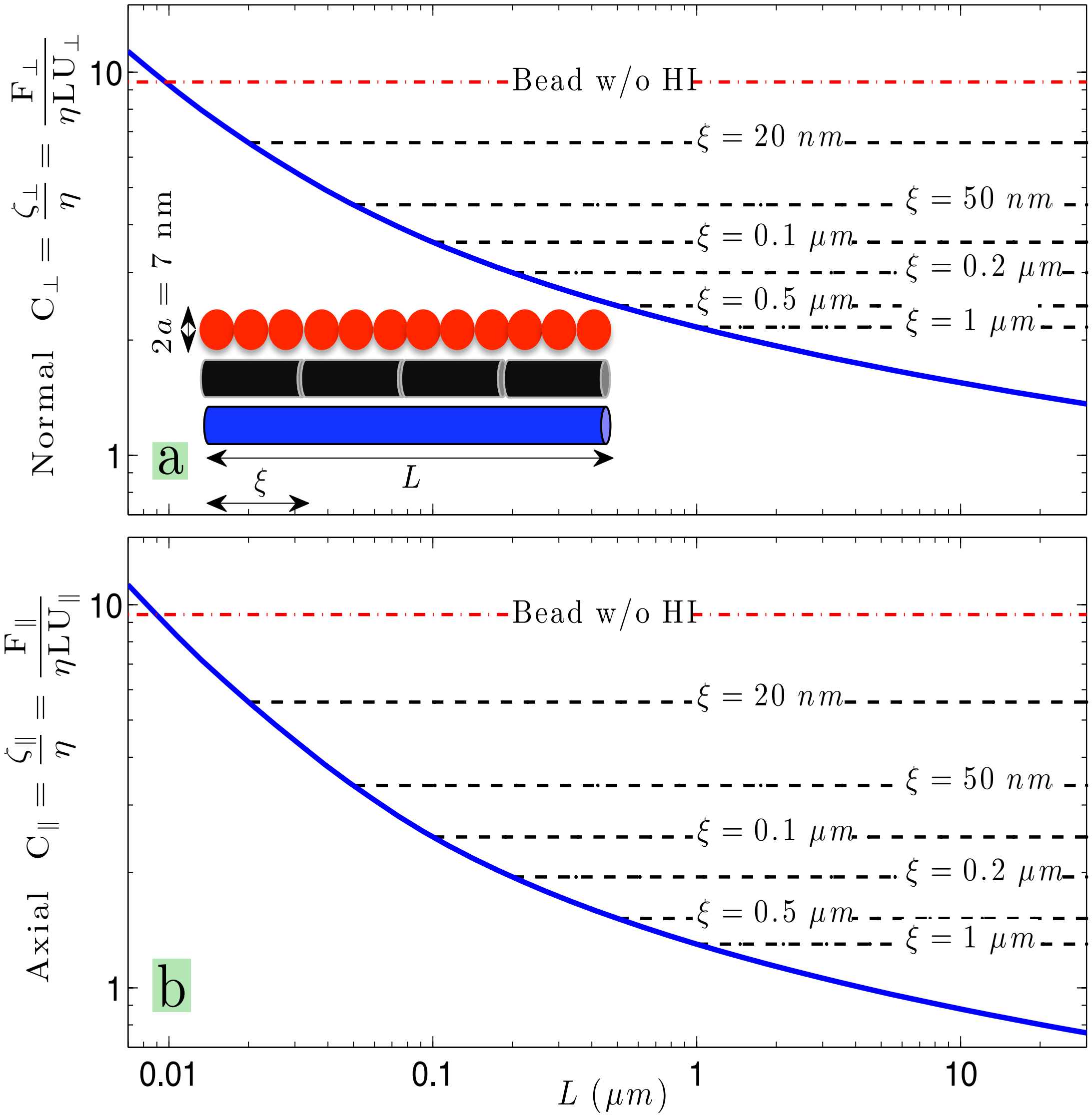

Figure 5-3: Dimensionless (a) normal ($C_\perp$), and (b) axial ($C_\parallel$) drag coefficients of an actin filament (η: viscosity, U: velocity, a: filament radius). Blue line: reference values based on SB (Swanson-Batchelor) introduced in section 4.3.2 [15,16]. Dashed black line: discretized into mesh-sized, ξ, rods without HIs. Dash-dotted red line: discretized into beads with the same diameter as the filament without HIs. Inset shows different discretizations.

The viscous drag force on the filament is a function of the filament length (Fig. 5-3), as discussed in section 4.3.2 . These forces per unit length are inversely proportional to $\ln L$, where L is the filament length[122,123]. This nonlinearity implies that the forces summed over smaller segments are overestimating the net force on the filament. However, generally in theoretical and computational models and specifically in the commonly-used tube model, the drag forces are based on the coefficients corresponding to the drag for the effective mesh size, ξ[111]. Depending on the concentration of crosslinkers and actin, ξ can vary between $20\ \mathrm{nm}$ and $1\ \mu\mathrm{m}$. Ignoring the HIs between these segments could lead to erroneous net forces, which can yield erroneous deformation rates in force-induced movement and remolding of the actin network (see Fig. 5-3).

For example, $\mathrm{C}_{\parallel}$ (dimensionless axial drag coefficient) for a $30\ \mu\mathrm{m}$ filament is ~0.8 for the whole filament, and ~6 for the same filament broken into $20\ \mathrm{nm}$ rods. Consequently, if the HIs between those rods are ignored, an approximately 7-fold error is expected ($\frac{6}{0.8} \cong 7$). Alternatively, if a single filament is divided into ξ -sized segments to model its elasticity, its net diffusion would be inaccurate by the same factor. Additionally, larger errors, more than one order of magnitude, would be expected if the filament is discretized into beads without accounting for HIs, i.e. when the HI effect is ignored in the bead level (dash-dotted red line in Fig. 5-3). Our finding corroborates the earlier finding that only theoretical models which explicitly account for HIs can quantitatively match experimental dynamics of single actin measured via fluorescence correlation spectroscopy[112].

5.2.2 Lateral Fluctuations

Fluctuations of filaments, also affected by HIs, are related to the macroscopic behavior of actin. Indeed, lateral bending modes are the main contributor to the viscoelasticity of cross-linked actins[111,144,145]. These mode shapes can be derived from worm-like chain models of filaments as employed here. Unless otherwise noted, in all simulations henceforth, we discretize filaments into beads and adopt the Rotne-Prager tensor[115], which is the standard method for HIs (see chapter 4 for details). Since we are interested only in the hydrodynamic forces, we examine only a single time snapshot of the system in equilibrium. As a result, we do not need to include Brownian forces or elasticity of the network. While both of these factors play significant roles in the dynamics of cytoskeletal network, they have no direct effect on instantaneous hydrodynamic forces. These instantaneous forces depend only on system configuration and velocity distribution at low Reynolds number.

To calculate filament bending-modes we note that, since axial modes are expected to relax much faster than lateral modes, an equation of pure bending can be employed[146,147]:

$$\rho \frac{\partial^2 w}{\partial^2 t} + \zeta \frac{\partial w}{\partial t} + \epsilon \frac{\partial^4 w}{\partial^4 s} = A(s,t) \qquad \text{Eq. (5-1)}$$

Nomenclatures used in this section are fully described in Table 5-1. Worm-like chain models ignore variation of hydrodynamic drag coefficient on the filament due to the screening effect and instead utilize the constant ζ drag coefficient in Eq. 5-1. This coefficient is multiplied by the local velocity of the filament to calculate local hydrodynamic force per unit length responsible for decaying the filament vibrations.

Table 5-1: Nomenclatures used in analyzing filament fluctuations.

Symbol	Description
$\boldsymbol{w(s,t)}$	lateral displacement
$\boldsymbol{s}$	position index along filament axis $-\frac{L}{2} \leq s \leq \frac{L}{2}$ (L: filament length)
$\boldsymbol{t}$	time
$\boldsymbol{\rho}$	filament mass per unit length
$\boldsymbol{\zeta}$	filament lateral drag coefficient per unit length per unit lateral velocity
$\boldsymbol{\epsilon}$	bending elasticity constant
$\mathbf{A(s,t)}$	stochastic Brownian force
$\boldsymbol{\lambda_i, q_i}$	eigenvalue and mode shape i
$\boldsymbol{q_{\perp 0}}$ or $\boldsymbol{q_{\perp}}$	mode shape zero with pure lateral rigid body displacement ($q_{\perp 0} = 1$: no rigid body rotation)
$\boldsymbol{f_h}$	viscous drag force per unit length

Inertial terms, $\rho \frac{\partial^2 w}{\partial^2 t}$, can be neglected due to low Reynolds. Normal mode analysis is applied to Eq. 5-1 to arrive at the following q_i modes:

$$
\begin{aligned}
q_i &= As + B && i = 0 \\
q_i &= \frac{\cos\frac{s\lambda_i}{L}}{\cos\frac{\lambda_i}{2}} + \frac{\cosh\frac{s\lambda_i}{L}}{\cosh\frac{\lambda_i}{2}} && i = 1,3,5,\dots \\
q_i &= \frac{\sin\frac{s\lambda_i}{L}}{\sin\frac{\lambda_i}{2}} + \frac{\sinh\frac{s\lambda_i}{L}}{\sinh\frac{\lambda_i}{2}} && i = 2,4,6,\dots
\end{aligned}
\qquad \text{Eq. (5-2)}
$$

We model the vibrations of a single filament with free ends. Free-end assumption holds true for isolated low concentration networks. However, *in vivo*, most segments have ends attached to other filaments (e.g., via crosslinkers or branches generated by Arp 2/3). Hyperbolic terms in Eq. 5-2 are used to satisfy free end boundary conditions, but their contributions are negligible for higher modes or away from filament ends. Otherwise, in general the mode shapes are not sensitive to boundary conditions.

Mode shapes, q_i, are originally derived to represent the amplitudes of vibrations, but they can also be interpreted as the velocity profiles. Mode shapes are shown on Fig. 5-4-a.

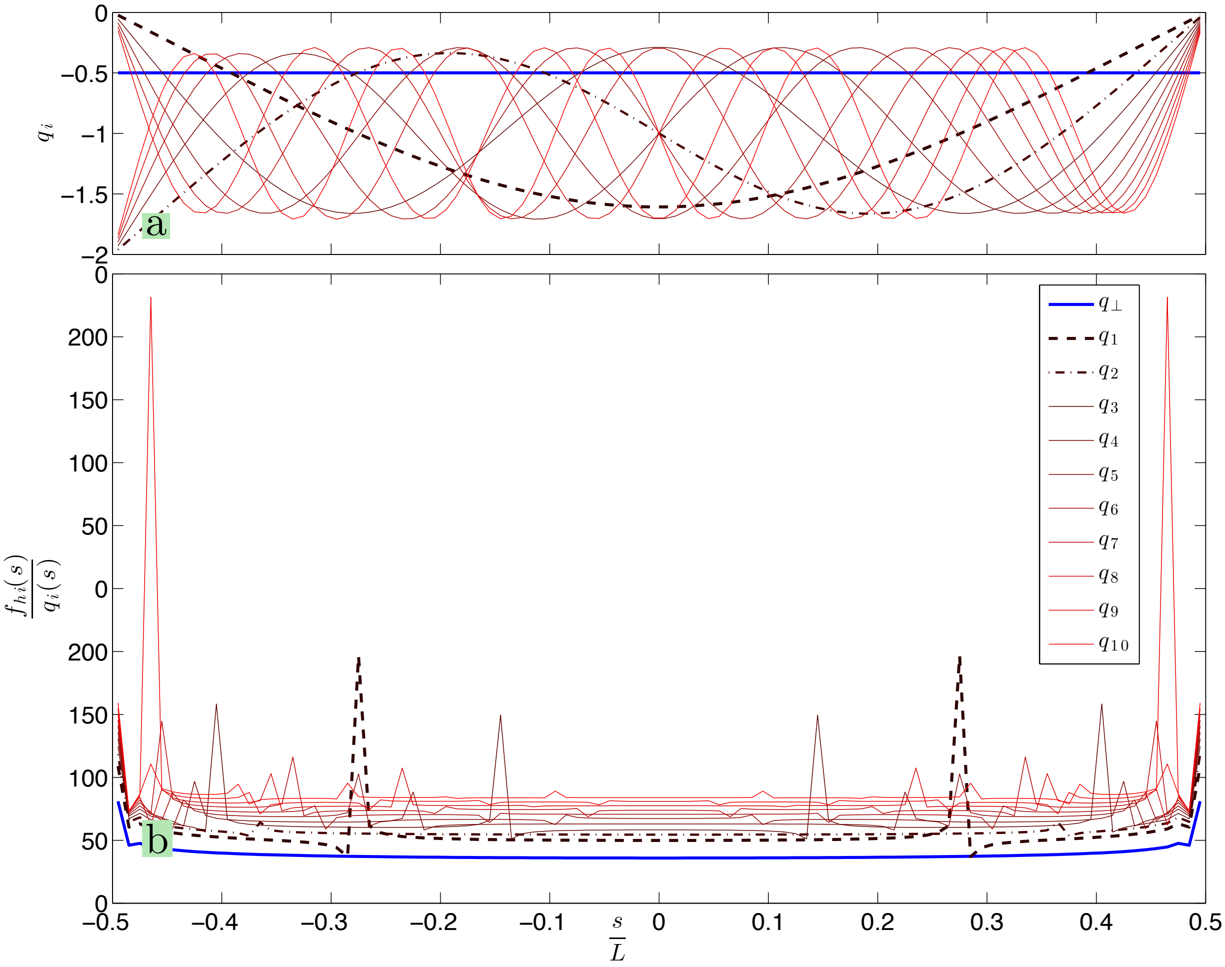

Figure 5-4: (a) Mode shapes and (b) local drag coefficient for a 0.7 µm filament at different modes. Solid blue line: rigid body lateral translational mode. Red shades: the first 10 modes. Brighter reds correspond to higher modes. Dashed and dash-dotted lines represent first and second modes respectively. This filament is discretized into 100 spherical beads each with a 7-nm diameter.

In Eq. 5-1, for simplicity it is assumed that the drag force is proportional to local filament velocity. However, we already know that even in $q_{\perp 0}$ mode (simply called $q_\perp$ henceforth), the drag force is not uniformly distributed. Based on the velocity profile of a given mode, q_i, we can calculate drag force profile $f_{h\,i}$ and examine the linearity between local velocity and local drag force. Mode shapes, q_i, and $\frac{f_{h\,i}}{q_i}$ ratios are plotted in Fig. 5-4-b for a filament with

$L = 0.7\,\mu m$. We can note that for this filament length and others not shown here, $\frac{f_{h\,i}}{q_i}$ is almost constant far from free ends and singularities (when q_i is zero), but slightly different for different modes. Next we try to quantify these variations.

We define the following normalized internal product as a measure of how much $f_{h\,i}$ and q_i are proportional:

$$q_i \otimes f_{h\,i} \overset{\text{def}}{=} \frac{\int q_i f_{h\,i} ds}{\sqrt{\int {q_i}^2 ds \int {f_{h\,i}}^2 ds}} \qquad \text{Eq. (5-3)}$$

According to Cauchy–Schwarz inequality, we know that $|q_i \otimes f_{h\,i}| \leq 1$ and only if $f_{h\,i}$ and q_i are exactly proportional, then $q_i \otimes f_{h\,i}$ will be equal to ± 1. Absolute values smaller than 1.0 correspond to functions that are not well aligned. From the physical perspective, local power consumed against viscous medium is proportional to $q_i f_{h\,i}$ and hence $q_i \otimes f_h$ can also be interpreted as the power ratio of f_h contained in the q_i mode.

Results in Fig. 5-5 indicate that for the first 10 modes of filaments between $140\,nm$ and $30\,\mu m$ long, $f_{h\,i}$ power is more than 95% contained in the corresponding mode q_i. Consequently, based on Fig. 5-5 and Fig. 5-6-inset, we conclude that force distribution due to hydrodynamic interactions does not alter normal modes substantially and hence application of a constant drag coefficient per unit length is a valid approximation (at least for lower modes considered here).

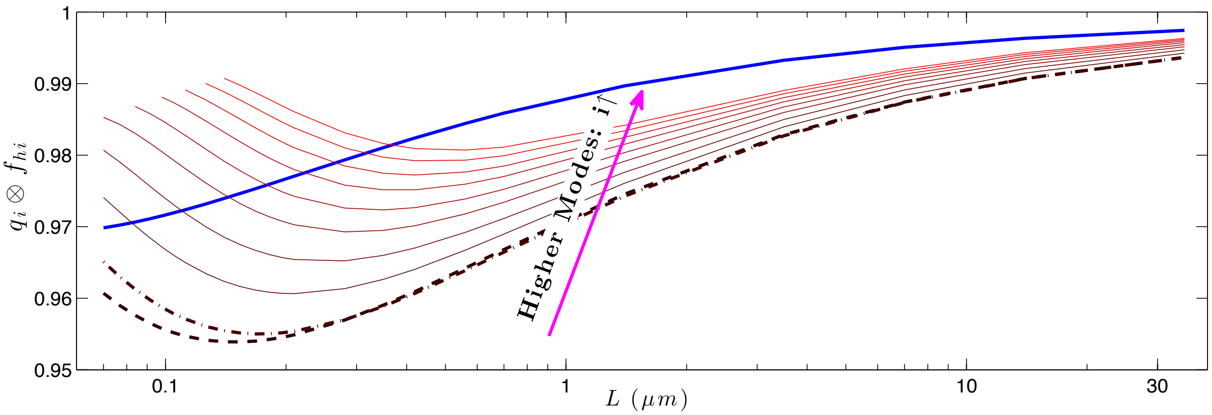

Figure 5-5: Normalized internal product of mode shape and hydrodynamic force, $q_i \otimes f_{h\,i}$, for different modes. Line styles match legend of Fig. 5-4-b. This internal product represents a power ratio (out of 1.0) for the component of the hydrodynamic force consistent with assuming a uniform drag for each mode (i.e., ignoring local variations in the drag coefficients, shown in Fig. 5-4-b, due to hydrodynamic interactions).

However, as is evident from Fig. 5-4-b, $\frac{f_{h\,i}}{q_i}$ has a variable value depending on the mode number and hence we require a ζ value to be dependent on the mode number. Generally ζ is approximated based on its value from $q_\perp$ mode, simply called $\zeta_\perp$ (Fig. 5-3 for actin filaments), as follows:

$$\zeta \cong \zeta_\perp = \frac{\int f_{h0} ds}{q_{\perp 0} \int ds} \qquad \text{Eq. (5-4)}$$

Eq. 5-4 cannot be used for higher modes because for them q_i is not constant (i.e., $q_i = q_i(s)$). To extend the above equation to higher modes, it might look natural to replace the denominator with $\int q_i ds$. However, for higher modes, $\int q_i ds$ is zero or close to it. Hence instead, we modify Eq. 5-4 to Eq. 5-5 to be applicable to higher modes. This new form, Eq. 5-5, eliminates plus and minus terms cancelled in both numerator and denominator in Eq. 5-4 simple extension ($\frac{\int f_{hi} ds}{\int q_i ds}$). Nonetheless, this new form results in the same $\zeta_\perp$ value for $q_\perp$ mode.

Eq. 5-5 is similar to Eq. 5-3 (definition of $q_i \otimes f_{h\,i}$), and can be considered as a way to calculate an average proportionality factor between $f_{h\,i}$ and q_i by avoiding singularities in $\frac{f_{h\,i}}{q_i}$.

$$\zeta_i \stackrel{\text{def}}{=} \frac{\int q_i f_{h\,i} ds}{\int q_i^2 ds} \qquad \text{Eq. (5-5)}$$

In fact, above ζ_i value is an optimal choice to minimize following integral: $E_i(\zeta) \stackrel{\text{def}}{=} \int (f_{h\,i} - \zeta q_i)^2 ds$, and by this optimal value we can show that square error follows this formula: $E_i(\zeta_i) = (1 - (q_i \otimes f_{h\,i})^2) \int {f_{h\,i}}^2 ds$. This $E_i(\zeta_i)$ formula provides a mathematical insight into the interpretation of $q_i \otimes f_{h\,i}$, which is used in the next part as a normalized root mean squared error to examine linear fit quality ($RMSE_i \stackrel{\text{def}}{=} \sqrt{\frac{E_i(\zeta_i)}{\int {f_{h\,i}}^2 ds}} = \sqrt{1 - (q_i \otimes f_{h\,i})^2}$ depicted in Fig. 5-6-inset).

Results of Eq. 5-5 are normalized as $\frac{\zeta_i}{\zeta_\perp}$ values depicted in Fig. 5-6 . We can think of $\frac{\zeta_i}{\zeta_\perp}$ as a measure of how much higher modes receive higher drag forces due to less screening effect. Additionally, since relaxation time of each mode is proportional to ζ_i, then $\frac{\zeta_i}{\zeta_\perp}$ is also an indicator of how much the relaxation time is underestimated, if as usual we use $\zeta_\perp$ instead of ζ_i.

To examine linearity of $f_{h\,i}$ and q_i pairs, we minimized $E_i(\zeta) \stackrel{\text{def}}{=} \int (f_{h\,i} - \zeta q_i)^2 ds$ (a squared error integrated over filament length) to find an optimal ζ_i value defined as the effective drag of mode i. We define $\mathrm{RMSE}_i \stackrel{\text{def}}{=} \sqrt{E_i(\zeta_i)/\int f_{h\,i}{}^2 ds}$ as a root mean squared error to quantify our fit quality. It was observed that for the first 10 lateral bending modes of actin filaments $140\,nm$ to $30\,\mu m$ long, a uniform drag coefficient can result in 10% to 30% $RMSE_i$ in drag (Fig. 5-6-inset). Interestingly, higher modes have a better proportionality between the velocity and the drag force. As expected, higher modes have shorter wavelengths and hence have more cancellation between positive and negative fluid velocity disturbances. Therefore, we conclude that HIs have a subtle effect on altering mode shapes due to local variations of drag coefficient.

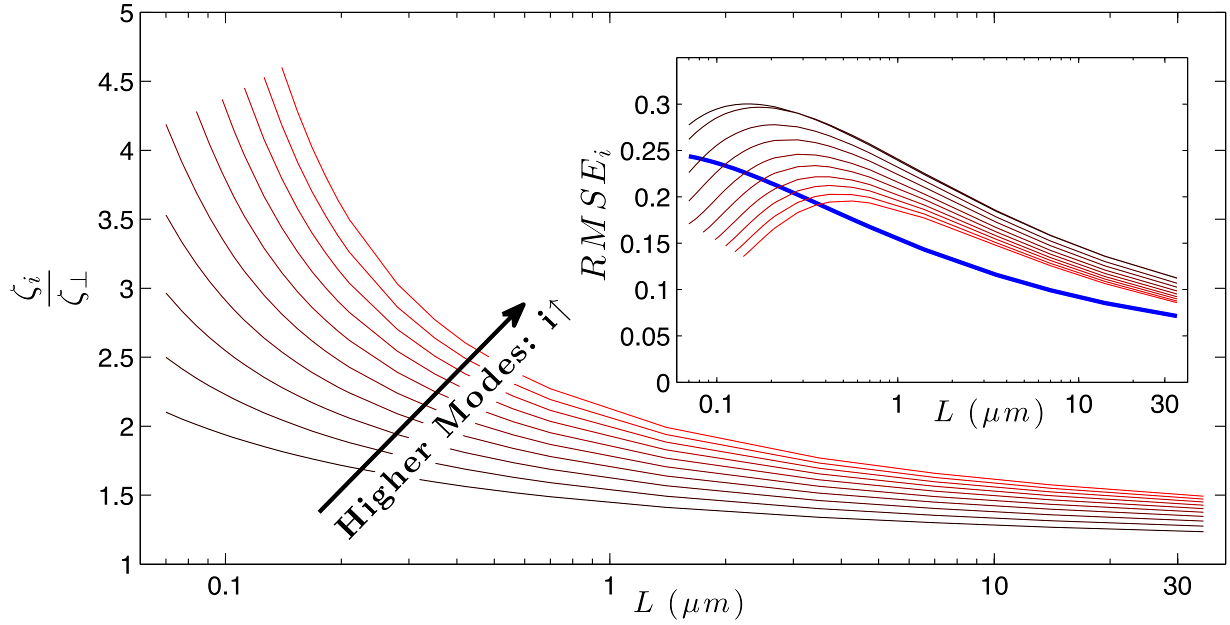

Figure 5-6: HI effects on the first 10 lateral bending modes versus actin filament length (L): The ratio of drag coefficient for a given mode compared to the drag coefficient of rigid body lateral translation is plotted here. This ratio is the same as the underestimation in relaxation time of those bending modes, if we use $\zeta_\perp$, instead of ζ_i Inset: the normalized root mean squared error of linear fit to examine proportionality between local velocity and local drag. Blue line: rigid body lateral translational mode. Red lines: the first 10 bending modes (brighter colors: higher modes).

On the other hand, the same cancellation means that filament segments cannot take advantage of screening effect to reduce their drag coefficient. Generally, drag coefficient obtained from rigid body lateral translation, $\zeta_\perp$ (Fig. 5-4-a), is used to calculate relaxation times in the tube model. Lateral modes seem to have an effective drag coefficient higher than $\zeta_\perp$ value. The ratio $\frac{\zeta_i}{\zeta_\perp}$, where ζ_i is the effective drag coefficient of mode i (Fig. 5-6) can be used as a more accurate numerical pre-factor in the tube model calculations. For instance, let us consider a network with a crosslinker distance l_c equal to $100\,nm$, which means we are interested only in the vibrational modes corresponding to a filament with $100\,\mathrm{nm}$ length or less. As indicated in Fig. 5-6, without the inclusion of HIs, the relaxation time of the first mode is underestimated by a factor of 2. Higher modes decay even more slowly than what is predicted from $\zeta_\perp$. Indeed experimental data for both actin and microtubule filaments suggest that higher wave numbers have an effective drag coefficient higher than that suggested by $\zeta_\perp$. Although such observations have been linked to internal viscosity of the filament[148,149], here we note that they might also be due to HIs especially in actin filaments whose internal structure is simpler and non-hollow.

It should be noted that typically mesh size of actin filaments are less than their persistence length, and hence, during deformation of an actin network the dominant mode of movement is local rigid body displacement (i.e., $q_\perp$ for lateral and $q_\parallel$ for axial motions) covered in section 5.2.1 . Similarly, in section 5.4.3, we investigate the rigid body displacement of a 3D cross as the representative repeating unit of a 3D regular network. Nonetheless, entropic elasticity of each filament is dominated by the relaxation times covered in this section[150-153].

5.3 Hydrodynamic Interactions in Bundle Formation

5.3.1 Geometry and Assumptions

As depicted in Fig. 5-1 and 5-2, F-actin uses various crosslinkers to form different network structure. Bundled (composite) networks are based on thick fibers (e.g., stress fibers) formed by (crosslinked) aligned filaments. In particular, cell movement utilizes acto-myosin machinery to pull the cell body by forces transmitted via stress fibers. When the bundles are formed, they approximately can be treated as a single filament, but with a bigger diameter. Increased diameter leads to increased hydrodynamic interactions similar to the results in former section. Consequently, in this section we focus on the process that leads to the bundle formation. Bundle formation is based on filaments being aligned, generally by the following two mechanisms[154], both depicted in Fig. 5-7:

1. Acto-myosin: sliding of anti-parallel filaments.
2. Zipper action of crossed filaments:
    a. Passive crosslinkers (they do not slide on F-actin): several crosslinker gradually align the filament.
    b. Myosin for crossed and parallel filaments: (one) myosin crosslinker gradually moves toward barbed end and aligns the filament.

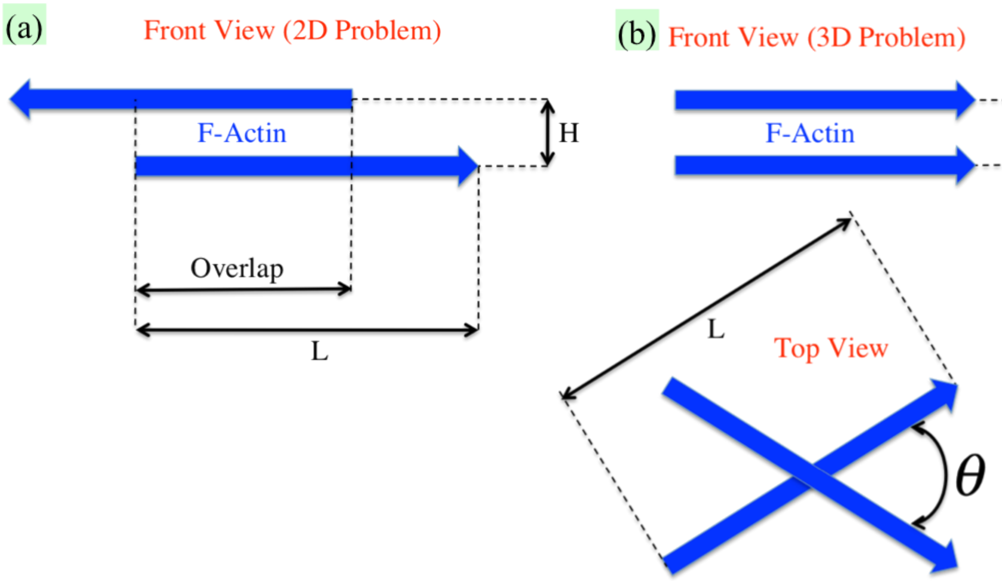

Figure 5-7: Two F-actin filament being aligned. (a): Acto-myosin: sliding of anti-parallel filaments. (b): Zipper action for crossed parallel filaments. The same geometry also applies to passive crosslinker; although for passive crosslinkers, the directionality of F-actins is not important.

As depicted in the Fig. 5-7, to model above phenomena, we restrict ourselves to two F-actins with the same length (L) moving toward each other symmetrically (i.e., the net movement of the center of the mass is zero). However, as depicted in Fig. 5-8, during cell migration one filament can be fixed (i.e., via focal adhesion), and the other filament can be pulled toward the fixed filament (to move the cell body). The later case can be considered as a combination of rigid body displacement (discussed in the previous section), and an alignment process.

We also assume that filaments have a fixed distance (H) from each other. This might be true, if the filaments are not attached to elsewhere. However, otherwise filament will bend locally before being aligned. Consequently, here we assume that all energy or power is consumed against viscous fluid, but in crowded environments, part of the energy could be consumed against bending or steric forces.

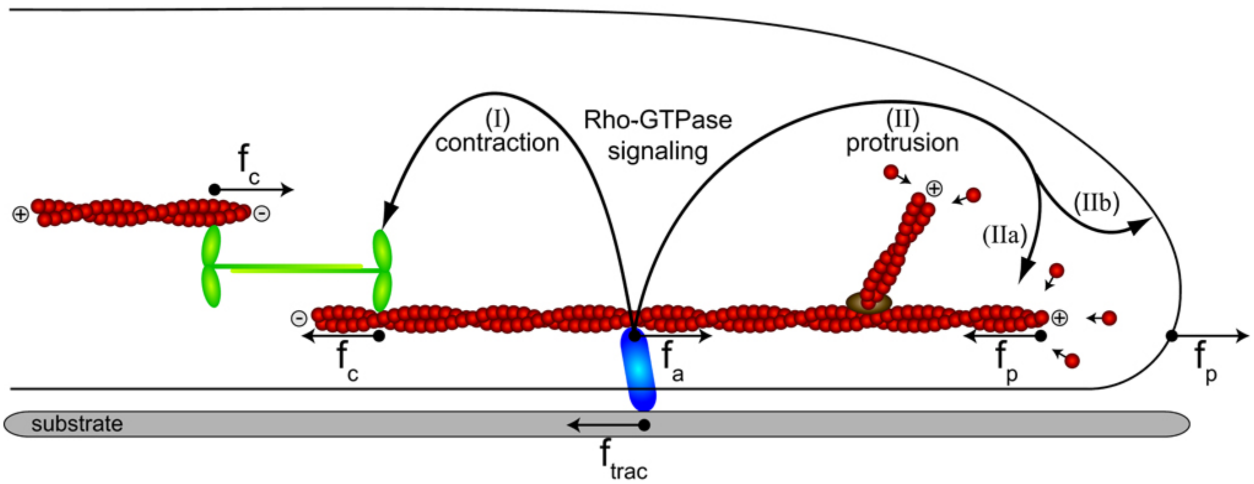

Figure 5-8: Acto-myosin force balance during cell migration. Myosin forces can be balanced with filament movements, force transfer to substrate via focal adhesion, retrograde flow, etc. Picture taken from danuser lab (http://lccb.hms.harvard.edu/research.html).

Nonetheless, for a first order of approximation, we calculate forces/torques (F: force, T: torque) required to move/rotate filaments in the absence and presence of hydrodynamic interactions between the two filaments (force: $F_{\text{with HI}}$ or $F_{\text{w/o HI}}$, torque: $T_{\text{with HI}}$ or $T_{\text{w/o HI}}$). In the absence of other time limiting factors (e.g., filament bending or acto-myosin sliding-rate limit), the ratio between $F_{\text{with HI}}/F_{\text{w/o HI}}$ or $T_{\text{with HI}}/T_{\text{w/o HI}}$ can determine how much filament alignment dynamics can be affected with hydrodynamic interactions.

H, distance between filaments, can have different values depending on the size and orientation of the crosslinkers. We calculated the hydrodynamic interaction for when the crosslinker is perpendicular to the filament, and hence, the distance between filaments is maximized. Crosslinkers, which are typically, overall smaller than the filament, can be at the center between filaments, where the net distributed flow velocity due to HI is zero, and hence, we have ignored their role in HIs. Nonetheless, eventually crosslinkers could be almost aligned with the filament to form a highly packed bundle. In that case, HI effects can be elevated due to closer distance. Hence, our HI factors ($F_{\text{with HI}}/F_{\text{w/o HI}}$ or $T_{\text{with HI}}/T_{\text{w/o HI}}$) might be interpreted as lower-estimates.

5.3.2 Sliding of Antiparallel Filaments

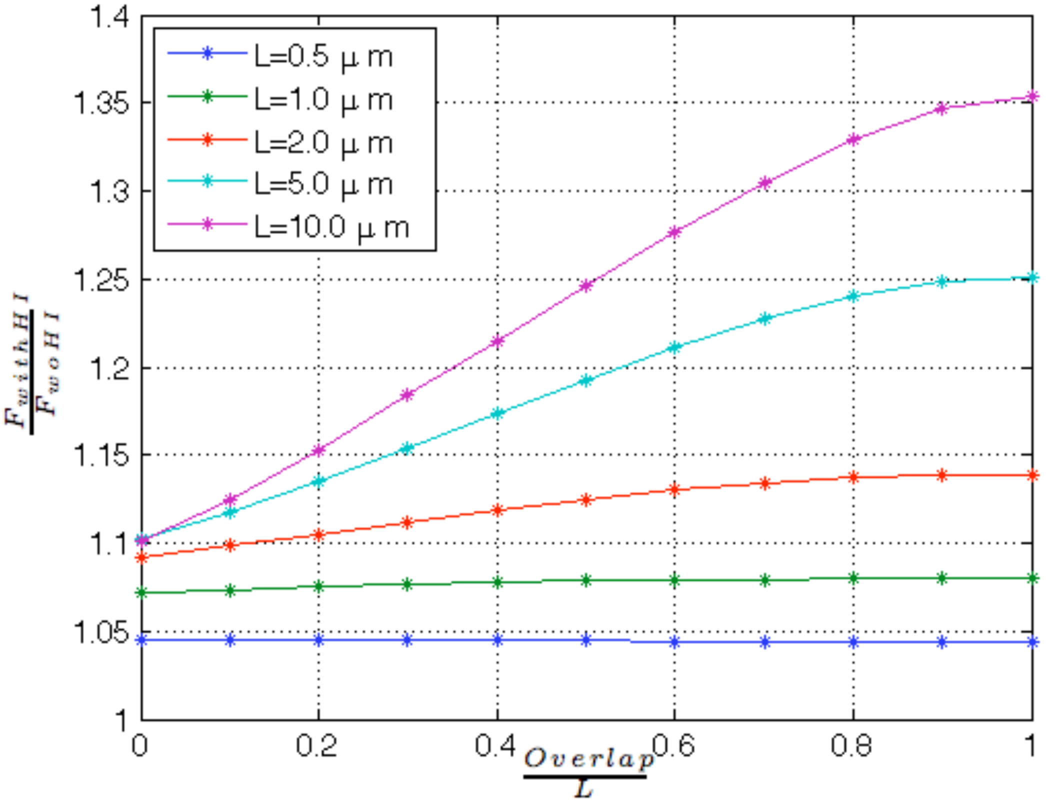

Figure 5-9: Effect of hydrodynamic interactions between two antiparallel F-actins being aligned by myosin. F represents axial force. Overlap and L are defined in Fig. 5-7.

We start by simulating the acto-myosin sliding of two antiparallel filaments at different lengths. Due to size of myosin, we assume that H=707 nm (and as before a=3.5 nm as actin radius). Interestingly, for filaments shorter than $1\,\mu m$ depicted in Fig. 5-9, HI effects are totally negligible regardless of the overlap length (less than 7%). In fact, it looks like that if the filament (overlap) length is about the same order as the closest distance between the two filaments, then the HI effects can be ignored.

It is also interesting that the $F_{\text{with HI}}/F_{\text{w/o HI}}$ factor is almost the same for all the filaments larger than $2\,\mu m$ at Overlap=0 case. This can be interpreted by realizing that the portion of the filament that is beyond the $2\,\mu m$ front has almost zero hydrodynamic interaction with the other filament. We further checked this by plotting $F(s, Overlap)$ (hydrodynamic force as a function of bead position and overlap) depicted in Fig. 5-10 for 3 values of overlap. That curve clearly shows that during $|Overlap| \gg L$, there is not any hydrodynamic interaction between filaments, and hence, the force is like when they are isolated but moving with the same speed

(Fig. 5-10 black line). On the other hand, when $Overlap = L$, we have the maximum force (Fig. 5-10 blue line). In the between, the portion of the filament that has overlap switches to the maximum force and the rest remains relatively unchanged (Fig. 5-10 red line for $Overlap = L/2$). In fact, in the corresponding animation it looks like that a smooth wave moves with the same speed as the filament, and switches the overlapping beads to the higher force values. Since this pattern holds for both axial and lateral force, this phenomenon might be observed experimentally by seeing a dent (bending) moving across filament with the same speed.

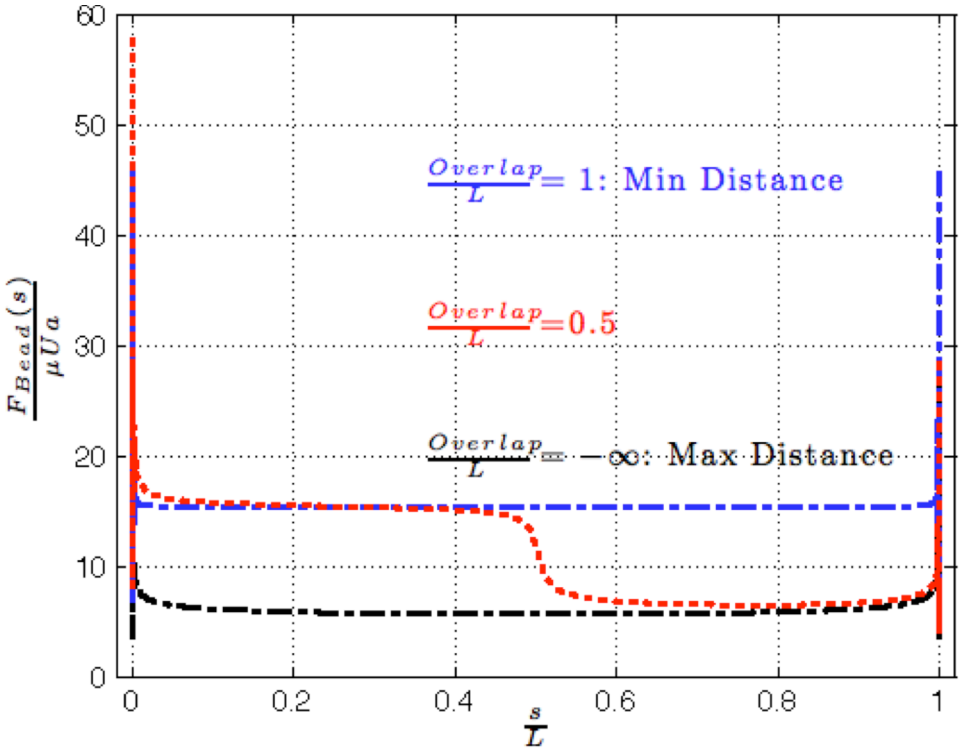

Figure 5-10: Normalized force distribution, $F(s, Overlap)$, for 3 overlap values: blue) side by side and maximum force, red) half side by side, black) at distance infinity corresponding to minimum force . This simulation corresponds to two 10 μm antiparallel actin filament coming side by side. We chose H=47 nm to elevate HIs and have a curve that better distinguishes the above 3 states. Nonetheless, H=707 nm results in the qualitatively similar curve, but with a less steep wave front. Force values near free ends, s=0 and 1, have fluctuations due to approximations in HIs tensor. (μ: viscosity, U: velocity, a: filament radius)

5.3.3 Zipper Action of Crossed Filaments

As described in Fig. 5-11, we tested two different crosslinkers, namely myosin and α-actinin by choosing different values for H.

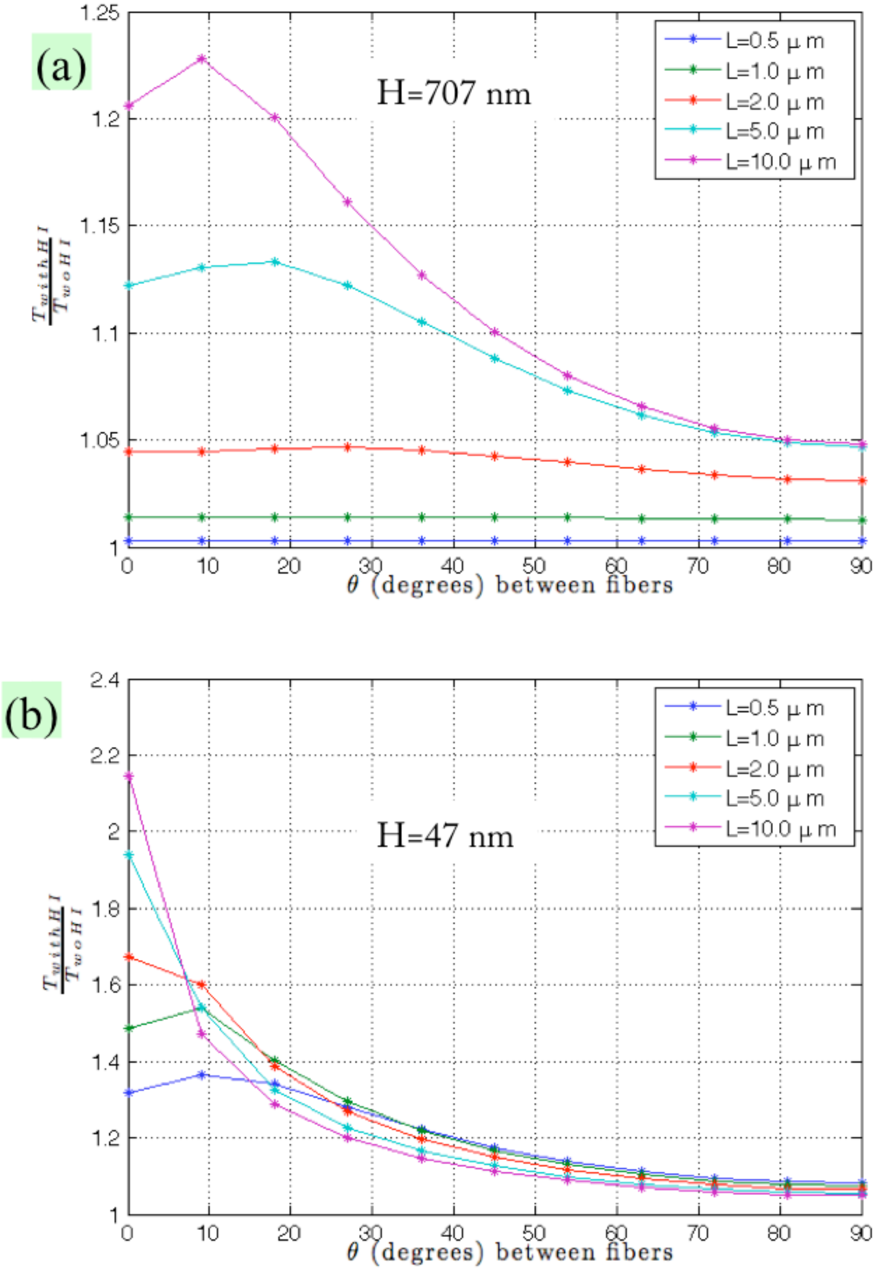

Figure 5-11: Effect of hydrodynamic interactions between two crossed F-actins being aligned. (a): H=707 nm, simulating myosin for crossed and parallel filaments. (b): H=47 nm, simulating passive crosslinkers representing α-actinin. T represents the torque required to rotate the filaments. θ and L are defined in Fig. 5-7.

Conclusions similar to section 5.4.3 can be made here as well. For example, when filaments are perpendicular (i.e., $\theta = 90°$), the exact length of the filament does not appear in HI factors. On the other hand, when they gradually align, they start to see the full length of each other and interact with all their body.

For myosin cases, both antiparallel and crossed, the HI factors were at most 1.35 . Hence, we can expect up to 35% slow down in their movement dynamics, if we ignore HIs. While 1.35 might look like a small number, 35% change in the rates can be measured experimentally. Furthermore, for the α-actinin case, the HI factor can go up to 2.2, meaning that dynamics can be severely miscalculated if we ignore HIs. Finally, we can realize that HIs can be more significant at the frontal edge of the cell (or near membrane), where actin filaments are densely packed by similar small crosslinkers. Comparing our cases for H=47 and 707 nm can also provide us with rough estimates on how HI effects might be different, when our packing density changes.

5.3.4 Verification of Simplified Rod Model

We also used the antiparallel case as a benchmark for our approximate rod model. We have plotted HIs factors in Fig. 5-12 for two antiparallel filaments. We have also plotted the bead method data (formerly plotted in Fig. 5-9) as our reference values. For different filament lengths, $0.5\,\mu m$ to $10\,\mu m$, and at different values of overlap, we compared rod method and bead method (both method introduced in Chapter 4), while varying the number of the rod segment (from 1 to 2000). As depicted in Fig 5-12, we found that for all cases by increasing the number of segments both methods converge to the same results. This also holds true for the similar problem of zipper action of crossed filaments, which we have not shown here in the interest of space.

According to Fig. 5-12, with only 5 segments, we can ensure an error less than 5%. This is significant, because bead method for a $10\,\mu m$ filament requires $10\,\mu m/7\ nm \cong 1429$ beads. On the other hand, rod method requires only 5 segments for the negligible 5% error. Given that HI matrix scales as the squared number of the particles, rod method requires $(1429/5)^2 \cong 0.82\times10^5$ less memory and similarly less computational time and resources.

Therefore, we realize that the application of our rod method can decrease the computational resources required by up to *5 orders of the magnitude*. This is highly significant, since it opens a door to include HIs in problems with larger length scales. Those new problems can be in various different fields, and hence, this method has a potential impact far beyond cytoskeletal mechanics.

Here, we have used filament radius as the Stokes radius in our rod method. Furthermore, relating to the discussion in section 4.3.4 , we found that Rotne-Prager tensor works as the best candidate for including HIs. However, we could not point out to any particular best candidate for Stokes radius.

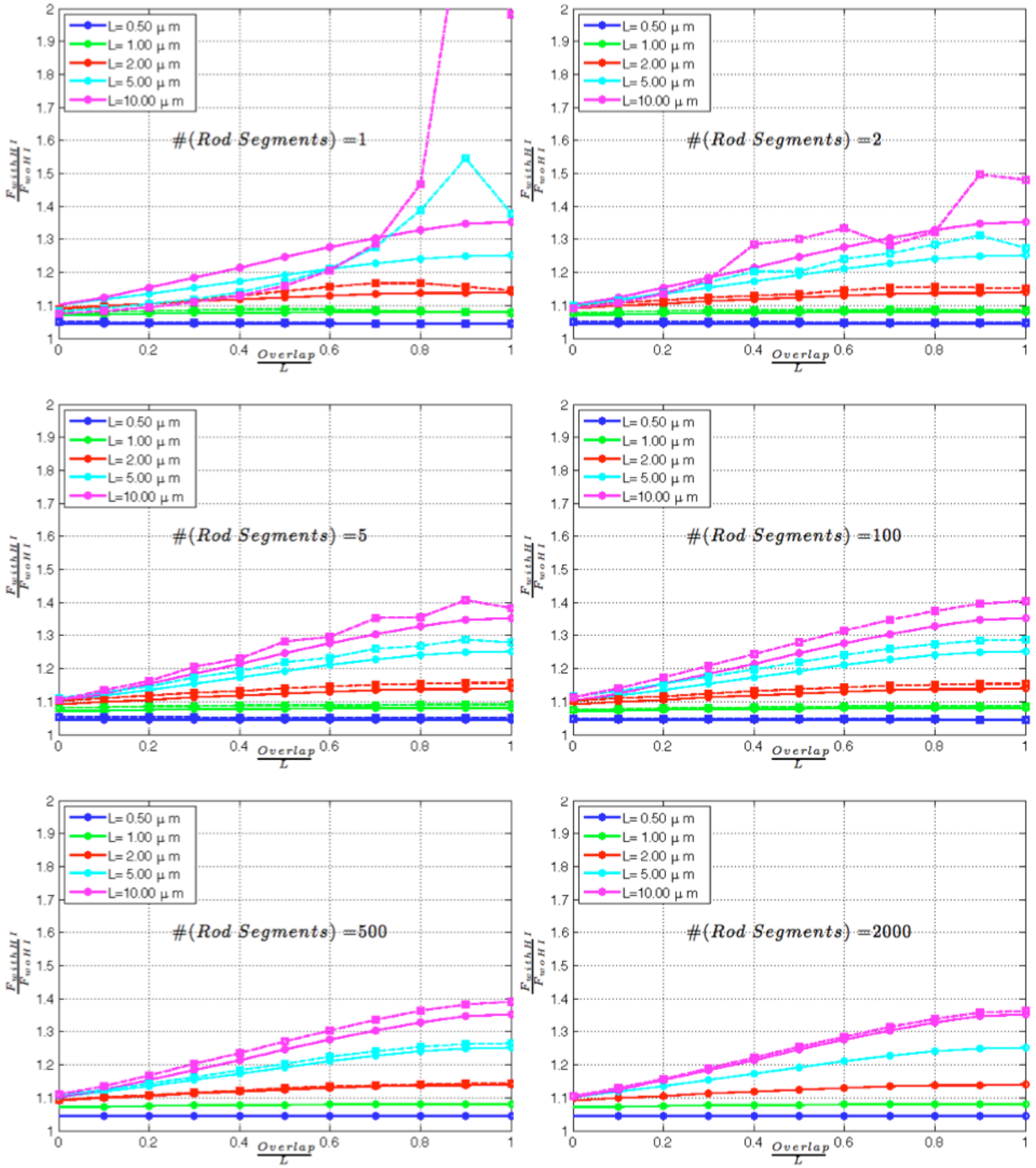

Figure 5-12: Comparison of approximate rod model and bead model for effect of hydrodynamic interactions between two antiparallel F-actins being aligned by myosin. Bead model: solid line with circular marker. Rod model: dashed line with square marker. Different graphs vary on the number of rod segments used for discretization of each filament. X-axis: $\boldsymbol{Overlap/L}$. Y-axis: $\boldsymbol{F}_{\text{with HI}}/\boldsymbol{F}_{\text{w/o HI}}$. F represents axial force. Overlap and L are defined in Fig. 5-7.

It should be noted that the strong variations in the Fig. 5-12 for low number of rod segments (1, 2, or 5) is a numerical artifact. This artifact is cleared, when we use higher number of rod segments, and hence, the rod method results converge to the bead method results. This artifact can be attributed to two factors.

Firstly, the pure bead model is susceptible to some unphysical variation of the force. For example, we can solve the HI equations for the rigid body motion of a single filament discretized into beads (Fig. 5-4-b blue line). Then, we can see that near free-ends force oscillates, whereas in the physical system, force increases monotonically toward filament ends.

Secondly, axial and lateral HIs have different strengths, and hence, for two single beads the position corresponding to the minimum distance, might not match the position with maximum HIs. This idea is depicted in Fig. 5-13 for two spherical beads, representing a similar problem to Fig. 5-3-#(Rod-Segments)=1. In both problems, the maximum HIs can happen around a point in which velocity partly results in an axial HIs (which is stronger than lateral HIs). This can be the main reason for overshoot in Fig. 5-3-#(Rod-Segments)=1 between $overlap/L$=0.8 and $overlap/L$=1.0 .

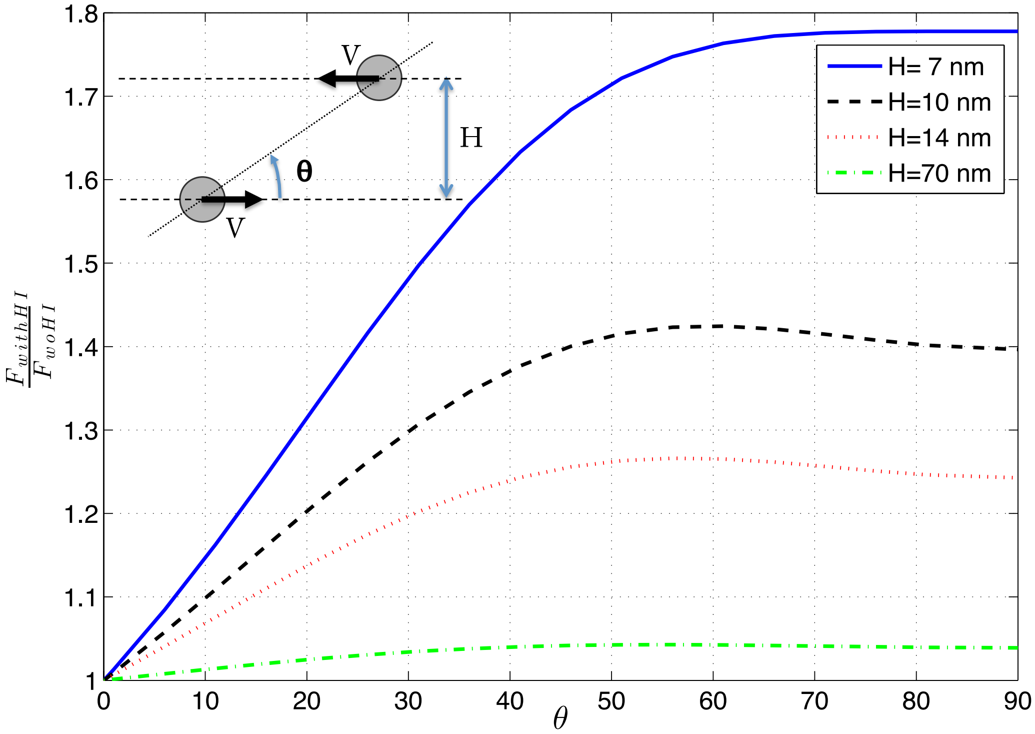

Figure 5-13: Effect of HIs between two beads moving toward each other with equal speeds on H-spaced parallel lines. Beads have a 7 nm diameter, equal to the diameter of F-actin. System geometry is shown on the subset. The ratio plotted corresponds to the force component in parallel to V. Note that maximum interaction (peak value of y-axis) does not necessary happens when the beads have the minimum distance ($\theta = 90°$).

5.4 Hydrodynamic Interaction in Actin Networks

5.4.1 Idealized Regular 1D Network

In a dense network, each segment is closer to nearby filaments than remote parts of the same filament, and hence HIs can increase beyond what we reported in Fig. 5-3 for a single filament. To examine this, we build a simple 1D network composed of actin filaments uniformly spaced, 56 nm, parallel or perpendicular to each other (Fig. 5-14-subset). A uniform strain rate is applied on this network, in both shear and axial modes, and the force required to overcome fluid drag is calculated. This force can be considered as the stress required for imposing the desired strain rate ($\dot{\varepsilon}$).

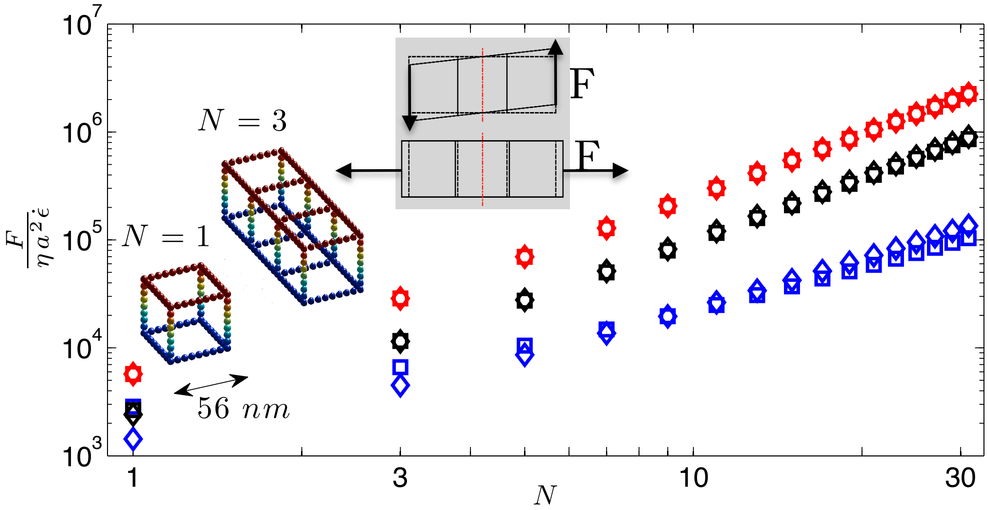

Figure 5-14: A regular 1D actin network built from different numbers of 56 nm units is devised, and dimensionless force to impose shear (diamond marker) or stretch (square marker) is calculated. Three methods for computing hydrodynamic forces are compared: 1) bead with HIs (blue), 2) mesh-sized rod segments w/o HIs (black), and 3) beads w/o HIs (red). When HIs are small, the markers overlay to appear as hexagonal stars. Inset: deformation modes and networks discretized into beads for N=1 and N=3 units. Beads are colored according to z-coordinate for 3D visualization.

In the elastic regime, a constant strain leads to a constant stress regardless of section depth. At a constant strain rate in viscous regime, in contrast, force is gradually transmitted to the fluid phase, and hence force increases with the addition of newer elements along the cross section (Fig. 5-14). In absence of HIs, this force would increase as a quadratic function of the section depth. However, due to HIs, the flow fields imposed by peripheral elements superimpose at the location of the central elements, and hence their smaller movement is similar to their surrounding fluid. Consequently, central elements are shielded or screened from surrounding stationary flow, force is fairly constant in central region, and overall the force is decreased (blue markers Fig. 5-14). A model *including* HIs can therefore better mimic the viscoelastic behavior that assumes for a given strain rate, stress is constant. Nonetheless, the poroelastic model is better suited to model stress variation at different depths.

Here, the hydrodynamic forces are calculated in three ways and together they demonstrate that ignoring HIs, be it between beads or rod segments, results in significant overestimation of force. Rod model of Fig. 5-14 is achieved by breaking each $56\ \mathrm{nm}$ unit to eight horizontal segments each $49\ \mathrm{nm}$ long (seven actin beads), and four vertical segments each $63\ \mathrm{nm}$ long (nine actin beads). For consistency, drag force of the rod model is still calculated based on segments discretized into beads, but any HIs between beads of different segments are ignored. Despite having different velocity fields, in comparison to Fig. 5-3, we notice that the overestimation factors are considerably higher for the same ξ. Clearly, if the same network units were assembled to build a 3D network, additional lateral HIs would result in even higher overestimation of stresses for the same deformation mode.

5.4.2 3D Network

Finally we consider a more physiologically representative 3D actin network, generated by $2.1\text{-}\mu m$ actin filaments randomly oriented at a sufficiently large box to achieve a $1\ \mathrm{mg/ml}$ [4] concentration at an inner cubic box of size $0.7\ \mu m$. This inner box is trimmed or extended periodically to build a cubic box of desired size S (Fig. 5-15-subset). S is a measure of network/system size and is used to investigate the effect of HIs in the loss modulus for systems of different sizes. Loss modulus or $\mathrm{G''}$ value is typically measured in the viscoelasticity tests as a function of frequency.

We simulate the network in the undeformed state and calculate viscous forces exerted by the fluid. Here we assume that undisturbed flow velocity, u_f, is zero uniformly. This means that any flow velocity is only due to the moving particles and otherwise the fluid is stationary. This assumption is a better match for actomyosin contraction and the cytoskeletal network where cytosol movement is a secondary effect, as opposed to the rheometer setup where walls directly induce (a linear) flow fields as used elsewhere[111]. In other words, here we are isolating the viscous forces due to network affine velocity field (corresponding to a harmonic affine deformation of the network in a stationary fluid), whereas Kim *et al.*[111] examined the contribution of the fluid affine velocity field for a network (non-homogenously) deformed by elasticity laws. Our study provides more accurate results for fluid effects, but the other assumption provides better results for elasticity and deformation in Brownian dynamics across different frequencies.

---

[4] $1\ \mathrm{mg/ml}$ is almost equivalent to $24\ \mu\mathrm{M}$, consistent with 43 kDa molecular mass of actin.

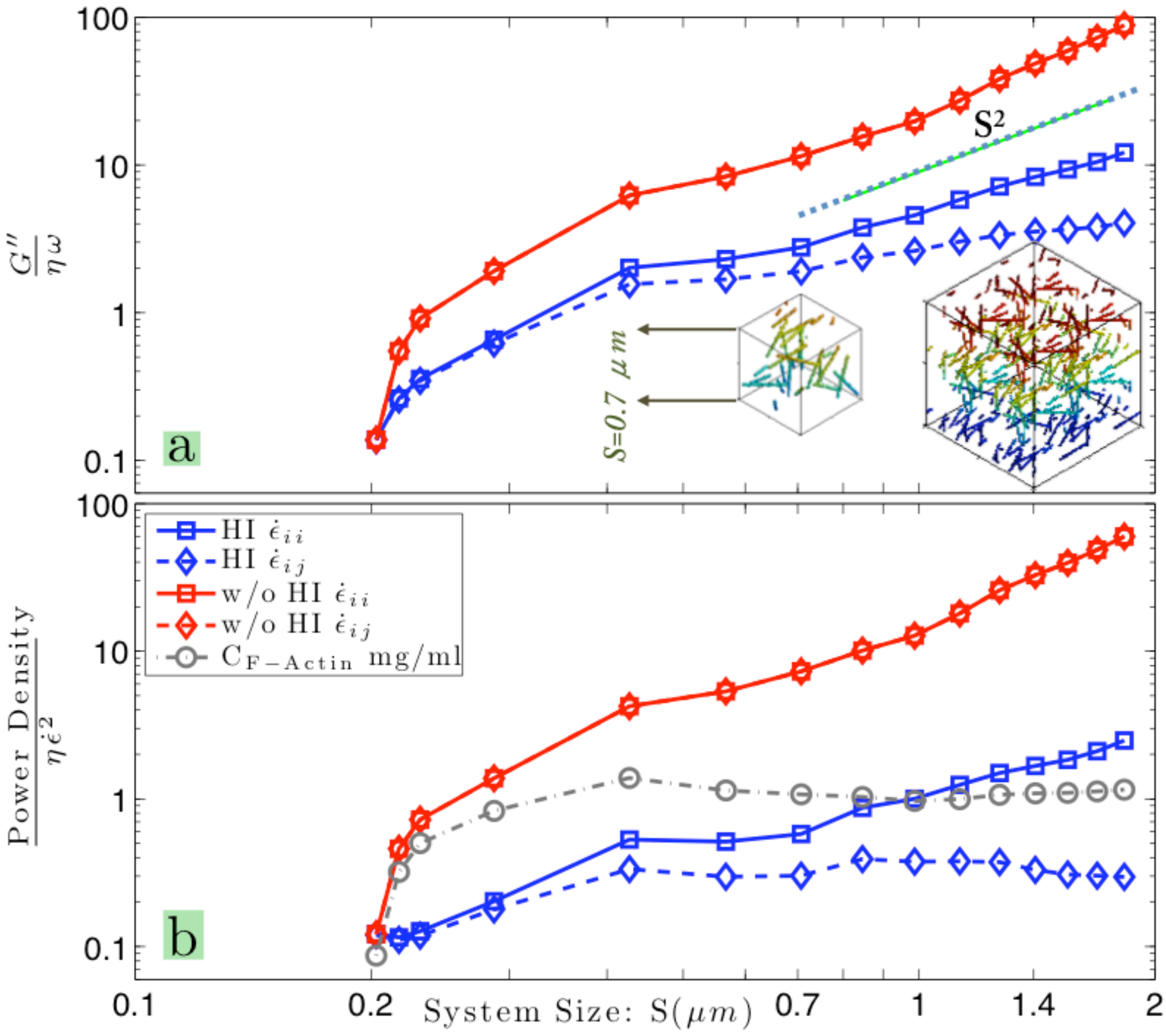

Figure 5-15: Dimensionless (a) loss modulus and (b) dissipative power per unit volume versus network/system size with HIs included (blue) and excluded (red), for uniform strain rate in pure axial elongation (square marker), and simple shear (diamond marker). Without HIs, the red markers overlay to appear as hexagonal stars. Solid dotted line in (a): L^2 scaling as the expected behavior when HIs are excluded and filaments are homogenously distributed. Gray dashed line in (b): F-actin concentration in mg/ml (on average 1 mg/ml). Subsets in (a): corresponding cubic networks for S=0.7 µm and 1.4 µm discretized into beads (colored according to z-coordinate for 3D visualization).

Ideally, we would like to combine both studies but it is beyond our computational power to perform time integration, and simultaneously solve elasticity and HIs non-sparse matrix for large length scales. Furthermore, the assumption of an affine deformation is an acceptable condition for isotropically crosslinked actin networks, to which we limit our study[150][5]. Indeed, Gardel *et al.* reported that actin networks, in general, deform uniformly at high concentration of actin and crosslinkers (similar to physiological condition in cell), as opposed to non-affine deformation for low concentrations[155]. It should be noted that although we did not include elasticity of the network in our calculations, this factor has been implicitly incorporated in our model with the assumption of an affine deformation.

In time domain, we have $\mathrm{F} \propto \dot{\varepsilon}$ (F: hydrodynamic drag force), which leads to $\mathrm{G}'' \propto \omega$ in the frequency domain. G" typically refers to shear, but we use this notion to refer to simple shear and pure axial elongation (deformation shown in Fig. 5-14-subset). However, the range of the frequency, ω, in which this holds is bounded at least between a lower limit due to the dissociation rate of crosslinkers, and an upper limit due to Stokes regime.

The crosslinker's life-time, about 20 sec, sets the lower limit to 0.05 Hz[150]. Additionally, for an oscillatory pure strain of 2%, the Reynolds number is calculated as $Re = 0.01\,\frac{\rho\omega L^2}{\eta}$ where L is the length scale and ρ is the cytosol density. If we set L=30 µm (the diameter of a cell), viscosity to η =5 cP for the cytosol and Re =0.1 as the upper limit for the Stokes regime, we find the upper limit of the frequency to be near 8.8 KHz.

The normalized loss modulus and dissipative power per unit volume for our simulated actin network are shown in Fig. 5-15. These values are obtained by averaging over three modes of uniaxial stretch and six modes of pure shear. Below $0.4\,\mu m$, there are steep changes, likely due to non-homogeneous density of the network at those length scales near ξ (0.3 μm for 1 mg/ml actin used here). Interestingly, beyond $1\,\mu m$, including HIs results in a fairly constant dissipative shear power as well as nearly constant G", similar to one-particle (1P) microrheology values measured at ~2 Hz by Gardel *et al.*[143] (based on $\eta = 5\,cP$ for cytosol).

Experimental study (typically for *in vitro* actin gel) and theoretical models report a $\mathrm{G}'' \propto \omega^{1/2}$ and $\mathrm{G}'' \propto \omega^{3/4}$ behavior respectively for low and high frequencies [143,151,152,156-158]. In the intermediate frequencies, and especially in the presence of crosslinkers, more complex behavior, including having a maximum and minimum in G" can be observed[142,144]. For sufficiently higher frequencies, solvent viscosity dominates and $\mathrm{G}'' \propto \omega$ behavior emerges[151].

Around 2 Hz, viscoelastic behavior follows $\mathrm{G}'' \propto \omega^{3/4}$ form consistent with the prediction of the tube model due to lateral bending[143,152]. Our model does not account for elasticity explicitly and our results are based on a single time snapshot of the undeformed system. Yet the confinement effects are rather accurately included to calculate G". This can be understood by noticing that at a length scale around ξ, actin filaments are rather rigid, and if no energy is consumed in breaking crosslinkers or deforming the filaments, all the forces are balanced against viscous medium.

---

[5] Our HI model does not include any crosslinker. However, crosslinkers are implicitly included by imposing an affine deformation. Furthermore, crosslinkers relative volume fraction is much lower than actin, and hence, they have a negligible role in drag forces.

On the other hand, in the axial deformation mode, the dissipative power and viscous modulus tend to increase with system size. This means that we have to either adopt a length-dependent axial loss modulus or decline to define it. This observation is similar to Fig. 5-14, where we denoted that poroelastic models better represent stress variations at different depths[159].

The loss modulus and dissipative power computed by *excluding* HIs (red markers) are also shown in Fig. 5-15, which increase rapidly with system size and diverge from the values including HIs. Therefore, loss modulus and dissipative power could be erroneous by nearly two orders of magnitude in the shear mode in the length scale we investigated if we exclude HIs (a ~20-fold overestimation for shear loss modulus). This again highlights the necessity of including HIs in any model that deals with network viscoelasticity. This is indeed a surprising finding, given that filaments are only occupying about 0.1% of the entire volume. As in Fig. 5-14, errors due to ignoring HIs could be decreased by using a rod model, but would still be significant if HIs between rods were ignored. To further examine this observation and to dissect error sources, an equivalent regular network (similar to Fig. 5-14, but in 3D) can be built in which a 3D-cross is envisioned as the repetitive network unit. An isolated 3D-cross reveals that *local* HIs (i.e., HIs within a volume size of ξ^3) are responsible for ~6.5-fold share out of this 20-fold error, leaving only ~3-fold error due to distant elements or potentially the finite variable size of the system (see details in the next section 5.4.3).

The computational burden of modeling the HIs limited our application to the 2 μm length scale, where we achieved results similar to 1P microrheology[143]. However, if we could overcome this computational limitation and model larger length scales, we might achieve results closer to macrorheology and examine the size dependency of the G" value[110,142,143,160,161]. Interestingly, we might be able to use our own rod model to push this length limit. While most studies cover frequency-dependent behavior of actin viscoelastic properties, to the best of our knowledge, no study has yet discussed the sample-size dependency of G" for crosslinked actin networks. Here we postulate that HIs may have a significant effect on modulating the G" value according to the system size. Nonetheless, according to Fig. 5-15, in the *absence* of HIs, the simulation box size has a significant role in calculation of G". Hence, care should be exercised in building consistent multiscale models of cytoskeleton, composed of elements with different sizes.

In summary, we show that HIs significantly alter the viscous forces required to deform and eventually remodel actin networks. Our observation is consistent with recent suggestions that crowding and hydrodynamic interactions likely dominate *in vivo* macromolecular motion[162]. We also show that HIs between elements of the actin network can alter their dynamics by at least 2-20 fold at different levels of network structure. Future studies are required to understand HI effects at larger length scales.

5.4.3 3D-Cross Model to Approximate Hydrodynamic Interactions Strength in a Network

In this part we explain a simple bead model to approximate the overestimation factors encountered in Fig. 5-15. According to Fig. 5-15, if we ignore hydrodynamic interactions, our results in shear modulus are erroneous by 20-fold. That is based on a model network in which filaments have random orientations. To simplify, we envision a regular network (similar to Fig. 5-14 but in 3D), in which filaments are uniformly spaced, are all parallel or perpendicular to each other and together build cubic units as depicted in 5-16-a. This network can be built by assembling 3D-cross units depicted in 5-16-b.

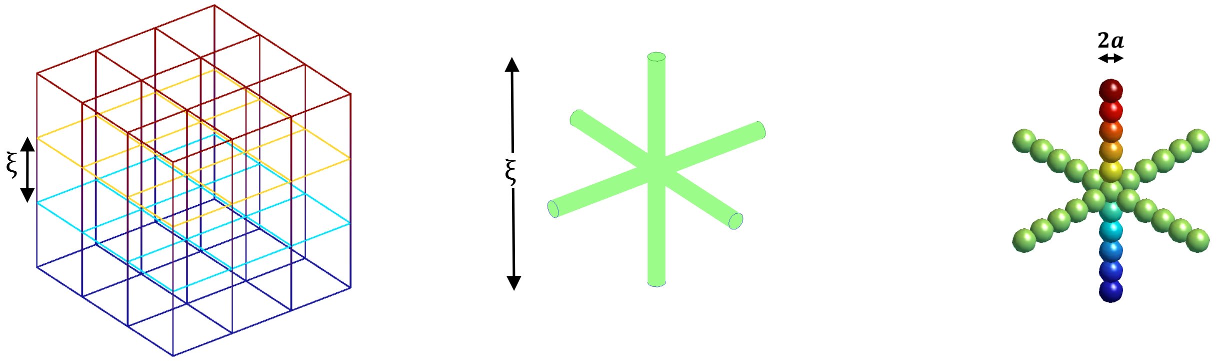

Figure 5-16: Simplification of a regular network into a 3D cross. (a): A regular network formed from filaments representing cubic units. This network is extended to infinity, but for simplicity only 3 units in each direction are plotted. Filaments are colored for better 3D visualization, but they are all identical. (b): 3D-cross as the repetitive unit of the network in part (a). All members of the cross have the same length (equal to mesh size: ξ). (c): 3D-cross discretized into beads. This specific number of beads correspond to $\frac{\xi}{2a}$=11 (a: filament radius). Beads are colored according to z-coordinate for better 3D visualization.

To calculate forces applied on the 3D-cross unit we make two important assumptions. Firstly, we ignore the hydrodynamic interactions between different units. It is generally assumed that hydrodynamic interactions are screened at length scales in the same order as the mesh size[147,163,164], hence this assumption is reasonable for our ξ-sized box.

Secondly, we ignore velocity variation in the 3D-cross and assume that it has a rigid body velocity equal to the velocity value at its central point. In fact, velocity varies linearly for affine deformation rate and its average value is equal to the velocity value at the central point. Furthermore, for a large network ($x \gg \xi$), it can be assumed that velocity variation across a single mesh ($\xi\dot{\varepsilon}$) is rather small compared to the average velocity of the cross ($x\dot{\varepsilon}$).

The normalized drag force per unit length, per unit velocity for a single bead is equal to 3π (dash-dotted red line in Fig. 5-3 based on $\mathrm{F} = 3\pi(2a)\eta U$ (η: viscosity, U: velocity, a: filament radius). The 3D-cross can be discretized into beads (Fig. 5-16-c), and in the absence of hydrodynamic interactions between beads, the force required to move it would be equal to $\mathrm{F}_{\mathrm{Bead\ w/o\ HI}} = 3\pi(3\xi - 2\times 2a)\eta U \cong 3\pi(3\xi)\eta U$. On the other hand, if we break the 3D-cross to three rods, then in the absence of hydrodynamic interactions between rods, a force $\mathrm{F}_{\mathrm{Rod\ w/o\ HI}} \cong (2\mathrm{C}_{\perp} + \mathrm{C}_{\parallel})\xi\eta U$ is required to move it. Values for $\mathrm{C}_{\perp}$ and $\mathrm{C}_{\parallel}$ are depicted in Fig. 5-3 (blue lines).

Using ξ value (0.3 μm for 1 mg/ml actin used here) and exact bead equations with hydrodynamic interactions, we can evaluate above equations to arrive at $\frac{\mathrm{F}_{\mathrm{Rod\ w/o\ HI}}}{\mathrm{F}_{\mathrm{Bead\ with\ HI}}} = 1.6$ (based on $\mathrm{C}_{\perp} \cong 2.73$ and $\mathrm{C}_{\parallel} \cong 1.73$). Similar to Fig. 5-14, ignoring hydrodynamic interactions between rod segments leads to erroneous drag (1.6-fold overestimation). If we compare rod case with when we ignore hydrodynamic interactions between beads, we observe that overestimation errors are higher for beads, $\frac{\mathrm{F}_{\mathrm{Bead\ w/o\ HI}}}{\mathrm{F}_{\mathrm{Bead\ with\ HI}}} = 6.5$. Hence, we can conclude that overestimation errors are mostly due to hydrodynamic interactions within beads composing each rod ($\frac{3\pi}{\mathrm{C}_{\perp}} \cong 3.45$ and $\frac{3\pi}{\mathrm{C}_{\parallel}} \cong 5.45$). Comparing this model 3D-cross with simulation of Fig. 5-15, we can speculate that observed overestimation is mostly due to *local* hydrodynamic interactions (i.e., hydrodynamic interactions within a volume size of ξ^3) accounting for 6.5-fold out of 20-fold, and the remaining 3-fold overestimation is due to distant elements or potentially the finite variable size of the system.

This 3D-cross model also provides intuitive idea about superimposition of hydrodynamic interactions due to filaments with different orientations. For an isolated filament, $\frac{3\pi}{\mathrm{C}_{\perp}}$ and $\frac{3\pi}{\mathrm{C}_{\parallel}}$ are factors describing *average* drag reduction due to hydrodynamic interactions within each rod. For the central bead in Fig. 5-16-c, we can envision that screening from filaments at three perpendicular orientations superimpose to reduce its drag approximately by factor $\left(\frac{3\pi}{C_\perp}\right)^2 \frac{3\pi}{C_\parallel} \cong$ 65.1. Accurate bead equations (same as $F_{\text{Bead with HI}}$ discussed above) lead to the factor 80.2, which is higher because drag force across filament is not uniform. The central parts receive lower drag forces and hence have more drag reduction (blue line Fig. 5-4-b for local drag force).

While for the net force to move all the 3D-cross we have $\frac{F_{\text{Bead w/o HI}}}{F_{\text{Bead with HI}}} = 6.5$, for its central bead we have $\frac{3\pi(2a)\eta U}{F_{\text{Center with HI}}} \cong 80.2$. Clearly, not all the beads can receive as much screening as this central bead, hence this factor of 80.2 can be thought of as a generous upper-estimate. On the other hand, looking at the full network, the end points of this cross, which receive the highest drag, are not completely isolated and their drag would be lower than what is predicted here (i.e., they themselves are in the middle of a segment). Consequently the factor 6.5 can be interpreted as a mean lower-estimate. Our 20-fold factor in Fig. 5-15 falls between these lower and upper bounds suggested here ($\frac{3\pi}{C_\parallel}, \frac{3\pi}{C_\perp} < 20 < \left(\frac{3\pi}{C_\perp}\right)^2 \frac{3\pi}{C_\parallel}$). However, care has to be taken in using the suggested model because the key variable in Fig. 5-15 is system size, which is not incorporated here. Furthermore, the model in Fig. 5-15 varies in other aspects such as being composed of a non-regular network. Nonetheless, it is still interesting that with only application of rod and bead drag formulae, we can find bounds that contain overestimation factor predicted from that complex model. It is possible that simulations with larger systems sizes cover the entire range presented here.

5.4.4 Hydrodynamic Interactions and System-Size Dependent Viscoelastic Shear Loss Moduli

It is evident from Fig. 5-15 that in the absence of HIs, friction between network and solvent constantly increases as a function of system size (S). In fact, overall stress due to that friction is proportional to the square of the system-size for a homogenous network deformed uniformly:

$$\sigma = \frac{F}{A} = \frac{\int dF}{S^2} \propto \frac{\int_0^S A\, x\dot{\varepsilon} dx}{S^2} \propto S^2 \dot{\varepsilon} \qquad \text{Eq. (5-6)}$$

As a result, the loss modulus in the absence of HIs follows G" $\propto S^2$ behavior (for a sufficiently large S such that homogeneity approximation is not violated). This can be verified in Fig. 5-15 for $S > 0.9\,\mu m$ (i.e., $S/\xi > 3$), where the logarithmic plot demonstrates a perfect linear form. Although, Fig. 5-15 is for the bead model without HIs, but Eq. 5-6 can be extended to a rod model without HIs as well. Hence, we conclude, that a model without HIs will significantly overestimate the frictional forces and the resulting G" or E" value.

On the other hand according to Fig. 5-15, beyond $1\,\mu m$, including HIs result in a fairly constant dissipative shear power as well as nearly constant G" in agreement with experimental observation for 1P (one particle) microrheology. Consequently, while excluding HI effects results in a sever size dependency (in conflict with out intuitions), including them results in an almost constant value that increases slightly with system size. This slow increase has the potential to clarify the mismatches observed between micro and macro measurements of viscoelastic moduli. While most studies cover frequency dependent behavior of actin viscoelastic properties, to the best of our knowledge, no study has yet discussed the system/sample size dependency of G" (*loss* modulus) for actin networks.

2P (two particles) microrheology probes viscoelastic moduli at $100\,\mu m$ length scale and its results are consistent with bulk rheology (probed with rheometer at a $160-\mu m$ gap size as the dominant length scale)[143]. This suggests that variation of G" with system size will asymptote around $100\,\mu m$ length scale. Consequently, we need further studies to extend the system size beyond current limit ($2\,\mu m$) to relate micro-size data to macro-size data. Rod model can help us to increase the system size by up to an order of the magnitude.

Nonetheless, analyzing a system with infinite size might not be possible. Analytically, Reynolds number of such a system is infinity, and hence, Stokes regime does not apply to it. For example, analytical solution of Stokes equation for a cylinder with infinite size results in a zero drag (it imposes a uniform velocity across fluid equal to the cylinder velocity). This is called Stokes paradox and is due to a logarithmic singularity by ignoring inertial terms in Navier-Stokes equations[165,166].

Similarly, it is hard to experimentally measure viscoelastic properties for a large system. In such a system, momentum diffusion of solvent as well as wave propagation in the network are slower than shear plate oscillations (ω). Consequently, deformation is not affine and we cannot simply relate sensor force to a known average deformation. In fact, even for systems with finite size, interplay between momentum diffusion, wave propagation, and network-solvent friction can result in complex deformation patterns (e.g., see Fu *et al.* FIG. 2-b[167]). Additionally, purified proteins are expensive and are not available in large quantities.

Nonetheless, experiments probing nm to mm system sizes have proved that viscoelastic moduli vary at different length scales, consistent with our predictions. Next, we review some of those experiments. According to Tassieri *et al.*[110], microrheological measurements of viscoelastic moduli can match the scaling laws found by macroscopic rheology, while disagreeing by a constant factor in absolute magnitude. Further deviations can arise if the probe size or surface chemistry does not match the network.

Gardel *et al.* used 2P microrheology to probe the contributions of large length scale fluctuations to G', and 1P microrheology to isolate the contributions of fluctuations at short length scales[143]. In their measurements reprinted in Fig. 5-17, values of G" from 1P and 2P microrheology are always lower than bulk values. However, while 2P values are slightly smaller than bulk values, 1P microrheology results are abruptly lower by a factor of 10 in 1.0 mg/ml F-actin (entangled but not crosslinked). They also reported that 1P and 2P microrheology measured the same plateau elasticity (G' , elastic moduli, at low frequencies). However, they differ in higher frequencies due to longitudinal fluctuations diffusing in the length scale of the persistence length. Unfortunately, they do not discuss the differences in the G" value. Though, they state that in the cytoskeleton, as a result of crosslinking, these longitudinal fluctuations are less important, and hence, 1P results are closer to bulk rheology. In fact, according to Luan *et al.* the ratio of *plateau* modulus between macro and micro measurements varies from 4 for low concentration of crosslinkers to 2.5 for entangled F-actin to 1 for high concentration of crosslinkers[160].

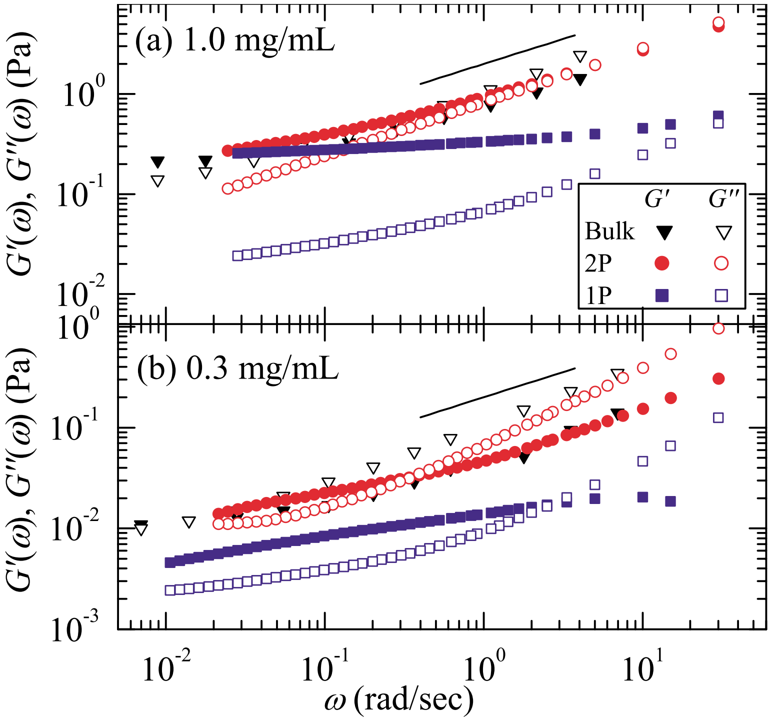

Figure 5-17: Viscoelastic moduli of F-actin at (a) 1.0 mg/ml, and (b): 0.3 mg/ml concentrations compared between 1P, 2P and bulk rheology. Bead radius: $0.42\ \mu m$. Picture is taken from Garden *et al.*[143].

Liu *et al.*[156] observed a similar pattern as Garden *et al.*[143] for different filament lenghts as depicted in Fig. 5-18. They noticed that for larger filament sizes (but the same concentration), the differences between 1P data and 2P data are higher. Surprisingly, incease in moduli due to ignoring HIs, and its decrease by considering only local particles (contained in the microscopic simulation box) can cancel each other. This cancellation means that Brownian dyanmics (BD) simulations can ignore HIs, and yet achieve a reasonable macroscopic data. Nontheless, this approach cannot be considered as a safe and rigorous techniques and might fail as cocentration varies.

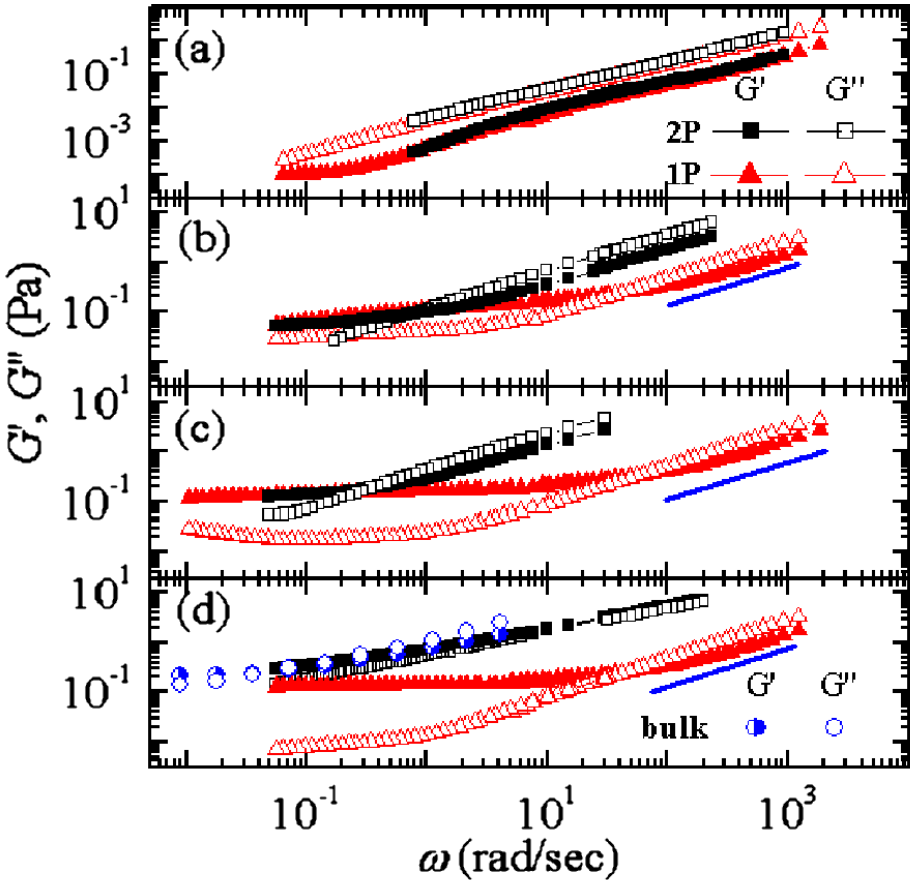

Figure 5-18: Viscoelastic moduli of F-actin at 1.0 mg/ml concentrations compared between 1P, 2P and bulk rheology for varying filament (contour) lengths: (a): $0.5\ \mu m$, (b): $2\ \mu m$, (c): $5\ \mu m$, (d): $17\ \mu m$. Bead radius: $0.42\ \mu m$. Picture is taken from Liu *et al.*[156]. Solid blue line represents $\omega^{3/4}$ scaling.

Actin crosslinked networks can present the same pattern as entangled actin in elasticity modulus versus size, but for the loss modulus the value for 1P (micro scale) can be higher! This is not yet noted or explained. As depicted in Fig 5-19, Lieleg *et al.* collected microscopic and macroscopic viscoelastic moduli of rigor HMM crosslinked actin networks in the 0.002 to 50 Hz range[142]. The macroscopic elastic modulus, G', is consistently higher across all ranges. On the other hand, the macroscopic viscous modulus, G", is lower approximately by a factor of 2 for frequencies higher than 0.03 Hz. Lower frequencies have a complicated behavior due to crosslinker dissociation.

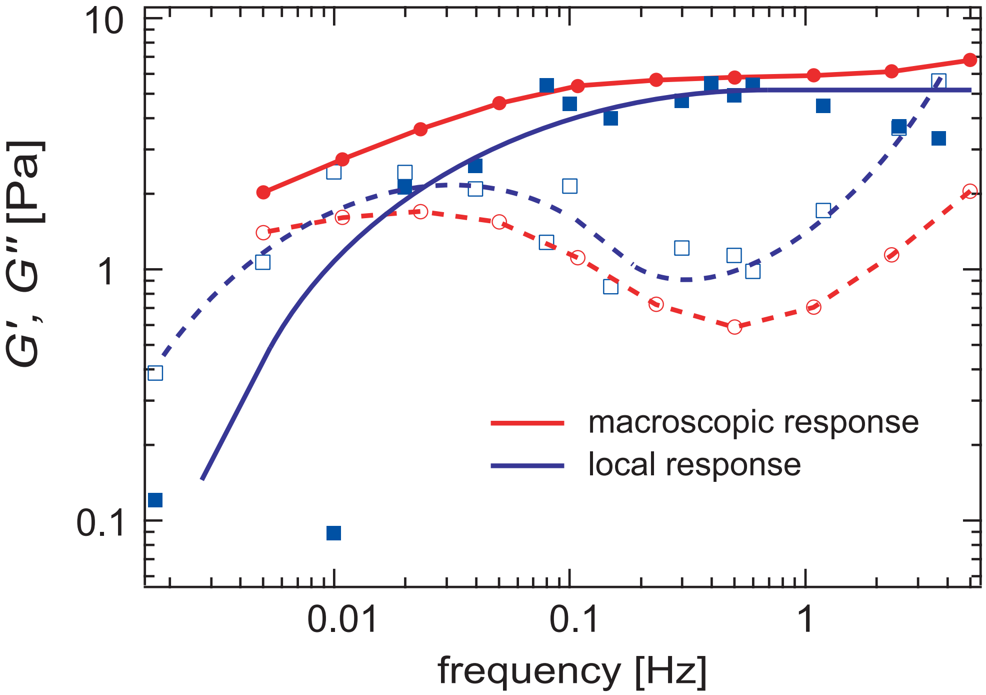

Figure 5-19: Viscoelastic moduli of F-actin transiently crosslinked with Rigor HMM compared between micro and macro rheology. Bead radius: $\mathbf{0.42}\ \boldsymbol{\mu m}$. Picture is taken from Lieleg *et al.* supplemental material[142].

Viscoelastic moduli of Bacteriophage fd, as a model semiflexible filament, was measured by rotating disk and magnetic beads rheometry at different concentrations. In all cases, macroscopic measures reported higher values[168]. Another study recently reported that for gel-forming aqueous dispersion of Laponite® clay[169], macroscopic viscoelastic moduli can be up to two orders of the magnitude higher than microscopic ones[170].

In summary, HIs are required to arrive at a reasonable loss moduli. Otherwise, the loss moduli will be surprisingly high and strongly dependent on the system size. On the other hand, with inclusion of HIs, loss moduli seem to reach to an asymptotic behavior or follow a subtle increase. This increase can potentially describe why typically macro viscoelasticity measurements report higher values than micro measurements. Nonetheless, while there are some explanations about this difference in the elastic moduli, the loss moduli difference is more complex and not yet understood. We hope to resolve this mystery by improving our understanding about the frictional forces transmitted between the solvent and the network. This study can be a stepping-stone toward that goal.

Chapter 6: Summary and Conclusions

6.1 Registration and Inverse Elasticity for Cardiovascular Diagnosis

Compared to the breast or prostate cancer elastography, cardiovascular elastography is more challenging mainly due to the complexity of typical lesions. A typical atherosclerotic plaque can contain multiple inclusions with varying sizes, geometries, and compositions spanning four orders of magnitude in elastic moduli.

The conventional IVUS (IntraVascular UltraSound) elastography deals only with radial strain measurements and registers only the radial or in-depth motion[171,172]. The conventional elastography techniques are developed for ultrasound and unfortunately while OCT (Optical Coherence Tomography) is the optical analog to the B-mode ultrasound, they cannot be successfully applied to the OCT elastography[97,98]. Consequently, we tried to develop new elastography techniques applicable to OCT. Compared to IVUS, catheter-based OCT generates high-resolution images at the cost of lower imaging depth and is capable of identifying arterial tissue types directly[173]. Furthermore, inter-frame registration is more challenging for OCT due to far lower speckle decorrelation time, as well as higher strain-induced decorrelation. We worked on low strain regime (i.e., close consecutive frames) for which strain-induced decorrelation is small. Furthermore, for small deformations, a linear isotropic relationship is a well-accepted approximation. Most tissues are not indeed isotropic, but equivalent parameters can be defined for in-plane deformation.

Ideally to compute the image similarity, we need to know the displacement field of the entire sample frame. Then, we can interpolate back a corresponding image at the reference position to compare it with the reference frame. However, a typical image has about 10^5 pixels, and interpolating for those data points is expensive. Instead, we noted that sub-blocks locally move in a rigid manner, and consequently, we can easily match points between reference and sample image just by knowing the motion of the sub-block center. Note that this approximation is violated, if we have considerable amount of rotation/distortion, high levels of strain (compared to the ratio of the pixel to the block size) and strain induced speckle decorrelation.

We developed effective initialization and regularization techniques for motion estimation, elastography, and modulus imaging. We showed that while these techniques can suppress the noise, they also recover a considerable portion of the original strain signal (having high SNR: signal to noise ratio).

Our approach seeks to optimize the quality of image registration within a single IREP (Inverse and Registration Elasticity Problem) step. It is vitally important to initialize these high-dimensional optimization problems properly, and hence, we utilized several simpler techniques such as REP (Registration Elasticity Problem) for robust initialization of IREP. While our techniques have been developed to generate robust solutions to the IEP (Inverse Elasticity Problem) in elastography of human tissues, they have broader applications in solving of general registration problems commonly encountered in many fields.

Our initial *in vitro* results seem promising. However, future studies are required for further quantification of accuracy and determination of measurement limits. Those studies can also correlate elastograms and modulus data with histologically-derived measures of plaque vulnerability. We have verified our methods with ultrasound images, and we recently used carotid images taken by CARS (Coherent AntiStokes Raman Spectroscopy) modality[103]. Based on C-H bounds, CARS can distinguish between different lipid structures, and we used this extra information to examine elasticity of different lipid forms in arteries, namely lipid pools and needle/plate-shaped lipid crystals. Tested by ultrasound, OCT, and CARS, we expect our methods to be applicable to other generic imaging modalities as well.

Nonetheless, there are several challenges in deployment of this system for *in vivo* catheter-based imaging. Of major concern is the additional decorrelation noise from catheter motion. However, this extra decorrelation might be resolved by application of frequency domain OCT[174-176], which has higher temporal frame rates. We have to be also careful to avoid optical aberrations affecting image magnification. Varying magnification at different location can introduce artificial strains and interfere with the registration and the inverse elasticity solutions.

Future Directions

Methodology) The image similarity measure can be made more accurate by altering block matching to overall image matching (performed by interpolating the second frame to the reference position). Additionally, overall image matching will make the model more compatible with large deformations/rotations. Furthermore, we can image a 3D grid to compensate for aberrations in the image. Similarly, with the advance of PSF-based (PSF: point spread function) image correction techniques, we can achieve sharper images to improve the segmentation and registration. Moreover, here we compared only two frames, but if we compare several consecutive frames (similar to our nonlinear elasticity study[72]), we can better suppress the imaging errors and noises.

Application) This method can be applied to other modalities, such as frequency domain OCT, CARS, ultrasound, MRI, or even fluorescence microscopy. Addition of a growth term will make this method as an ideal candidate for the developmental biology, where we look at the collective migration of cells and their growth. This study focused on developing the method and examining its *in vitro* feasibility. Future studies are required to further quantify the accuracy, especially for *in vivo* application with catheters.

6.2 Hydrodynamic Interactions in Cytoskeletal Mechanics and a New Rod Method

We showed that hydrodynamic interactions (HIs) significantly alter the viscous forces required to deform and ultimately remodel actin networks. Our observation is consistent with recent suggestions that crowding and hydrodynamic interactions likely dominate *in vivo* macromolecular motion[162]. We showed that HIs among elements of the actin network can alter their dynamics by at least 2-20 fold at different levels of network structure.

Future studies are required to understand HI effects at larger length scales. However, our proposed rod method opens the door for simulation of systems with larger size. We have shown that with a negligible 5% error, this rod method can reduce the computational cost and memory requirement by 5 orders of the magnitude. Currently, the limiting factor in modeling larger systems is the prohibitive memory and computing resource requirement of the bead methods. On the other hand, conventional rod methods are complicated and cannot be adopted by most biologists. However, in our rod HI method, the HI formulation is exactly similar to the HI formulation for the beads, and the only differences are in the input Stokes radius and the drag coefficients used for beads. Consequently, codes developed for bead HI calculation can easily adopt our rod HI formulation and use it to extend the limit on the system size they investigate.

In a more detailed summary, in Chapter 4, we began by introducing the concept of the hydrodynamic interactions. We presented the standard bead method, based on discretizing filaments into side-by-side stacked spherical beads. We used Rotne-Prager tensor for hydrodynamic interactions and briefly reviewed other tensor forms. We found that Oseen tensor and Rotne-Prager tensor performed better than the spherical bead tensor, but overall, only Rotne-Prager performed satisfactory at all cases.

We covered various methods to compensate for the discretization errors due to geometrical difference between stacked spheres and a cylinder. Each method is typically adjusted toward either long aspect ratio or high aspect ratio filaments. Furthermore, each method is usually good only for axial motion or lateral motion. However, we introduced an optimal bead method, where instead of spherical beads, we use disk-shaped beads to build an exact cylindrical filament. Our optimal bead method performs well in low/high aspect ratio as well as axial/lateral motion.

Subsequently, we introduced the Swanson-Batchelor formulation to calculate the drag coefficients of filament at both large and small aspect ratios. Based on Swanson-Batchelor formulation, we can rely on accurate rod data and avoid the rod to bead discretization error, if the filament length is not an integer multiple of the filament radius. We examined almost all experimental/theoretical data in the drag coefficient of straight filaments and hand picked the Swanson formulation for low aspect ratio and the Batchelor formulation for the high aspect ratio. This combination provides us with a sweet spot for accuracy, simplicity, and consistency (between high and low aspect ratio or lateral and axial). Based on comparing different experimental/theoretical data for drag coefficients, we also found that those data have up to 5% uncertainly. Hence, any effort to calculate HIs and match drag data with less than %5 error is over fitting. Accordingly, when we discretize a filament into rod segments, the number of segments can be based such that the error in the drag coefficients is less than 5%.

Next, we developed a new simplified rod method to account for HIs. The method uses Swanson-Batchelor formulation, together with Rotne-Prager tensor to calculate HIs between rod segments. We further quantified accuracy of this method and examined different candidates for its Stokes radius. It turns out that effective volumetric radius, 2D/3D hydrodynamic radius, or filament radius all perform well as candidates of the Stokes radius in our rod method. Further studies are required to distinguish between these candidates.

The standard bead method and our new rod method are used in Chapter 5 for analysis of HI effects in the mechanics of the cytoskeleton. The method has two main advantages. Firstly, it can be used for systems with larger size, due to superbly lower required computational resource. Secondly, it is simple and similar to the bead method. Hence, our rod method can be adopted by groups already using bead methods, or biologists despising the messy mathematics of the conventional rod HI methods.

In Chapter 5, we began by introducing the F-actin structure and its prominent role in cell mechanics. Next, we focused on the role of HIs on altering actin mechanics and dynamics at different length scales and structural levels. We began by looking at the role of HIs at a single filament level in rigid body motion and diffusion, as well as filament lateral fluctuations. We found that ignoring the HIs between mesh-sized rod segments (300 nm for 1 mg/ml F-actin) can result in up to 7-fold error in the drag coefficients of the filament. Consequently, we can have up to 7-fold error in the diffusion rates of the filament or its overall rigid body movements if we ignore HIs.

We specifically investigated how HIs can alter mode shapes or relaxation times. Relaxation times of filaments are directly related to the viscoelastic properties of the macroscopic network. Typically, in filament bending equation a uniform drag coefficient is presumed based on rigid body lateral translation. The bending equation assumes that local filament velocity and force are proportional, and therefore, ignores HIs between different locations of the filament.

We calculated force distribution across filament for each mode. Based on a normalized cross correlation of force and mode shape, we found that for each mode typically at least 95% of the hydrodynamic force power lies in the same mode, meaning that mode shapes are not affected by HIs. This also means that local force and local velocity are approximately proportional with a root mean squared error of 30%.

However, effective drag coefficients of modes are higher than the presumed value. For example, for a 300 nm filament, the relaxation time of the first mode is approximately two times the value predicted in the absence of HIs. Relaxation times of other modes are even more underestimated if we ignore HIs. Consequently, our data reflects that higher modes have higher effective drag coefficients, consistent with experimental observation in actin and microtubules. Those observations were speculated to be due to an unknown internal viscosity, and instead, we suggest a simpler rigorous explanation. Similarly, Sedeh *et al.* [116] have calculated the Langevin normal modes and diffusion coefficients of (actin) proteins using the finite element method. They observed that HIs have a prominent role in those values. In fact, they reported that proteins have to be embedded in a chamber at least 400 times larger than protein size to overcome the HIs between walls and the protein (see their Fig. 2-4 for details).

At the next structural level, we examined the effects of His in the alignment process of two actin filaments during bundle formation. We studied acto-myosin alignment for antiparallel filaments and crossed parallel filaments. We also studied zipper action for aligning crossed filaments by invoking passive crosslinkers like α-actinin. In this part, HI effects were quantified based on how forces to move the filament change, if we ignore HIs. We found that for acto-myosin or α-actinin the forces can be altered by 35% or 120% respectively. Smaller crosslinkers are present for filaments closer to each other, and hence, enhance the role of HIs. We also confirmed our rod method, against bead method in this study. Using the rod method, the computational cost can be decreased by up to 5 orders of the magnitude for only 5% error.

In alignment studies, we also found that HIs for distant parts of the filament are negligible. In other words, each filament only interacts approximately with the parts of the other filament that are within the same distance as the distance between filaments[6]. Alternatively, we can state that screening length for HIs scales with the filament distance. This study also compared and supported our rod method, which is based on modeling HIs similarly between rods and isotropic beads.

---

[6] Note that distance between two filaments is different than distance between a point on filament one, to a point on filament two.

Finally, we focused on the role of HIs in the network level. We began by examining a regular 1D network. We showed that given a constant strain rate, the viscous force alters in the section depth. Consequently, a poroelastic model is more compatible with HI effects. We also realized that in a network, the HIs between nearby segments are greater than HIs between different locations of the same filament. In fact, this means that even if we break our filaments into rod segments (as opposed to bead discretization), we cannot yet ignore HIs.

Next, we modeled a random 3D actin network with the relevant physiological concentration of 1 mg/ml ($\cong 24\ \mu\text{M}$ converted to molar based on Mason *et al.*[157], consistent with 43kDa mass of actin). In this part, we measured the viscoelastic loss modulus as a function of system size and matched it against experimental data. We observed that a loss modulus for viscoelastic behavior could be defined in the shear mode, but not in the axial mode. We showed that HIs result in a system-size dependent loss modulus, and hence, we require further studies at larger length scales (where we might apply our rod method). Nonetheless, ignoring HIs between network beads can result in a substantial, about 20 fold, error in loss modulus. Indeed, in contrary to the reasoning that HIs are small because F-actin only occupies 0.1% of the volume, HIs are superbly large.

Finally, we introduced a 3D cross as the basic unit to build regular 3D networks. The drag coefficients of the mesh-sized segments in the 3D cross can be used to calculate simple estimates on how loss modulus might be affected by HIs in a random 3D network.

In conclusion, we have developed a simple rod method that mimics the ingenuous formulation of the bead method, but yet accurately accounts for HIs between rod segments. This method can have applications far beyond just cellular mechanics, can substantially decrease the computational cost of HIs, and can enable us to include HIs for more complex and larger systems. We have also established that HIs significantly affect actin dynamics, and hence, they cannot be neglected in the cytoskeleton modeling or interpreting experimental data about actin dynamics. HI effects start in the single filament level, but are magnified further in the network level, altering actin dynamics by more than an order of the magnitude.

Future Directions

General Applications. With further analysis, we might find a better candidate for the Stokes radius of our rod method. This method is a simple model that can be integrated in other Brownian dynamic packages for different problems, especially those with larger sizes. More specifically, we intend to use it for the analysis of the transport and diffusion inside the nuclear pore complex. There is not a clear understanding of how transport in nanopores might be affected by the enormous number of peptide polymer filaments that coat the walls and occlude the passage[177-179]. The hydrodynamic interactions among those protein filaments cannot be modeled by bead method (due to problem-size limit). However, the rod method can include HIs to calculate the diffusion inside the pore, especially for the filamentous geometry of DNAs used in gene delivery.

Actin Mechanics. Relaxation times of higher mode are different from those suggested by the tube model. Experimental data on fluctuations of isolated F-actins can determine whether they are due to HIs or due the internal viscosity. In addition, we can use the rod method to extend the loss modulus analysis to the larger system sizes. Our studies were based solely on viscous forces at a single time snapshot. The HIs model can be joined with a model taking into account elasticity and thermal forces, to examine the behavior of actin networks at longer time scale. Moreover, recently a collective steady state motion was observed for actin filaments in myosin motility assays[106,180-182]. It is speculated that this pattern formation is due to HIs. However, we can use our rod method to examine this claim and investigate the role of HIs in another level of active actin structures.

Appendix

Attached CD contains all related codes for:

1. Inverse and Registration Elasticity Problem, including the custom-built FEM core and related scripts in both Matlab and C++. I have also included FFT library and related Matlab libraries for completeness. Every time Matlab is updated, the libraries should also be checked for compatibility and correct dynamic links (dl).

2. Matlab code for Hydrodynamic Interaction of bead/rod models and specific scripts for analyzing the role of Hydrodynamic Interactions in Actin's Dynamic.

Bibliography

1. Roger VL, Go AS, Lloyd-Jones DM, Adams RJ, Berry JD, et al. (2011) Heart disease and stroke statistics--2011 update: a report from the American Heart Association. Circulation 123: e18–e209. doi:10.1161/CIR.0b013e3182009701.

2. Hansson GK, Robertson A-KL, Söderberg-Nauclér C (2006) Inflammation and Atherosclerosis. Annu Rev Pathol Mech Dis 1: 297–329. doi:doi: 10.1146/annurev.pathol.1.110304.100100.

3. Jones DW, Chambless MLE, Folsom PAR, Heiss MG, Hutchinson MRG, et al. (2002) Risk Factors for Coronary Heart Disease in African Americans: 1–7.

4. Association AH (2003) Heart and Stroke Facts, American Heart Association: 1–80.

5. Libby P (2002) Inflammation in atherosclerosis. Nature 420: 868–874. doi:10.1038/nature01323.

6. Steinberg D (1989) The cholesterol controversy is over. Why did it take so long? Circulation 80: 1070–1078.

7. Munro JM, Cotran RS (1988) The pathogenesis of atherosclerosis: atherogenesis and inflammation. Lab Invest 58: 249–261.

8. Libby P, Ridker PM, Maseri A (2002) Inflammation and atherosclerosis. Circulation 105: 1135–1143.

9. Berliner JA, Navab M, Fogelman AM, Frank JS, Demer LL, et al. (1995) Atherosclerosis: basic mechanisms. Oxidation, inflammation, and genetics. Circulation 91: 2488–2496.

10. Epstein FH, Ross R (1999) Atherosclerosis—an inflammatory disease. N Engl J Med 340: 115–126.

11. Springer T, Cybulsky M (1996) Traffic signals on endothelium for leukocytes in health, inflammation, and atherosclerosis. Atherosclerosis and coronary artery Disease.

12. Steinberg D (2002) Atherogenesis in perspective: hypercholesterolemia and inflammation as partners in crime. Nat Med 8: 1211–1217. doi:10.1038/nm1102-1211.

13. Ridker PM (2003) High-sensitivity C-reactive protein and cardiovascular risk: rationale for screening and

primary prevention. Am J Cardiol 92: 17K–22K.

14. Goldschmidt-Clermont PJ, Creager MA, Losordo DW, Lorsordo DW, Lam GKW, et al. (2005) Atherosclerosis 2005: recent discoveries and novel hypotheses. Circulation 112: 3348–3353. doi:10.1161/CIRCULATIONAHA.105.577460.

15. Libby P (2006) Inflammation and cardiovascular disease mechanisms. American Journal of Clinical Nutrition. Vol. 83. pp. 456S–460S.

16. Tuzcu EM, Kapadia SR, Tutar E, Ziada KM, Hobbs RE, et al. (2001) High prevalence of coronary atherosclerosis in asymptomatic teenagers and young adults: evidence from intravascular ultrasound. Circulation 103: 2705–2710.

17. Hackett D, Davies G, Maseri A (1988) Pre-existing coronary stenoses in patients with first myocardial infarction are not necessarily severe. Eur Heart J 9: 1317–1323.

18. Glagov S, Weisenberg E, Zarins CK, Stankunavicius R, Kolettis GJ (1987) Compensatory enlargement of human atherosclerotic coronary arteries. N Engl J Med 316: 1371–1375. doi:10.1056/NEJM198705283162204.

19. Libby P, Theroux P (2005) Pathophysiology of coronary artery disease. Circulation 111: 3481–3488. doi:10.1161/CIRCULATIONAHA.105.537878.

20. Slager C, Wentzel J, Gijsen F, Thury A, van der Wal A, et al. (2005) The role of shear stress in the destabilization of vulnerable plaques and related therapeutic implications. Nat Clin Pract Cardiovasc Med 2: 456–464. doi:10.1038/ncpcardio0298.

21. Texon M (1957) A hemodynamic concept of atherosclerosis, with particular reference to coronary occlusion. AMA Arch Intern Med 99: 418–427.

22. Glagov S, Rowley DA, Kohut RI (1961) Atherosclerosis of human aorta and its coronary and renal arteries. A consideration of some hemodynamic factors which may be related to the marked differences in atherosclerotic involvement of the coronary and renal arteries. Arch Pathol 72: 558–571.

23. Glagov S (1965) Hemodynamic factors in localisation of atherosclerosis. Acta Cardiol: Suppl 11:311.

24. Suzuki K (1967) Experimental studies on morphogenesis of arteriosclerosis, with special reference to relation between hemodynamic change and developments of cellulofibrous. Intimal thickening and atherosclerosis. Gunma J Med Sci 16: 185–243.

25. Palma EC (1973) Hemodynamic atherosclerosis. J Cardiovasc Surg (Torino) Spec No: 538–549.

26. Blackman BR, García-Cardeña G, Gimbrone MA (2002) A new in vitro model to evaluate differential responses of endothelial cells to simulated arterial shear stress waveforms. Journal of biomechanical

engineering 124: 397–407.

27. Cheng C, de Crom R, van Haperen R, Helderman F, Gourabi BM, et al. (2004) The Role of Shear Stress in Atherosclerosis: Action Through Gene Expression and Inflammation? CBB 41: 279–294. doi:10.1385/CBB:41:2:279.

28. Davies PF, Spaan JA, Krams R (2005) Shear Stress Biology of the Endothelium. Ann Biomed Eng 33: 1714–1718. doi:10.1007/s10439-005-8774-0.

29. Berger SA, Jou L-D (2000) Flows in Stenotic Vessels. Annu Rev Fluid Mech 32: 347–382. doi:10.1146/annurev.fluid.32.1.347.

30. Roach M, Smith N (1983) Does high shear stress induced by blood flow lead to atherosclerosis? Perspectives in biology and medicine 26: 287.

31. Cunningham KS, Gotlieb AI (2005) The role of shear stress in the pathogenesis of atherosclerosis. Lab Invest 85: 9–23. doi:10.1038/labinvest.3700215.

32. Awolesi MA, Sessa WC, Sumpio BE (1995) Cyclic strain upregulates nitric oxide synthase in cultured bovine aortic endothelial cells. J Clin Invest 96: 1449–1454. doi:10.1172/JCI118181.

33. Kakisis J, Liapis C, Sumpio B (2004) Effects of cyclic strain on vascular cells. Endothelium-J Endoth 11: 17–28.

34. Lee T, Sumpio B (2004) Cell signalling in vascular cells exposed to cyclic strain: the emerging role of protein phosphatases. Biotechnol Appl Bioc 39: 129–139.

35. Davies M (1995) Acute coronary thrombosis - The role of plaque disruption and its initiation and prevention. European Heart Journal. Vol. 16. pp. 3–7.

36. Rudd JHF, Davies JR, Weissberg PL (2005) Imaging of Atherosclerosis — Can We Predict Plaque Rupture? Trends in Cardiovascular Medicine 15: 17–24. doi:10.1016/j.tcm.2004.12.001.

37. Chau AH, Chan RC, Shishkov M, MacNeill B, Iftimia N, et al. (2004) Mechanical analysis of atherosclerotic plaques based on optical coherence tomography. Ann Biomed Eng 32: 1494–1503.

38. Holzapfel G, Sommer G, Regitnig P (2004) Anisotropic mechanical properties of tissue components in human atherosclerotic plaques. J Biomech Eng-T Asme 126: 657–665. doi:10.1115/1.1800557.

39. Williamson S, Lam Y, Younis H, Huang H, Patel S, et al. (2003) On the sensitivity of wall stresses in diseased arteries to variable material properties. J Biomech Eng-T Asme 125: 147–155. doi:10.1115/1.1537736.

40. Richardson P, Davies M, Born G (1989) Influence of Plaque Configuration and Stress-Distribution on

Fissuring of Coronary Atherosclerotic Plaques. Lancet 2: 941–944.

41. Li Z-Y, Howarth S, Trivedi RA, U-King-Im JM, Graves MJ, et al. (2006) Stress analysis of carotid plaque rupture based on in vivo high resolution MRI. Journal of biomechanics 39: 2611–2622. doi:10.1016/j.jbiomech.2005.08.022.

42. Tang D, Yang C, Zheng J, Woodard P, Saffitz J, et al. (2005) Local maximal stress hypothesis and computational plaque vulnerability index for atherosclerotic plaque assessment. Annals of Biomedical Engineering. Vol. 33. pp. 1789–1801. doi:10.1007/s10439-005-8267-1.

43. Tang D, Yang C, Zheng J, Woodard P, Saffitz J, et al. (2005) Quantifying effects of plaque structure and material properties on stress distributions in human atherosclerotic plaques using 3D FSI models. J Biomech Eng-T Asme 127: 1185–1194. doi:10.1115/1.2073668.

44. Loree HM, Kamm RD, Stringfellow RG, Lee RT (1992) Effects of fibrous cap thickness on peak circumferential stress in model atherosclerotic vessels. Circulation Research 71: 850–858.

45. Cheng GC, Loree HM, Kamm RD, Fishbein MC, Lee RT (1993) Distribution of circumferential stress in ruptured and stable atherosclerotic lesions. A structural analysis with histopathological correlation. Circulation 87: 1179–1187.

46. Lee RT, Grodzinsky AJ, Frank EH, Kamm RD, Schoen FJ (1991) Structure-dependent dynamic mechanical behavior of fibrous caps from human atherosclerotic plaques. Circulation 83: 1764–1770.

47. Richardson PD (2002) Biomechanics of plaque rupture: progress, problems, and new frontiers. Ann Biomed Eng 30: 524–536.

48. van der Wal A, Becker A (1999) Atherosclerotic plaque rupture - pathologic basis of plaque stability and instability. Cardiovasc Res 41: 334–344.

49. Mofrad MRK, Younis H, Patel S, Isasi A, Chung C, et al. (2003) Cyclic strain in human carotid bifurcation and its potential correlation to atherogenesis: Idealized and anatomically-realistic models. J Eng Math 47: 299–314.

50. Duck FA (1990) Physical Properties of Tissues - A Comprehensive Reference Book. Sheffield, United Kingdom: Academic Press. pp.

51. Sarvazyan A (1993) Shear acoustic properties of soft biological tissues in medical diagnostics. Proc Acoust Soc Am. Ottawa, Canada. p. 2329.

52. Loree HM, Tobias B, Gibson LJ, Kamm R, Small D, et al. (1994) Mechanical-Properties of Model Atherosclerotic Lesion Lipid Pools. Arterioscler Thromb 14: 230–234.

53. Ophir J, Cespedes I, Ponnekanti H, Yazdi Y, Li X (1991) Elastography - a Quantitative Method for

Imaging the Elasticity of Biological Tissues. Ultrason Imaging 13: 111–134.

54. Schaar JA, Mastik F, de Korte CL, Doyley MM, Cartier S, et al. (2001) Three dimensional palpography: a new tool for detection of vulnerable plaque, a feasibility and reproducibility in vitro. Eur Heart J 22: 506–506.

55. Schoenhagen P (2005) 3-D Intravascular ultrasound (IVUS) and IVUS-Palpography: insights into the mechanical behavior of the coronary vessel wall. Int J Cardiovasc Imaging: 1–3.

56. Ophir J, Kallel F, Varghese T, Bertrand M, Cespedes I, et al. (1997) Elastography: A systems approach. Int J Imag Syst Tech 8: 89–103.

57. Kallel F, Bertrand M (1996) Tissue elasticity reconstruction using linear perturbation method. IEEE Trans Med Imaging 15: 299–313. doi:10.1109/42.500139.

58. Raghavan KR, Yagle AE (1994) Forward and inverse problems in elasticity imaging of soft tissues. Nuclear Science, IEEE Transactions on 41: 1639–1648. doi:10.1109/23.322961.

59. Skovoroda AR, Emelianov S, LUBINSKI M, Sarvazyan A, O'Donnell M (1994) Theoretical-Analysis and Verification of Ultrasound Displacement and Strain Imaging. IEEE T Ultrason Ferr 41: 302–313.

60. Sumi C, Suzuki A, Nakayama K (1995) Estimation of shear modulus distribution in soft tissue from strain distribution. IEEE Trans Biomed Eng 42: 193–202. doi:10.1109/10.341832.

61. Cespedes I, Ophir J, Ponnekanti H, Maklad N (1993) Elastography - Elasticity Imaging Using Ultrasound with Application to Muscle and Breast in-Vivo. Ultrason Imaging 15: 73–88.

62. Chen EJ, Adler RS, Carson PL, Jenkins WK, O'Brien WD (1995) Ultrasound tissue displacement imaging with application to breast cancer. Ultrasound in Medicine & Biology 21: 1153–1162.

63. Sinkus R, Tanter M, Catheline S, Lorenzen J, Kuhl C, et al. (2005) Imaging anisotropic and viscous properties of breast tissue by magnetic resonance-elastography. Magn Reson Med 53: 372–387. doi:10.1002/mrm.20355.

64. Dresner MA, Rose GH, Rossman PJ, Muthupillai R, Ehman RL (1998) Magnetic resonance elastography of the prostate. Radiology 209P: 181–181.

65. Ophir J, Alam S, GARRA B, Kallel F, Konofagou EE, et al. (1999) Elastography: ultrasonic estimation and imaging of the elastic properties of tissues. P I Mech Eng H 213: 203–233.

66. Kemper J, Sinkus R, Lorenzen J, Nolte-Ernsting C, Stork A, et al. (2004) MR Elastography of the Prostate: Initial In-vivo Application. Rofo Fortschr Geb Rontgenstr N 176: 1094–1099. doi:10.1055/s-2004-813279.

67. Souchon R, Rouviere O, Gelet A, Detti V, Srinivasan S, et al. (2003) VISUALISATION OF HIFU LESIONS USING ELASTOGRAPHY OF THE HUMAN PROSTATE *IN VIVO:* PRELIMINARY RESULTS. Ultrasound in Medicine & Biology 29: 1007–1015. doi:10.1016/S0301-5629(03)00065-6.

68. ROWE P (1995) Magnetic-Resonance Elastography - a New Dimension for Mri. Mol Med Today 1: 395–395.

69. Fercher AF, Drexler W, Hitzenberger CK, Lasser T (2003) Optical coherence tomography-principles and applications. Reports on progress in physics 66: 239.

70. Sun C, Standish B, Yang VXD (2011) Optical coherence elastography: current status and future applications. J Biomed Opt 16: 043001. doi:10.1117/1.3560294.

71. Jang I-K, Tearney GJ, MacNeill B, Takano M, Moselewski F, et al. (2005) In vivo characterization of coronary atherosclerotic plaque by use of optical coherence tomography. Circulation 111: 1551–1555. doi:10.1161/01.CIR.0000159354.43778.69.

72. Karimi R, Zhu T, Bouma B, Mofrad MRK (2008) Estimation of Nonlinear Mechanical Properties of Vascular Tissues via Elastography. Cardiovascular Engineering 8: 191–202. doi:10.1007/s10558-008-9061-0.

73. Khalil AS, Bouma BE, Mofrad MRK (2006) A combined FEM/genetic algorithm for vascular soft tissue elasticity estimation. Cardiovasc Eng 6: 93–102. doi:10.1007/s10558-006-9013-5.

74. Kassab GS (2004) Y.C. “Bert” Fung: the father of modern biomechanics.

75. Fung Y-C (2010) Biomechanics: Circulation. Springer Verlag. p. Available:http://www.amazon.com/Biomechanics-Circulation-Y-C-Fung/dp/1441928421/ref=sr_1_5?ie=UTF8&qid=1323253070&sr=8-5.

76. Fung Y-C (1993) Biomechanics: Mechanical Properties of Living Tissues. 2nd ed. Springer. p.

77. Guccione JM, Kassab GS, Ratcliffe M (2010) Computational Cardiovascular Mechanics. Springer Verlag. p.

78. Gundiah N, Matthews PB, Karimi R, Azadani A, Guccione J, et al. (2008) Significant material property differences between the porcine ascending aorta and aortic sinuses. J Heart Valve Dis 17: 606–613.

79. Bathe K-J (1996) Finite element procedures.

80. Hughes TJR (2000) The finite element method. Dover Pubns. p.

81. Bonnet M, Constantinescu A (2005) Inverse problems in elasticity. Inverse Problems 21: R1–R50. doi:10.1088/0266-5611/21/2/R01.

82. Oberai A, Gokhale N (2003) Solution of inverse problems in elasticity imaging using the adjoint method. Inverse Problems.

83. Kallel F, Bertrand M (1995) Quantitative strain imaging and elasticity reconstruction. Engineering in Medicine and Biology Society, 1995., IEEE 17th Annual Conference. Vol. 1. pp. 629–630. doi:10.1109/IEMBS.1995.575284.

84. Souchon R, Srinivasan S, Varghese T (2002) Elastography: Imaging the elastic properties of soft tissues with ultrasound. J Med.

85. Righetti R (2004) The feasibility of using elastography for imaging the Poisson's ratio in porous media. Ultrasound in Medicine & Biology 30: 215–228. doi:10.1016/j.ultrasmedbio.2003.10.022.

86. Karimi R, Zhu T, Bouma BE, Mofrad MRK (2008) NIH VERSION: Estimation of nonlinear mechanical properties of vascular tissues via elastography. Cardiovasc Eng 8: 191–202. doi:10.1007/s10558-008-9061-0.

87. Barbone PE, Gokhale NH (2004) Elastic modulus imaging: on the uniqueness and nonuniqueness of the elastography inverse problem in two dimensions. Inverse Problems 20: 283–296. doi:10.1088/0266-5611/20/1/017.

88. Barbone PE, Bamber JC (2002) Quantitative elasticity imaging: what can and cannot be inferred from strain images. Phys Med Biol 47: 2147–2164.

89. Chan R, Chau A, Karl W, Nadkarni S, Khalil A, et al. (2004) OCT-based arterial elastography: robust estimation exploiting tissue biomechanics. Optics Express 12: 4558–4572.

90. Ibrahimbegović A (2009) Nonlinear solid mechanics. Springer Verlag. p.

91. Wu H-C (2005) Continuum mechanics and plasticity. CRC Press. p.

92. Hayes MA, Saccomandi G, Sciences ICFM (2001) Topics in finite elasticity. Springer Verlag Wien. p.

93. Khalil AS, Chan RC, Chau AH, Bouma BE, Mofrad MRK (2005) Tissue Elasticity Estimation with Optical Coherence Elastography: Toward Mechanical Characterization of In Vivo Soft Tissue. Ann Biomed Eng 33: 1631–1639. doi:10.1007/s10439-005-6766-3.

94. Oberai AA, Gokhale NH, Doyley MM, Bamber JC (2004) Evaluation of the adjoint equation based algorithm for elasticity imaging. Phys Med Biol 49: 2955–2974. doi:10.1088/0031-9155/49/13/013.

95. Zienkiewicz OC, Taylor RL, Taylor RL, Zhu JZ (2005) The finite element method. Butterworth-Heinemann. p.

96. Taylor RL, Simo JC, Zienkiewicz OC, Chan ACH (1986) The patch test—a condition for assessing

FEM convergence. Int J Numer Meth Engng 22: 39–62. doi:10.1002/nme.1620220105.

97. Schmitt J (1998) OCT elastography: imaging microscopic deformation and strain of tissue. Optics Express 3: 199–211.

98. Rogowska J, Patel NA, Fujimoto JG, Brezinski ME (2004) Optical coherence tomographic elastography technique for measuring deformation and strain of atherosclerotic tissues. Heart 90: 556–562.

99. Varghese T, Bilgen M, Ophir J (1998) Multiresolution imaging in elastography. IEEE Trans Ultrason Ferroelectr Freq Control 45: 65–75. doi:10.1109/58.646912.

100. Gokhale N, Richards M, Oberai A, Barbone P, Doyley M (2004) Simultaneous elastic image registration and elastic modulus reconstruction. Biomedical Imaging: Nano to Macro, 2004 IEEE International Symposium on: 543–546. doi:10.1109/ISBI.2004.1398595.

101. Kybic J, Smutek D (2005) Computational elastography from standard ultrasound image sequences by global trust region optimization. Inf Process Med Imaging 19: 299–310.

102. Liu DC, Nocedal J (1989) On the limited memory BFGS method for large scale optimization. Mathematical programming 45: 503–528.

103. Kim S-H, Lee E-S, Lee JY, Lee ES, Lee B-S, et al. (2010) Multiplex coherent anti-stokes Raman spectroscopy images intact atheromatous lesions and concomitantly identifies distinct chemical profiles of atherosclerotic lipids. Circulation Research 106: 1332–1341. doi:10.1161/CIRCRESAHA.109.208678.

104. Karimi R, Chan R, Houser S, Bouma B, Mofrad MRK (2006) A novel framework for elastography and modulus estimation: integration of tissue mechanics with imaging. 2006 IEEE International Symposium on Biomedical Imaging: From Macro to Nano, Arlington, Virginia, USA IEEE: 602–605.

105. Adamczyk Z, Sadlej K, Wajnryb E, Ekiel-Jeżewska ML, Warszyński P (2010) Hydrodynamic radii and diffusion coefficients of particle aggregates derived from the bead model. Journal of Colloid and Interface Science 347: 192–201. doi:10.1016/j.jcis.2010.03.066.

106. Schaller V, Weber C, Frey E, Bausch AR (2011) Polar pattern formation: hydrodynamic coupling of driven filaments. Soft Matter 7: 3213. doi:10.1039/c0sm01063d.

107. Ardekani AM, Stocker R (2010) Stratlets: low Reynolds number point-force solutions in a stratified fluid. Phys Rev Lett 105: 084502.

108. Chandran P, Mofrad MRK (2009) Rods-on-string idealization captures semiflexible filament dynamics. Phys Rev E 79: 011906. doi:10.1103/PhysRevE.79.011906.

109. Chandran PL, Mofrad MRK (2010) Averaged implicit hydrodynamic model of semiflexible filaments. Phys Rev E 81: 031920. doi:10.1103/PhysRevE.81.031920.

110. Tassieri M, Evans R, Barbu-Tudoran L, Khaname G, Trinick J, et al. (2008) Dynamics of Semiflexible Polymer Solutions in the Highly Entangled Regime. Phys Rev Lett 101: 198301. doi:10.1103/PhysRevLett.101.198301.

111. Kim T, Hwang W, Lee H, Kamm RD (2009) Computational Analysis of Viscoelastic Properties of Crosslinked Actin Networks. PLoS Comput Biol 5: e1000439. doi:10.1371/journal.pcbi.1000439.t001.

112. Bernheim-Groswasser A, Shusterman R, Krichevsky O (2006) Fluorescence correlation spectroscopy analysis of segmental dynamics in actin filaments. J Chem Phys 125: 084903.

113. Bhattacharya S, Mishra C, Bhattacharya S (2010) Analysis of general creeping motion of a sphere inside a cylinder. J Fluid Mech 642: 295–328. doi:10.1017/S0022112009991789.

114. Bailey A, Lowe C, Pagonabarraga I, Lagomarsino M (2009) Accurate simulation dynamics of microscopic filaments using "caterpillar" Oseen hydrodynamics. Phys Rev E 80: 046707. doi:10.1103/PhysRevE.80.046707.

115. Yamakawa H (1970) Transport properties of polymer chains in dilute solution: Hydrodynamic interaction. J Chem Phys 53: 436.

116. Sedeh RS (2011) Contributions to the analysis of proteins. PhD Thesis MIT: 1–145.

117. Purcell E (1997) The efficiency of propulsion by a rotating flagellum. Proceedings of the National Academy of Sciences of the United States of America 94: 11307.

118. Saintillan D, Darve E, Shaqfeh ESG (2006) Hydrodynamic interactions in the induced-charge electrophoresis of colloidal rod dispersions. J Fluid Mech 563: 223. doi:10.1017/S0022112006001376.

119. Lettinga MP, Dhont JKG, Zhang Z, Messlinger S, Gompper G (2010) Hydrodynamic interactions in rod suspensions with orientational ordering. Soft Matter 6: 4556–4562. doi:10.1039/c0sm00081g.

120. Hsieh C, Larson R (2004) Modeling hydrodynamic interaction in Brownian dynamics: Simulations of extensional and shear flows of dilute solutions of high molecular weight polystyrene. Journal of Rheology 48: 995–1021. doi:10.1122/1.1781171.

121. Di Leonardo R, Cammarota E, Bolognesi G, Schäfer H, Steinhart M (2011) Three-Dimensional to Two-Dimensional Crossover in the Hydrodynamic Interactions between Micron-Scale Rods. Phys Rev Lett 107. doi:10.1103/PhysRevLett.107.044501.

122. Batchelor G (1970) Slender-body theory for particles of arbitrary cross-section in Stokes flow. J Fluid Mech 44: 419–440.

123. Swanson E, Teller D, de Haën C (1978) The low Reynolds number translational friction of ellipsoids, cylinders, dumbbells, and hollow spherical caps. Numerical testing of the validity of the modified Oseen

tensor in computing the friction of objects modeled as beads on a shell. J Chem Phys 68: 5097–5103.

124. Cox R (1970) The motion of long slender bodies in a viscous fluid Part 1. General theory. J Fluid Mech 44: 791–810.

125. Keller J, Rubinow S (1976) Slender-body theory for slow viscous flow. J Fluid Mech 75: 705–714.

126. RUSSEL WB, Hinch EJ, Leal LJ, TIEFFENBRUCK G (1977) Rods falling near a vertical wall. J Fluid Mech 83: 273–278.

127. Tirado MM, Martínez CL, la Torre de JG (1984) Comparison of theories for the translational and rotational diffusion coefficients of rod-like macromolecules. Application to short DNA fragments. J Chem Phys 81: 2047.

128. Broersma S (1981) Viscous force and torque constants for a cylinder. J Chem Phys 74: 6989. doi:doi:10.1063/1.441071.

129. Ui T, Hussey R, Roger R (1984) Stokes drag on a cylinder in axial motion. Phys Fluids 27: 787.

130. YOUNGREN G, ACRIVOS A (1975) Stokes Flow Past a Particle of Arbitrary Shape - Numerical-Method of Solution. J Fluid Mech 69: 377–403.

131. HEISS J, COULL J (1952) The Effect of Orientation and Shape on the Settling Velocity of Non-Isometric Particles in a Viscous Medium. Chem Eng Prog 48: 133–140.

132. Allison S, Pei H, Haynes M, Xin Y, Law L, et al. (2008) Translational Diffusion of Macromolecules and Nanoparticles Modeled as Non-overlapping Bead Arrays in an Effective Medium. J Phys Chem B 112: 5858–5866. doi:10.1021/jp710700n.

133. Gluckman M, Weinbaum S, PFEFFER R (1972) Axisymmetric slow viscous flow past an arbitrary convex body of revolution. J Fluid Mech 55: 677–709.

134. Pollard TD, Cooper JA (2009) Actin, a Central Player in Cell Shape and Movement. Science 326: 1208–1212. doi:10.1126/science.1175862.

135. Mofrad MRK (2009) Rheology of the Cytoskeleton. Annu Rev Fluid Mech 41: 433–453. doi:10.1146/annurev.fluid.010908.165236.

136. Nguyen L, Hirst L (2011) Polymorphism of highly cross-linked F-actin networks: Probing multiple length scales. Phys Rev E 83. doi:10.1103/PhysRevE.83.031910.

137. Lieleg O, Claessens MMAE, Bausch AR (2010) Structure and dynamics of cross-linked actin networks. Soft Matter 6: 218. doi:10.1039/b912163n.

138. Dominguez R, Holmes KC (2011) Actin Structure and Function. Annu Rev Biophys 40: 169–186.

doi:10.1111/j.1462-5822.2009.01378.x.

139. Svitkina TM, Verkhovsky AB, McQuade KM, Borisy GG (1997) Analysis of the actin–myosin II system in fish epidermal keratocytes: mechanism of cell body translocation. The Journal of Cell Biology 139: 397.

140. Hotulainen P, Lappalainen P (2006) Stress fibers are generated by two distinct actin assembly mechanisms in motile cells. J Cell Biol 173: 383–394. doi:10.1083/jcb.200511093.

141. Lieleg O, Kayser J, Brambilla G, Cipelletti L, Bausch AR (2011) Slow dynamics and internal stress relaxation in bundled cytoskeletal networks. Nature materials. doi:10.1038/nmat2939.

142. Lieleg O, Claessens MMAE, Luan Y, Bausch AR (2008) Transient Binding and Dissipation in Cross-Linked Actin Networks. Phys Rev Lett 101: 108101. doi:10.1103/PhysRevLett.101.108101.

143. Gardel M, Valentine M, Crocker J, Bausch AR, Weitz D (2003) Microrheology of Entangled F-Actin Solutions. Phys Rev Lett 91: 158302. doi:10.1103/PhysRevLett.91.158302.

144. Broedersz C, Depken M, Yao N, Pollak M, Weitz D, et al. (2010) Cross-Link-Governed Dynamics of Biopolymer Networks. Phys Rev Lett 105. doi:10.1103/PhysRevLett.105.238101.

145. Lieleg O, Schmoller K, Claessens MMAE, Bausch AR (2009) Cytoskeletal Polymer Networks: Viscoelastic Properties are Determined by the Microscopic Interaction Potential of Cross-links. Biophysical Journal 96: 4725–4732. doi:10.1016/j.bpj.2009.03.038.

146. Aragon SR, Pecora R (1985) Dynamics of Wormlike Chains. Macromolecules 18: 1868–1875.

147. Kroy K, Frey E (1997) Dynamic scattering from solutions of semiflexible polymers. Phys Rev E 55: 3092–3101.

148. Brangwynne CP, Koenderink GH, Barry E, Dogic Z, MacKintosh FC, et al. (2007) Bending dynamics of fluctuating biopolymers probed by automated high-resolution filament tracking. Biophysj 93: 346–359. doi:10.1529/biophysj.106.096966.

149. Taute KM, Pampaloni F, Frey E, Florin E-L (2008) Microtubule dynamics depart from the wormlike chain model. Phys Rev Lett 100: 028102.

150. Tharmann R, Claessens MMAE, Bausch AR (2007) Viscoelasticity of Isotropically Cross-Linked Actin Networks. Phys Rev Lett 98: 088103. doi:10.1103/PhysRevLett.98.088103.

151. Morse D (1998) Viscoelasticity of concentrated isotropic solutions of semiflexible polymers. 2. Linear response. Macromolecules 31: 7044–7067.

152. Morse D (1998) Viscoelasticity of tightly entangled solutions of semiflexible polymers. Phys Rev E 58: R1237–R1240.

153. Hinner B, Tempel M, Sackmann E, Kroy K, Frey E (1998) Entanglement, elasticity, and viscous relaxation of actin solutions. Phys Rev Lett 81: 2614–2617.

154. Bathe M, Heussinger C, Claessens MMAE, Bausch AR, Frey E (2008) Cytoskeletal bundle mechanics. Biophysical Journal 94: 2955–2964. doi:10.1529/biophysj.107.119743.

155. Gardel ML, Shin JH, MacKintosh FC, Mahadevan L, Matsudaira P, et al. (2004) Elastic behavior of cross-linked and bundled actin networks. Science 304: 1301–1305. doi:10.1126/science.1095087.

156. LIU J, Gardel ML, Kroy K, Frey E, Hoffman BD, et al. (2006) Microrheology probes length scale dependent rheology. Phys Rev Lett 96: 118104.

157. Mason T, Gisler T, Kroy K, Frey E, Weitz D (2000) Rheology of F-actin solutions determined from thermally-driven tracer motion (vol 44, pg 917, 2000). Journal of Rheology 44: 1433–1433.

158. Mizuno D, Tardin C, Schmidt CF, MacKintosh FC (2007) Nonequilibrium Mechanics of Active Cytoskeletal Networks. Science 315: 370–373. doi:10.1126/science.1134404.

159. Rosenbluth MJ, Crow A, Shaevitz JW, Fletcher DA (2008) Slow Stress Propagation in Adherent Cells. Biophysical Journal 95: 6052–6059. doi:10.1529/biophysj.108.139139.

160. Luan Y, Lieleg O, Wagner B, Bausch AR (2008) Micro- and Macrorheological Properties of Isotropically Cross-Linked Actin Networks☆. Biophysical Journal 94: 688–693. doi:10.1529/biophysj.107.112417.

161. Claessens MMAE, Tharmann R, Kroy K, Bausch AR (2006) Microstructure and viscoelasticity of confined semiflexible polymer networks. Nat Phys 2: 186–189. doi:10.1038/nphys241.

162. Ando T, Skolnick J (2010) Crowding and hydrodynamic interactions likely dominate in vivo macromolecular motion. Proceedings of the National Academy of Sciences 107: 18457–18462. doi:10.1073/pnas.1011354107.

163. Diamant H (2009) Hydrodynamic Interaction in Confined Geometries. J Phys Soc Jpn 78: 041002. doi:10.1143/JPSJ.78.041002.

164. Pryamitsyn V, Ganesan V (2008) Screening of hydrodynamic interactions in Brownian rod suspensions. J Chem Phys 128: 134901. doi:10.1063/1.2842075.

165. Happel J, Brenner H (1983) Low Reynolds number hydrodynamics. Springer. p.

166. Johnson RW (1998) The handbook of fluid dynamics. CRC. p.

167. Fu H, Shenoy V, Powers T (2008) Role of slip between a probe particle and a gel in microrheology. Phys Rev E 78. doi:10.1103/PhysRevE.78.061503.

168. Schmidt FG, Hinner B, Sackmann E, Tang JX (2000) Viscoelastic properties of semiflexible filamentous

bacteriophage fd. Phys Rev E Stat Phys Plasmas Fluids Relat Interdiscip Topics 62: 5509–5517.

169. Oppong F, Coussot P, de Bruyn J (2008) Gelation on the microscopic scale. Phys Rev E 78. doi:10.1103/PhysRevE.78.021405.

170. Rich JP, McKinley GH, Doyle PS (2011) Size dependence of microprobe dynamics during gelation of a discotic colloidal clay. Journal of Rheology 55: 273. doi:10.1122/1.3532979.

171. De Korte C, Pasterkamp G, Der Steen Van A (2000) Characterization of plaque components with intravascular ultrasound elastography in human femoral and coronary arteries in vitro. Circulation.

172. Schaar JA (2004) Incidence of High-Strain Patterns in Human Coronary Arteries: Assessment With Three-Dimensional Intravascular Palpography and Correlation With Clinical Presentation. Circulation 109: 2716–2719. doi:10.1161/01.CIR.0000131887.65955.3B.

173. Yabushita H (2002) Characterization of Human Atherosclerosis by Optical Coherence Tomography. Circulation 106: 1640–1645. doi:10.1161/01.CIR.0000029927.92825.F6.

174. Karnabatidis D, Katsanos K, Paraskevopoulos I, Diamantopoulos A, Spiliopoulos S, et al. (2011) Frequency-domain intravascular optical coherence tomography of the femoropopliteal artery. Cardiovasc Intervent Radiol 34: 1172–1181. doi:10.1007/s00270-010-0092-8.

175. Goderie TPM, van Soest G, Garcia-Garcia HM, Gonzalo N, Koljenović S, et al. (2010) Combined optical coherence tomography and intravascular ultrasound radio frequency data analysis for plaque characterization. Classification accuracy of human coronary plaques in vitro. Int J Cardiovasc Imaging 26: 843–850. doi:10.1007/s10554-010-9631-2.

176. Templin C, Meyer M, Müller MF, Djonov V, Hlushchuk R, et al. (2010) Coronary optical frequency domain imaging (OFDI) for in vivo evaluation of stent healing: comparison with light and electron microscopy. Eur Heart J 31: 1792–1801. doi:10.1093/eurheartj/ehq168.

177. Moussavi-Baygi R, Jamali Y, Karimi R, Mofrad MRK (2011) Biophysical coarse-grained modeling provides insights into transport through the nuclear pore complex. Biophysical Journal 100: 1410–1419. doi:10.1016/j.bpj.2011.01.061.

178. Moussavi-Baygi R, Jamali Y, Karimi R, Mofrad MRK (2011) Brownian Dynamics Simulation of Nucleocytoplasmic Transport: A Coarse-Grained Model for the Functional State of the Nuclear Pore Complex. PLoS Comput Biol 7: –. doi:10.1371/journal.pcbi.1002049.

179. Keminer O, Peters R (1999) Permeability of single nuclear pores. Biophysical Journal 77: 217–228. doi:10.1016/S0006-3495(99)76883-9.

180. Schaller V, Weber C, Semmrich C, Frey E, Bausch AR (2010) Polar patterns of driven filaments. Nature 467: 73–77. doi:10.1038/nature09312.

181. Köhler S, Schaller V, Bausch AR (2011) Collective Dynamics of Active Cytoskeletal Networks. PLoS ONE 6: e23798. doi:10.1371/journal.pone.0023798.g005.

182. Schaller V, Weber CA, Hammerich B, Frey E, Bausch AR (2011) Frozen steady states in active systems. Proceedings of the National Academy of Sciences. doi:10.1073/pnas.1107540108.